Doctoral Dissertation
博士論文

Research on Hydrodynamic Responses of FOWT Attaching a Torus Structure with Annular Flow
環状流を伴うトーラス構造を有する FOWT の浮体運動特性に関する研究

By
LIU Xiaolei
19QA391

Academic Supervisor: **Prof. MURAI Motohiko**
指導教員：村井　基彦　教授

2022.09

Graduate School of Engineering Science
Yokohama National University

Table of Contents

Acknowledgments

Studying at Yokohama National University has been an unforgettable memory for me, especially most of the time is spent during the COVID-19 pandemic. I am very excited to do this research at the Laboratory of Ocean Space Utilization although full of happiness and sorrow in the process.

First and foremost, I would like to acknowledge my gratitude to my academic supervisor Prof. MURAI Motohiko for his unequivocal patience and continuous support throughout my doctoral four years studies. In four years studies, he takes me to a new world, and his backing and thorough encouragement has integral to the progress in every ways. I have been very grateful to be under his mentorship and learnt the virtues of hard work, meticulous understanding and gaining confidence to face the difficulties and challenges from his guidance. I would like that this is greatest gain of all for me in these four years. Your time and patience helped me immensely for a smooth and conducive environment in our laboratory.

Meanwhile, I would like to thank reviewers of submitted paper for their valuable comments.

In addition, special acknowledgement is due for my parents whose support and sacrifice has enabled me to be where I am today, and I would never finish my PhD paper without them. I will be forever indebted to them.

Last but not the least; I would like to thank all of my friends, being friends with them is a treasure in my life and I will always cherish, and I will also cherish memories forever in Yokohama since the last four years, especially the beauty of running from school to Chinatown.

LIU Xiaolei

August 2022

ABSTRACT

Under the background of global warming, carbon dioxide peaking and carbon neutrality have become one of the goals that people are striving to achieve. Ocean wind energy has always been one of the renewable energy sources that people value and use from ancient sailing ships to modern ocean wind power generation. However, because of the high center of gravity of floating offshore wind turbines (FOWTs), the hydrodynamic response in the roll and pitch DOFs are relatively large under severe sea conditions. Therefore, if the vast space of the far-reaching sea wind energy is used on a large scale, the problem, of restraining the shaking movement of FOWT, that has always plagued us should be researched and resolved seriously.

Until now, all of FOWTs are moored at sea. In this paper, a novel FOWT without a mooring system is designed, its vacillating motion in severe sea conditions is controlled by a spinning top device that is designed as a neutrally buoyant double-layer torus structure with an annular flow water in the internal small radius torus structure, and is welded to the periphery of the central cylinder of FOWT underwater buoyancy providing part. The torus structure is very common in daily life, such as swimming rings, doughnut desserts, bicycle tires, etc. The torus structure is also often used in scientific research, such as the acceleration track of a particle accelerator in particle physics. The neutral buoyancy can keep the constant draft of FOWT for comparative studies, meanwhile, make that steel rod connecting pieces between the periphery of the central cylinder of FOWT and the external large radius torus structure under vertical force as little as possible, delaying its fatigue. Moreover, the neutral buoyancy will also facilitate installation and removal.

It is envisaged but verified with an experiment in this paper that the principle of the rotating annular flow water in the internal small radius torus structure is the same as the rotation of a rigid body - the spinning top. The fact that the moon revolves around the earth without resistance every lunar month plays a vital role in the stability of the earth's rotation axis. In addition to being used as a stabilizer, the spinning top is also widely used in many fields of engineering. For example, it is used to develop gyrocompass for navigation 100 years ago; the 3-axis gyroscope as the micro-electro-mechanical system is put into Iphone4 published in 2010; furthermore, NASA envisages using it to create gravity in space vehicles, but the rotation radius of the space vehicles is required to exceed 100m…… The gyroscopic effect from the precession of annular flow and the rotational axis retention effect from rotational inertia of annular flow can be obtained for actively restraining the shaking movement of

FOWT. If these effects are linearized into the small amplitude problem, they can be treated as a damping force. This paper will study the possibility of contributing to the agitation of FOWT and improving its hydrodynamic response by effectively using these effects.

The presence or absence of the torus structure, the different positions placed in the vertical direction, the radius of the torus structure, the radius of the internal annular flow and the angular velocity of the internal annular flow, the central cylinder radius and the central cylinder height, and the central cylinder wall thickness will be the design variables. Then a large number of comparative calculations based on the fluid-solid coupling theory of potential flow are carried out to determine the appropriate design parameters. Eventually, based on the obtained suitable design parameters, the proposed conceptual design approach is demonstrated to be feasible in view of engineering possibility.

Keywords: floating offshore wind turbine, torus structure, annular flow, gyroscopic effect, rotational axis retention effect, damping force, design variables

Illustration Index

Table Index

Chapter 1:Introduction

1.1 Research Background

Now that the demand for electricity is rapidly increasing in human society, it is difficult to imagine how much inconvenience will be caused by living in an era without electricity. With the development and progress of science and technology, renewable energy has received more and more attention and applications. Among the world's total power generation, the utilization of natural energy power generation has been significantly developed in recent years. According to data released by the British company BP [1] [2], the proportion of natural energy power generation in total power generation has reached 27.8%, and the proportion of wind power generation in total power generation has also reached 5.9% in 2020.

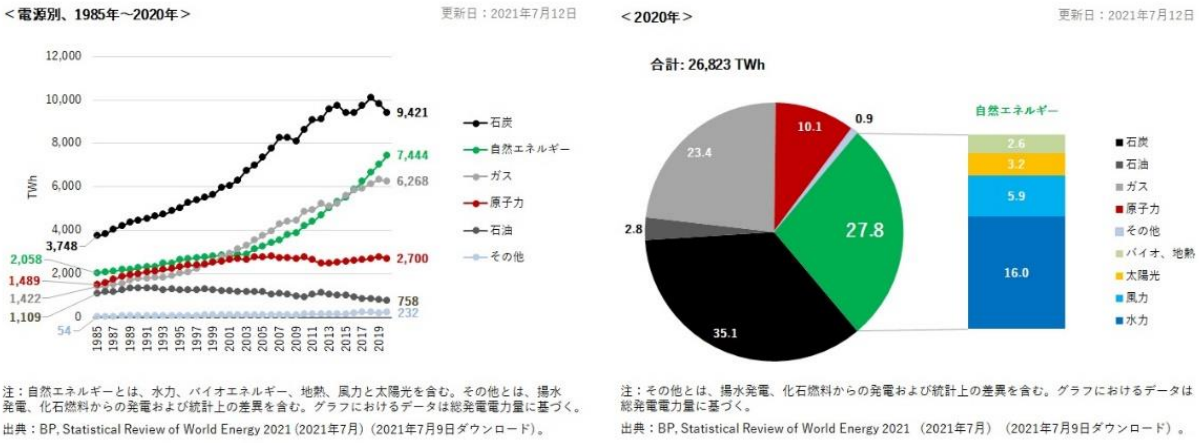

Fig. 1.1 Status of world's electricity power generation

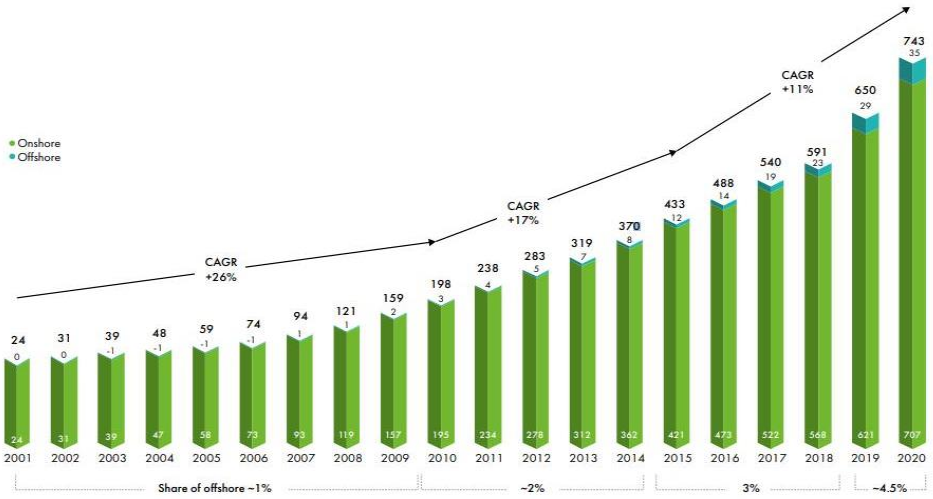

Fig. 1.2 Status of global installed capacity of wind power generation

According to the data of the "Global Offshore Wind Power Report 2021" released by GWEC (Global Wind Energy Council) [3] and the annual report of REN21 [4], the global installed capacity of wind power generation, including onshore and offshore wind power generation, has reached 743 GW by 2020, and offshore wind power generation is developed and constructed from 2.9 GW by 2010 to 35 GW by 2020. From the above data, we can see that with the vigorous construction of offshore wind power generation in recent years, offshore wind power generation accounts for an increasing proportion of all wind power generation.

According to the "Global Offshore Wind Power Report 2020" issued by GWEC [5], as of the end of 2019, there is 65.7 MW floating offshore wind power installed globally, distributed in the UK (32 MW), Japan (19 MW), Portugal (10.4 MW), Norway (2.3 MW), France (2 MW). GWEC predicts that 6.2 GW of floating offshore wind power projects will be built globally in the next 10 years (by 2030), concentrated in South Korea, Japan, France, Norway, and the United Kingdom. Floating offshore wind power projects will be commercialized in 2030. From the above data, we can see that compared with fixed offshore wind power, floating offshore wind power accounts for a very small proportion.

Because offshore wind farms have significant advantages such as high wind speed, small wind shear, small wind turbulence and few fluctuations in wind speed and wind direction, offshore wind power is playing an increasingly important role in the utilization of wind power generation. Through more than 20 years' development, not only the proportion of offshore wind power increased substantially, but also the development trend of offshore wind power is large-scale, deep-sea floating type, low cost, high reliability and remote controllability [6]. Currently, industry consensus is that when the water depth exceeds 50~60 m, fixed foundations will no longer be economical due to high geological survey costs, high underwater structure costs and high construction costs. However, the current status is that the technical threshold of floating offshore wind power generation is much higher than that of fixed offshore wind power generation, the cost is approximately three times of fixed offshore wind power generation and ten times of natural gas, resulting in a very low proportion of floating offshore wind power generation.

Look back on the development history of floating offshore wind power, the professor **William Edward Heronemus** of University of Massachusetts at Amherst (UMass) of USA proposed the concept for the first time in 1972, but 20 years later, it was the pool test phase of scale model from 1990 to 1999. Since then, the progress had accelerated, it was the low-power prototype test stage from 2000 to 2008, and it was the demonstration stage of megawatt unit prototype from 2009 to 2018. At present, some commercial projects have been carried

out. This article collected statistics on the projects of the demonstration stage and commercial projects as much as possible [7] [8] [9].

Tab. 1.1 Projects of the demonstration stage in EU

Name	Hywind Demo	WindFloat 1	FLOATGEN
Country	Norway	USA	France
Company	Statoil (Equinor)	Principal Power	IDEOL
Location	Stavanger, Norway	Aguçadoura, Portugal	Le Croisic
Type of Floating	SPAR	Semi-Sub	Barge concrete used
Rated Power [MW]	2.3	2	2
Windmill Type	Siemens	Vestas V-80	Vestas V80
Rotor Diameter [m]	85	80	80
Distance from Shore [km]	10	5	22
Water depth [m]	220	45	33
Operation Time	2009	2011-2016	2018

Tab. 1.2 Projects of the demonstration stage in Asia

Name	福島未来	福島新風	福島浜風	ひびき	椛島 project	三峡引领号
Location	福島県沖			北九州市	長崎県五島市	中國阳江市
Type of Floating	Semi-Sub	Semi-Sub V-type	SPAR	Barge 2 blade	SPAR concrete at lower	Semi-Sub
Rated Power [MW]	2	7	5	3	2	5.5
Windmill Type	Downwind	Hydraulic drive	Downwind	Upwind	Downwind	
Rotor Diameter [m]	80	167	126	100	80	158
Draft [m]	16	17	33	7.5	76	13.5
Mooring Number	6	8	6	9	3	
Chain Diameter [mm]	132	132	132	132	132	
Distance from Shore [km]	20			15	2	28
Water depth [m]	100~150			50~100	100	27~32
Operation Time	2013	2015	2016	2018	2013	2021

Tab. 1.3 Current commercial projects

Name	Kinkardine	Hywind Scotland	WindFloat Atlantic	Hywind Tampen
Installed Capacity [MW]	49.5	30	25	88
Location	Scotland Aberdeen	Scotland Peterhead	Portugal Viana do Castelo	Norwegian Snorre and Gullfaks
Type of Floating	Triangle Semi-Sub	SPAR	Semi-Sub	SPAR
Rated Power and Number	9.5MW × 5	6MW × 5	8.4 MW × 3	8MW × 11

	and 2MW × 1			
Windmill Type	MHI-Vestas	Siemens-Gamesa	MHI-Vestas	Siemens Gamesa
Rotor Diameter [m]	164 and 80	154	164	167
Distance from Shore [km]	15	25	20	140
Water depth [m]	60-80	95-120	100	260-300
Operation Time	2020	2017	2019	2022

We can see that there are mainly three types of floating structures, SPAR, Semi-Sub and Barge [10].

Fig. 1.3 Three types of FOWT (floating offshore wind turbine)

The features of SPAR:

- The water-plane area is small and is suitable for setting in more severe ocean wave environments.
- The draft is large, and the water depth is basically required to be above 80 m.
- The heave motion is small, but the roll and pitch DOFs motions are relatively large.
- The unit needs to be transported and installed separately.

The features of Semi-Sub:

- A reasonable buoyancy and gravity distribution can be formed by the ballast degree of each pontoon to maintain balance.
- The draft is shallow, and the unit is less difficult to transport and install.
- The cost is high.

The features of Barge:

- The middle is hollow that resembles a moon pool, it can have a damping effect.
- The cost is low.
- The design of the mooring system is difficult.

- The roll and pitch DOFs motions are relatively large.

The three types of FOWT have their own advantages and disadvantages from an engineering point of view. In addition, there are some other design ideas. For example, the "TwinWay" project is run by Hexicon, Sweden [11]. It is a type of TLP (Tension Leg Platform), as the two turbines that being set up on one platform are downwind of the taut mooring point, wind forces naturally turn the platform, just like a boat moored by anchor. It has high requirements for mooring ropes and sensitive to tides, but it can have good heave and roll motion hydrodynamic response.

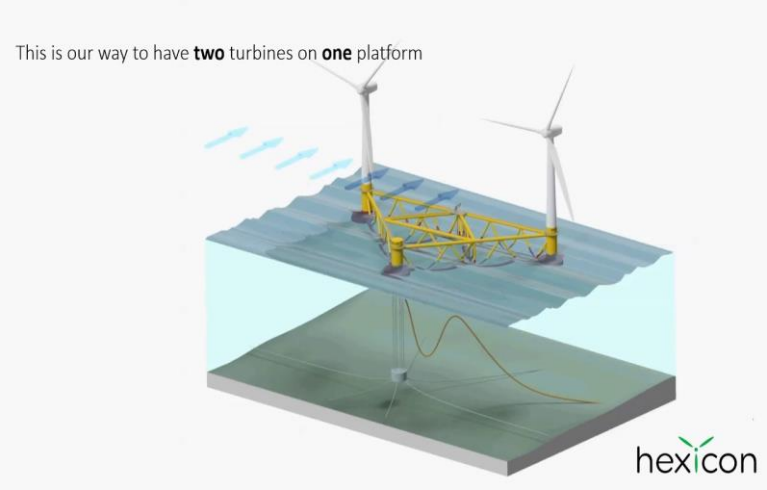

Fig. 1.4 The other type of FOWT

In actual production, which type FOWT is selected needs to be based on the characteristics of the installation sea area, comprehensive consideration of safety and economy all in all. In 2020, offshore wind power industry providing about 297,000 full-time jobs, approximate 350,000 wind turbines are in operation worldwide. In the future, Rystad Energy [12] predicts that offshore wind power industry will drive about 868,000 jobs by 2030 based on the installed capacity of offshore wind power that will reach 250 GW by 2030. The European Commission [13] predicts that Europe will need 230-450 GW of offshore wind power by 2050, which will account for 30% of European electricity demand, of which 100-150 GW will come from floating offshore wind power. The Japan Wind Power Association (JWPA) [14] predicts that Japan will build 42.8 GW of offshore wind power generation by 2050, of which 23.8 GW will come from floating offshore wind power. As of 2020, this value is 0.7 GW of offshore wind power, of which 0.1 GW of electricity comes from floating offshore wind power. It will take a long way! In addition, Japan's current onshore wind power generation has reached 10.2 GW, and it is estimated that the scale of onshore wind power generation will reach 38 GW by 2050,

the increase will be much smaller than offshore wind power generation.

1.2 Research Motivation

Humans have always maintained a strong interest in overcoming the torque generated by gravity that is always perpendicular to the earth surface. For example, the popularity of “Broom Stick Challenge” activity in recent years and the development of bicycle that is not easy to fall. In recent years, an artificial intelligence-based bicycle that can drive automatically has been realized, which won't fall and stand upright at zero speed even without the bicycle foot stand. Moreover, since ancient times, the issue of “how to reduce the vibration and shaking of marine structures in waves” has been always researched in the field of marine engineering. Even now that science and technology have made great progress, it is still a problem that needs special attention in marine engineering.

Fig. 1.5 Violent pitch motion in the second sea trial of “INS Vikrantthe” [15]

From the development of the shipbuilding industry with a long history, engineers have got many effective methods to solve this problem, and various kinds of anti-rolling devices are designed and manufactured to reduce the rolling motion of the ship, mainly consider from the following three aspects:

1. To increase the damping coefficient

This approach is called "damping stabilization" such as bilge keel by generating and releasing vortex when ship become roll, since the physical meaning of damping refers to the consumption of energy, this anti-rolling method is effective in any situation, especially in the resonance zone.

2. To change the natural frequency of the ship

This method is called "harmonic stability", for the natural frequency of the ship avoids the

wave frequency. However, since there are various wave frequencies on the actual ocean, this method is not always appropriate, and it is also unrealistic to make a device to change the natural frequency of the ship. This can only be considered generally when designing the ship that to keep the natural frequency of the ship away from the frequency of the most frequent waves occurring in the ship served sea area.

3. To reduce the disturbing force or moment

This method is called "balance and stability" such as rudder, anti-rolling fin, anti-rolling tank, and in principle it can be applied to all rocking motions. In this case, a stable torque that is opposite to the disturbance torque is applied, so that the disturbance torque is reduced.

The bilge keel can achieve the most obvious anti-rolling effect at zero speed, but the anti-rolling effect is not too big. The rudder and the anti-rolling fins can achieve a satisfactory anti-rolling effect only in a relatively high sailing speed, and the reason is the anti-rolling fin need to rely on the lift force generated on the wing-shaped surface of the fin to generate a rolling restoring moment, and the lift force is proportional to the square of the speed within a certain range. When sailing at low speeds, the lift force generated by the fin is very small, it has no obvious anti-rolling effect at all. The anti-rolling tank also has its relative shortcomings. Only when the anti-rolling tank reaches a certain volume (generally about 30-40%), it can produce sufficient rolling restoring moment, so the anti-rolling tank occupies a lot of space on the ship. In addition, it should be noted specially that the effective anti-rolling frequency range is very narrow because it works according to the "double resonance" principle, the self-rolling frequency of the anti-rolling tank must be higher than the self-rolling frequency of the ship, otherwise it will even increase the rolling effect, which will bring certain difficulties to the design of the anti-rolling tank [16].

In recent years, with the development of marine engineering, engineers have created a method named DPS (Dynamic Positioning System), that sensors put the measured environmental forces to the computer, then the computer-controlled system to automatically maintain position by using its own propellers and thrusters. But DPS is a complex system and is concerned primarily with control of the marine structure in the horizontal plane: surge, sway and yaw DOFs [17].

Another anti-rolling methods such as mooring lines are the most practical method and are widely used in actual production. At present, there are mainly two kinds of mooring method. The traditional catenary mooring line, which provides horizontal resilience by its own weight, and the taut mooring line, which provides horizontal resilience by its own elastic tension. As marine engineering advances into deep water, the required length and mass for traditional

catenary mooring will increase the costs. On the other hand, taut mooring is expected to reduce costs because it has the advantages of shorter length than catenary mooring, a smaller area of the occupied seabed, and a smaller load on the structure. However, the disadvantages of mooring lines are also obvious, the mooring lines require a firm connection to the seabed, and when the water depth is super deep, too long mooring line is very inconvenient and difficult to install [18].

Because of the limitation of these traditional anti-rolling devices, this paper proposed a novel anti-rolling concept to study the possibility of improving hydrodynamic response that using the spinning top (コマ) that generates the rotational axis retention effect from rotational inertia and the gyroscopic effect come from the precession motion [19]. Just as the fact that the moon revolves around the earth without resistance every lunar month plays a vital role in the stability of the earth's rotation axis. The tank's gun barrel uses a gyro stabilizer to allow it to fire accurately even when driving on bumpy roads. In addition to being used as a stabilizer, the spinning top is also widely used in many fields of engineering. For example, it is used to develop gyrocompass for navigation 100 years ago; the 3-axis gyro- scope as the micro-electro-mechanical system is put into Iphone4 published in 2010; furthermore, NASA envisages using it to create gravity in space vehicles, but the rotation radius of the space vehicles is required to exceed 100 m …… Generally speaking, the rotational axis retention effect and the gyroscopic effect are generated through the rotation of a rigid body, and obviously FOWT can't rotated. The assumption in this article is to obtain the above rotational momentum through the fluid flows at a constant angular velocity to form an annular flow in the torus structure which will be welded to the periphery of the underwater buoyancy providing part. The rotating object, an annular flow, is attached in the FOWT, and itself does not touch the outside seawater. It is envisaged that the principle of the rotating annular flow in the torus structure is the same as the rotation of rigid body, but at this time the torus itself does not need to make a rotational movement, and the suppression effect to restrain vacillating movement of FOWT can be generated by changing the angular velocity of annular flow in the ring tube of the torus structure. Generally speaking, the rotation of annular flow in the torus structure will affect the torus structure through friction, so that the torus structure will also become rotate finally, regarding this point, reducing the friction between the rotating annular flow and the torus structure as little as possible, or using other ways to form rotation in the torus structure with as little friction as possible, even mooring lines are considered to be used to offset it. First, study without considering this frictional force is carried out in this paper.

In daily life, the torus structure is very common, such as swimming rings, doughnut dessert, bicycle tires, etc. The torus structure is also often used in scientific research, such as the acceleration track of a particle accelerator in particle physics. The torus structure in this article has double-layer structures with a large external torus and a small internal torus inside the large external torus, and the two parts are joined together by welding steel rod so as to the large external torus and the small internal torus have the same center of the ring tube and the same center of the torus. That is, they are concentric. All space in the ring tube of the small internal torus is densely filled with fluid and all space between the ring tube of the large external torus and the ring tube of the small internal torus is filled with air. The radius of the ring tube of the large external torus is determined so that it has neutral buoyancy in order to keep the constant draft of FOWT, meanwhile, make the steel rod connecting piece between the central cylinder and the torus structure under vertical force as little as possible, delaying the bending fatigue of steel rods due to the influence of gravity from objects at both sides, but the fatigue caused by stretching movements in the horizontal direction cannot be delayed.

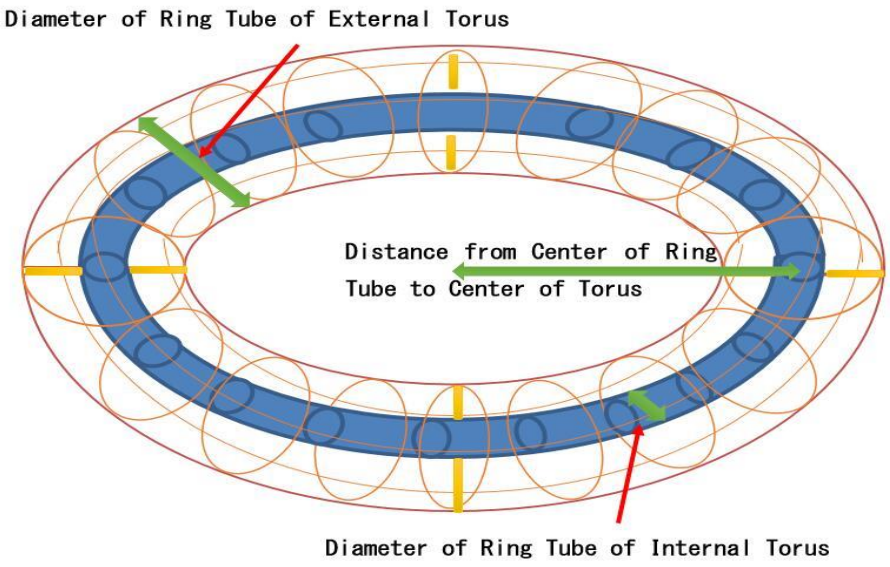

Fig. 1.6 The designed double-layer torus structure

Wind turbines are designed to increase power generation and optimize kilowatt-hours of electricity through wind loads, the design concept of wind turbines is to hope for greater wind speed. While marine floating structures are designed to meet the requirements of hydrodynamic response, the design concept of marine floating structures is to minimize wave loads, which are generally caused by wind loads. Combining the design concept of the wind turbines and the marine floating structures, FOWT has two contradictory parts, but compared

with fixed offshore wind power generation, the overall installation and overall towing of FOWT are also very convenient, the costs of construction and installation are reduced by optimizing the floating foundation under the premise of ensuring safety, especially in deep water. Currently, marine aquaculture and hydrogen production have been assumed to combine with FOWT, the advantages of FOWT will become more and more obvious.

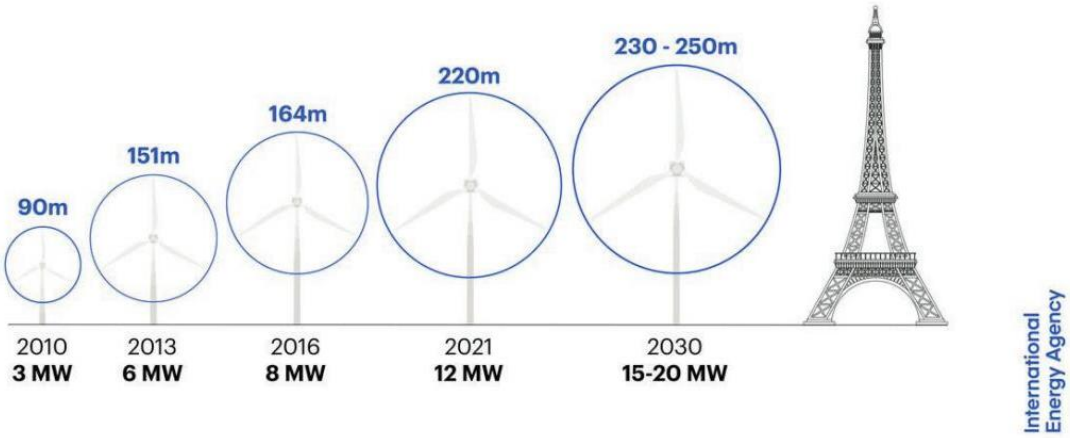

Fig. 1.7 Development trend of FOWT

In recent years, the rated power of FOWT is getting bigger and bigger, even 20 MW FOWT with blades longer than 100 m is under discussion. The pitch and roll DOFs motions of such a large FOWT will also increase proportionally. This article focuses on the development trend of FOWT and designs a novel large-scale deep-sea FOWT using the principle of the spinning top in order to improve hydrodynamic response of FOWT with a high center of gravity. The blades are designed based on BEM theory (Blade Element Momentum) [20], the floating foundation parts are designed as Cylinder-type and SPAR-type based on potential flow theory. Since the vertically elongated structure such as SPAR-type has a relatively small stability against inclination, the possibility of contributing to the agitation of SPAR-type FOWT by effectively using the principle of gyroscopic. With the overall cost-effectiveness of the system as the goal and safety as the constraint, the performance indicators of wind turbines and floating foundations are allocated, reliability matching is carried out, and detailed design is carried out after iterative optimization. It can ensure the safety and normal operation under severe weather conditions in the future

1.3 The Organization of This Thesis

The first chapter mainly introduces the development history and current situation of FOWT and the new FOWT model proposed in this paper. Section 1.1 gives the development status

of total power generation and wind power generation through statistical data, especially for FOWT, the development history and current situation are explained, and the prospective and necessity of FOWT research are analyzed. Section 1.2 gives the design method of the buoyancy support part in the water for FOWT by summarizing the current anti-rolling technical route in ship design, and describes in detail the new FOWT model proposed in this paper, which is in line with the anti-rolling technical route of increasing the damping coefficient.

The second chapter mainly introduces the research process of fluid-structure interaction in ship motion forecasting problem, especially with the development of computer technology in recent years, the hydrodynamic calculation problem has made great progress.

The third chapter mainly introduces the knowledge that will be used in this paper in the seakeeping theory of marine structures, mainly including the prediction method of the three-dimensional speedless floating body in steady state, and gives the detailed calculation and derivation process of the hydrodynamic coefficient, and frequency domain motion equation and time domain motion equation of three-dimensional speedless floating body on 6 DOFs, and calculation method of motion response of three-dimensional speedless floating body under the action of irregular waves. In addition, the torus geometry is also introduced, and the process of obtaining the damping force using the gyroscopic effect from the precession of spinning top and the rotational axis retention effect from rotational inertia of spinning top is given by linearization under the assumption of small amplitude.

The fourth chapter firstly introduces the simple pendulum experiment to verify that the rotating annular flow in the torus structure can indeed act as a damping force like a rigid spinning top, and then introduces the calculation results of the hydrodynamic response of the new floating windmill model conceived in this paper. The dimensionless RAO of pitch DOF under the action of regular waves in the frequency domain and the expected value of the pitch DOF under the action of irregular waves are verified, and the effect of the existence of the torus structure on improving the hydrodynamic response is verified, especially, the reasonable value range of the design parameters of the different positions placed in the vertical direction, the radius of the torus structure, the radius of the internal annular flow and the angular velocity of the annular flow, the central cylinder radius and the central cylinder height, and the central cylinder wall thickness is determined, and by comparing the Cylinder-type FOWT and SPAR-type FOWT, provide guidance for finding a FOWT with excellent hydrodynamic response.

The fifth chapter mainly introduces the conclusions obtained in the full text by summarizing.

Chapter 2:Literature Review

2.1 General Introduction

Ancient Greek **Archimedes** studied the theory of buoyancy and created hydrostatics in his book 《On Floating Bodies》 in the third century BC. After that, in the 17th century, French **Blaise Pascal** proposed **Pascal**'s principle in his book 《A Collection of Essays on Liquid Balance and Air Weight》 to enrich hydrostatics content.. However, once the fluid moves, its complexity becomes extremely huge. For the study of hydrodynamics, after **Newton** invented **Newton**'s law of motion in his book 《Mathematical Principles of Natural Philosophy》 in 1687, **Daniel Bernoulli** of Switzerland proposed Bernoulli's principle to give an incompressible, inviscid, energy conservation formula for steady flow along the streamline in his book 《Hydrodynamica》 in 1738. Afterwards, in 1757, **Leonhard Paul Euler** gave the continuity equation of the conservation of mass and the momentum equation of the conservation of momentum governing the motion of inviscid fluids in his paper 《Principes généraux du mouvement des fluides》. France **Pierre-Simon, marquis de Laplace** gave the third equation representing the conservation of energy in **Euler**'s equation in 1816, and he also quantitatively described the properties of water waves for the first time and gave the dispersion relationship of water waves.

At this time, the use of rigorous mathematical tools to study the inviscid ideal fluid theory is quite complete, but when studying the resistance of objects in the fluid, the theoretical calculation of the inviscid ideal fluid is very different from the actual experimental results. In this context, based on a large number of experimental measurements, such as **Gotthilf Heinrich Ludwig Hagen** in Germany, **Jean Léonard Marie Poiseuille** in France, and **Osborne Reynolds** in the United Kingdom have used experiments to study the resistance and pressure loss of water and other viscous fluids flowing in pipes and trenches, obtained empirical formulas and semi-empirical theoretical formulas that help solve some practical engineering problems. The hydraulics for studying the flow of incompressible viscous fluids is established.

Later, the French **Claude-Louis Navier** added the viscosity term to the **Euler** differential equation of motion in 1827, and the Irish **George Gabriel Stokes** made a strict derivation in 1846. The **Navier-Stokes** equations describing the complete fluid motion are given. Since then, fluid mechanics has entered the computational fluid dynamics stage of solving equations. In 2000, the **Clay** Mathematics Institute (CMI) announced the seven major problems of the world millennium, "**Navier-Stokes** Existence and Smoothness" is among them, and it has not yet been resolved. In the research of solving equations, **Boussinesq** puts forward the

hypothesis of eddy viscosity, which analogizes the shearing stress caused by turbulent pulsation to **Newton**'s internal friction law, that is, multiplying the viscosity by the velocity gradient to express the shearing stress caused by turbulent pulsation. **Reynolds** decomposes the instantaneous velocity into the time-averaged velocity and the pulsating velocity, and obtains the **Reynolds** average N-S equation – RANS. Then the representative results is **Ludwig Prandtl**, Germany, who proposed the concept of boundary layer in the paper 《On the Motion of Fluids in Very Little Friction》 in 1904 and after then established the mixing length theory with the efforts of many people, which gave clear answers to the incomprehensible and difficult-to-answer fluid phenomena in the past, which changed the long-term disconnection of theoretical fluid mechanics and hydraulics, and closely linked theory and practice together, forming modern fluid mechanics with equal emphasis on theory and experiment.

In addition, potential flow theory based on the field theory method has also been paid attention to with the deepening understanding of electromagnetic phenomena. These are studies based on the macroscopic continuum assumptions of **Newtonian** fluids in large-scale slowly changing "thermal dynamic equilibrium" or "quasi-thermal dynamic equilibrium states". Partial differential equations are used to describe fluid motion equations, which reflect **Newton**'s second law, it is especially emphasized that the mass in **Newton**'s second law is inertial mass. In addition, there are statistical-based research methods in physics. The velocity distribution function of molecules is used to describe the velocity distribution of fluid particles in space. The total rate of change of the velocity distribution function is equal to the rate of collision, thereby deriving the macroscopic properties of the fluid, which is the LBM (Lattice **Boltzmann** Methods) [21] [22] [23].

Since the 1940s, the establishment and solution of the linear boundary value problem of the velocity potential has been used to predict the motion of ships on waves. Around 1950, considering the influence of the existence and movement of the ship on the flow field of the incident wave, **Haskind** [24] [25] applied **Green**'s theorem to construct the disturbance velocity potential caused by the existence and movement of the ship, and divided the disturbance velocity potential into the diffraction velocity potential and radiation velocity potential within the range of linear theory. The former only considers the interference of a fixed floating body on the incident wave flow field, that is, wave diffraction; the latter only considers the disturbance of the static water flow field by a floating body in 6 DOFs. This method is still a typical processing method to deal with linear disturbance velocity potential. This also shows that what is important in the theory of floating body motion response in regular waves is the concrete solution of the radiation wave and diffraction wave problem. Then the analytical

expression of the point source Green's function is deduced. According to the boundary conditions, the integral equation for solving the velocity potential is finally obtained, and this integral equation is further solved by using the narrow ship assumption. At about the same time, Havelock, Ursell [26] used the multipole expansion method to solve the velocity potential boundary value problem for a cylindrical floating body. However, these studies are all researches on floating bodies with simple geometric shapes. The three-dimensional theory of hydrodynamic calculations for actual ships and other floating bodies with complex geometric shapes, Haskind [27], Havelock [28], F. John [29] [30] and others to solve the analytical expression of Green's function of three-dimensional pulsating point sources, but at that time there was a lack of large-capacity, high-speed computers, and three-dimensional theoretical numerical calculations were not realized. It was not until the 1970s that conditions were created for three-dimensional theoretical numerical calculations. Hess and Smith [31] of McDonnell Douglas in the United States began to use computer to solve the three-dimensional non-lift-free flow problem in an unbounded flow field based on the singularity distribution method (boundary element method; Green function method) for the first time. Since then, three-dimensional theories and methods have been developed rapidly, especially the three-dimensional frequency domain theory. The most commonly used numerical method in the three-dimensional frequency domain theory is the Green's function method. At present, there are two mainstream methods: the three-dimensional free surface Green's function method and the Rankine source method. The free-surface Green's function used in three-dimensional free surface Green's function method satisfies all boundary conditions except the surface condition of floating body. Therefore, it is only necessary to distribute the source and dipoles on the wet surface of the hull to calculate the velocity potential, which is especially suitable for solving the problem of hydrodynamic interaction between a speedless (zero forward speed) floating bodies and waves. The Rankine source method needs to distribute sources and sinks on the entire flow field boundary, which requires a large amount of calculation, and appropriate methods must be used to deal with free surface conditions and radiation conditions.

For the three-dimensional time domain theory, the Finkelsteinsdl [32] system derives the time-domain Green's function that satisfies the free surface condition under infinite water depth and finite water depth. Cummins [33] creatively decomposes the disturbance velocity potential into two parts, the instantaneous effect and the memory effect, and the motion is separated from the geometry of the object, and the impulse response function method is established. Although it is not too late to put forward the three-dimensional time domain

theory, it was not until 1979 that **Oorermersen** [34] of the Netherlands Ship Model Basin realized numerical calculations on the computer. The huge amount of calculation of the three-dimensional time domain theory limits its development. However, compared with the three-dimensional frequency domain theory is only suitable for solving steady-state problems, it has advantages for complex problems such as nonlinearity and transient state.

Up to now, a large amount of numerical results have been compared with some available experimental data as well as some contemporary analytical techniques used by many researchers. By evaluating a number of studies up to date, the seakeeping committee of the 24th ITTC (UK, 2005) has shown its confidence over the three-dimensional frequency domain **Green** function method. Based on this method, commercial software such as "WAMIT" from MIT, "SESAM" from DNV, and "HYDROSTAR" from BV has been developed and widely put into operation in ship design. The numerical calculation method used in the research of FOWT design in this paper is also the three-dimensional frequency domain theory, specifically it is the free-surface **Green**'s function. By the way, instead of obtaining the three-dimensional time-domain disturbance potential function directly, the hydrodynamic parameters of the time-domain motion equation can also be obtained through the indirect time-domain method, that is, FTTM (the frequency to the time domain transformation method).

Meanwhile, the significant breakthroughs research of predicting the movement of ships on waves have been made in the other two areas. A significant breakthrough was the work got by **Korvin-Kroukovsky** [35] and **Jacobs** (1957) [36]. By applying the slender concept in aerodynamics, they provided the early version of strip theory based on physical intuition rather than the rigorous mathematics. This is a kind of ship motion calculation method on waves that easily incorporates the effects of R/D waves by taking advantage of the slenderness of the ship. Even though their theory was later found to be mathematically inconsistent, experimental data have shown that it nevertheless provides very good results in many cases. After then, many researchers developed and improved the strip theory in three aspects. The first aspect is the theoretical foundation was rationalized and rigorous, a number of modified versions of the strip theory have been developed, of which, new strip method (NSM) proposed by **田才 福造** and **高木 又男** (1969) [37]; rational strip theory proposed by **Ogilvie** and **Tuck** (1969) [38] [39]; STF method proposed by **Salvesen**, **Tuck** and **Faltinsen** (1970) [40], et el [41]. Specially, the work of **Newman** (1978) [42] that overcame the limitations of this conventional strip theory to the region of high frequency and proposed a unified strip theory which is valid throughout the whole frequency region. The second aspect is due to the emergence of the multi-parameter

conformal transformation method and the close-fit method, the two-dimensional profile has been developed, and there is no need to replace the real ship-shaped profile with an approximate profile. The third aspect is popularizing the strip theory to predict ship motions on the diagonal waves. The strip theory has very fast calculation speed and relatively reliable calculation results for low-speed and medium-speed ships, this led to its rapid development and application after the 1950s, but this theory has its inherent limitations that the floating body must be slender, for the reason that the hydrodynamic parameters of the surge DOF of the ship cannot be given.

Another very significant step was the introduction of spectrum analysis method. Spectral distribution information that can represent ocean waves stochastically, proposed by **St. Dennis** and **Pierson** (1953) [43] that using the results by oceanographers who applied the statistical theory of irregular phenomena to ocean waves in the 1940s. Then, using the principle of linear superposition, the spectrum of ship motion can be obtained from frequency response multiply by the ocean spectrum, and if the maximum value prediction theory for **Longuet-Higgins** statistics, that most commonly used in engineering, is applied to this, various design quantities can be calculated for ships navigating in chaotic ocean waves.

2.2 Objective

In order to guarantee the floating body's enough seakeeping performance, safety and reliability, it's important that motions and wave loads can be predicted within sufficient engineering accuracy. As a basic research, this article will numerically discuss how the gyroscopic effect and the rotational axis retention effect generated from the annular flow affect the vacillating motion of FOWT based on potential flow theory.

- The presence or absence of the torus structure;
- The different positions placed in the vertical direction;
- The radius of the torus structure;
- The radius of the internal annular flow;
- The angular velocity of the annular flow;
- The cylindrical radius of the central floating body;
- The draft of the central floating body;
- The wall thickness of the central floating body;

will be seen as design variables in this paper.

Chapter 3:Formulation of Marine Structures Hydrodynamics

3.1 The Steady-State Periodic Motion Problem of the Three-Dimensional Speedless Floating Body in Regular Wave

3.1.1 The Control Equation

Seawater is treated as an ideal fluid in this paper, then seawater has the following two properties.

1. Uncompressible

When the **Knudsen** number $Kn = \frac{\lambda}{L} < 0.01$, λ is mean free path, L is representative physical length scale, seawater fluid can be thought as a substance that can be continuously divided. This means that seawater fluid is a continuous smoothly changing medium which is assumed that seawater molecules are continuously distributed in space and random thermal motion of micro molecules will not affect macro physical quantities. Although the shape of seawater is not fixed, the volume will not change from the macro physical perspective. According to the experimental results about seawater compressibility problem, when 1 cm^2 of water is subjected to 1 kg of pressure, its volume can only be reduced by 1/22000, and then for every additional kilogram of pressure, it can only be reduced by that. In the deepest part of the ocean, the density of water has only increased by 1100/22000 [44]. In other words, the rate of change in volume is approximate zero, seawater can be treated as an uncompressible fluid.

$$\frac{\partial \rho}{\partial t} + (\nabla \cdot \rho \boldsymbol{v}) = 0 \tag{3.1}$$

$$\nabla \cdot \boldsymbol{v} = 0 \tag{3.2}$$

where, ρ is the fluid density, $\boldsymbol{v}$ is the velocity of fluid. The differential equation is just an approximation, because there are no absolutely incompressible objects, and its **Poisson**'s ratio σ is exactly equal to $\frac{1}{2}$, and its **Young**'s modulus $\frac{(1-\sigma)}{(1+\sigma)(1-2\sigma)}$ tends to $+\infty$. Equation 3.1 represents the conservation of fluid mass, and is also called the continuity equation, is a part of **Euler** equation in hydrodynamics.

2. No viscosity and non-rotational motion

Viscosity refers to the ability of the fluid to resist deformation. The viscosity is greater, the ability to resist external shearing forces will be stronger. The seawater viscosity coefficient is about 10^{-3} Pa·s at 20 ℃. [45] It is a very small value in the fluid, so seawater can be treated without viscosity, it is an ideal fluid (a “dry” water) that no resistance to shearing forces. Its

stress tensor is a diagonal tensor, with only three values on the diagonal representing the pressure. In recent years of condensed matter physics research, it has been found that liquid helium does not have any viscous resistance when flowing below a certain critical temperature, which is called superfluid. The assumption of seawater as an ideal fluid is that the water particle is not under shearing force at the beginning of the movement, then the water particle will continue to move without rotation, because the shearing force is the force of the fluid micro-elements to make a rotational movement. By the **Stokes** equation:

$$\int_L \boldsymbol{F} \cdot d\boldsymbol{r} = \iint_\Sigma (\nabla \times \boldsymbol{F}) \cdot \boldsymbol{n} ds \tag{3.3}$$

$\int_L \boldsymbol{F} \cdot d\boldsymbol{r} = 0$. L is an arbitrary closed curve in the flow fluid field, in other words, $\nabla \times \boldsymbol{F} = 0$. It is irrotational motion, and the vortex will be $\Omega = \nabla \times \boldsymbol{v} = 0$. It is similar to the electrostatic field or static magnetic field equations in free space (unbounded space).

Therefore, only the conservative force exists in the "dry" water.

$$\boldsymbol{F_x} = -\frac{\partial U}{\partial x}, \boldsymbol{F_y} = -\frac{\partial U}{\partial y}, \boldsymbol{F_z} = -\frac{\partial U}{\partial z} \tag{3.4}$$

U is called potential, then

$$\boldsymbol{v} = \nabla \phi \tag{3.5}$$

when connected to the continuity equation,

$$\nabla^2 \phi = 0 \tag{3.6}$$

This equation is also called the **Laplace** equation which is drawn a physics phenomenon that is stable all the time and has nothing to do with time. As an elliptic partial differential equation, in addition to the non-rotational liquid flow, there is also other physical conditions, such as stable heat flow, the current in the doped medium, and the flexure of the elastic membrane conform to this equation. Therefore, there is no initial condition and only boundary conditions for the **Laplace** equation. Generally, there are three kinds of boundary conditions: **Dirichlet** boundary condition ϕ, **Nuamann** boundary condition $\frac{\partial \phi}{\partial n}$ and **Rubin** boundary condition $\phi + \frac{\partial \phi}{\partial n}$. There are also mixed boundary conditions due to practical problems [46].

For the ocean flow field, the actual boundary conditions of the ocean are very complicated and undisciplined. At least, the velocity potential ϕ also satisfy the free surface condition, the seabed condition, the distant condition and floating body surface condition.

3.1.2 The Equation of Boundary Conditions

This article is based on the view of **Euler**'s method (control volume) to analyze, it focuses on the selected spatial point to study the parameters of the fluid particle at different moments of the entire flow field, and the study is the instantaneous flow parameters that occupy all the fluid particles in the flow field. Because position is always relative, when analyzing the motion

of the floating body on the waves, two coordinate systems are used. The first one is the space fixed coordinate system $o_0x_0y_0z_0$ which $o_0x_0y_0$ coincide with the static water surface and oz_0 axis in the vertical direction. The second one is the dynamic coordinate system $oxyz$ that is consolidated with the floating body and moves with the floating body. When the surface of the floating body is expressed in this coordinate system, the surface equation of the floating body does not contain a time term. All the quantities in this Section are expressed in the space fixed coordinate system $o_0x_0y_0z_0$.

1. The free surface condition

Fluid is both a nonlinear medium and a dispersive medium that has very complex free surface conditions. Under the assumption of small amplitude wave, the free surface displacement ζ is much smaller than the wavelength λ, that is $\zeta \ll \lambda$, for the ocean surface wave, generally speaking $\zeta/\lambda < 1/20$, depending on the **Ursell** number $U = \frac{\zeta}{h}\left(\frac{\lambda}{h}\right)^2$, h is the water depth, the free surface condition is linearized. The free surface condition has two types of boundary conditions: kinematics and dynamics. If the fluid on the free surface is on the free surface all the time and the fluid under the free surface cannot escape from the free surface, then the kinematic boundary condition is as follows:

$$\frac{\partial \zeta}{\partial t} = \frac{\partial \Phi}{\partial z} = 0 \ \ (z = 0) \tag{3.7}$$

If the pressure on the free surface and the pressure on the atmosphere are equal all the time, then the dynamic boundary condition is as follows:

$$g\zeta + \frac{\partial \Phi}{\partial t} = 0 \ \ (z = 0) \tag{3.8}$$

After the merger:

$$\frac{\partial^2 \Phi}{\partial t^2} + g\frac{\partial \Phi}{\partial z} = 0 \ \ (z = 0) \tag{3.9}$$

2. The seabed condition

Since the fluid particle cannot pass under this condition.

$$\frac{\partial \phi}{\partial z} = 0 \ \ (z = -h) \tag{3.10}$$

where, the water depth h is constant.

3. The distant condition

According to the law of conservation of energy, energy does not disappear out of thin air, but various energy forms can be transformed. In other words, an energy will never be equal to 0 unless it is converted into other forms of energy. The real-world ocean boundary transforms the kinetic energy and potential energy of the wave by changing the size of the boundary domain. When the kinetic energy of the wave is completely converted into potential energy, the kinetic energy of the wave becomes 0. For a huge ocean, limiting the space of the fluid domain to a fixed size, but the radius of this space R is infinite. The fluid loses its velocity in

the infinite distance.

$$\lim_{R\to\infty} \nabla \phi = 0 \tag{3.11}$$

This unbounded fluid condition is also called **Sommerfeld** condition. It is firstly proposed by German physicist **Arnold Sommerfeld** [1868-1951]. In electrostatics, the electric potential is directly equal to 0 at infinity, $\lim_{R\to\infty} \phi = 0$. Waves generated from the motion of floating body will radiate to the outside, and in the case of three dimensions, as column surface waves, the width of the divergent wave is $A \propto \frac{1}{\sqrt{R}}$, by wave equation:

$$\lim_{R\to\infty} \sqrt{R}\left(\frac{\partial \Phi}{\partial R} + \frac{1}{C}\frac{\partial \Phi}{\partial t}\right) = 0 \tag{3.12}$$

4. Floating body surface condition

Radiation and diffraction phenomena occur at the same location and at the same time on the surface in contact with the floating body and the fluid under the influence of the incident wave. But according to the approach proposed by **Haskind**, the velocity potential ϕ is expressed as three parts: first part, ϕ_0 is the incident wave potential; second part; ϕ_D is the scattered wave potential as the diffraction problem; third part, ϕ_R is the scattered wave potential as the radiation problem.

In the case of diffraction, diffraction potential ϕ_D represents the perturbation of the incident wave flow field by the existence of a fixed object, it is treated as a total reflection:

$$\frac{\partial \phi_D}{\partial n} = -\frac{\partial \phi_0}{\partial n} \tag{3.13}$$

In the case of radiation, radiation potential ϕ_R represents it is only related to the normal speed of points on the surface of the floating body when the floating body oscillates. And there are no relations with diffraction potential ϕ_D and incident potential ϕ_0. It's like a floating body forced to do forced oscillatory motion on free surface of still water.

$$\frac{\partial \phi_R}{\partial n} = \sum_{j=1}^{6} v_j n_j \tag{3.14}$$

where, v_j is the j mode motion complex amplitude of rigid body motion with 6 DOFs, surge, sway, heave, roll, pitch, yaw, n_j is the object normal vector related to the mode of motion.

$$\left.\begin{matrix} n_1 \\ n_2 \\ n_3 \end{matrix}\right\} = \boldsymbol{n}, \qquad \left.\begin{matrix} n_4 \\ n_5 \\ n_6 \end{matrix}\right\} = (\boldsymbol{r} - \boldsymbol{r_G}) \times \boldsymbol{n} \tag{3.15}$$

where, $\boldsymbol{n}$ is the outward unit normal vector of the floating surface, $\boldsymbol{r}$ and $\boldsymbol{r_G}$ are the position vector of the point on the surface of the floating body and the center of gravity of the floating body.

So far, the model describing the steady-state periodic motion problem of the three-dimensional speedless floating body has been constructed. Although the characteristic of the

governing equation is linear and there is no relationship between governing equation and time, there are relationships between time and two boundary conditions: the free surface condition and the distant condition. The governing equation is not complicated, but the boundary conditions are very complicated. That means that the nature of this problem is still related to the history of motion, and initial conditions need to be specified. To make this differentiation scheme easier to solve, the seakeeping problem is seen as a linear system, the output response becomes steady-state after a steady frequency ω oscillating input has passed enough time. At this time, space-time can be separated [47].

$$\phi(x,y,z,t) = \mathrm{Re}\{\phi(x,y,z)e^{-i\omega t}\} \tag{3.16}$$

When the value of ω=1, I calculated the $e^{-i\omega t}$, that is drawn from t=0 to t=20:

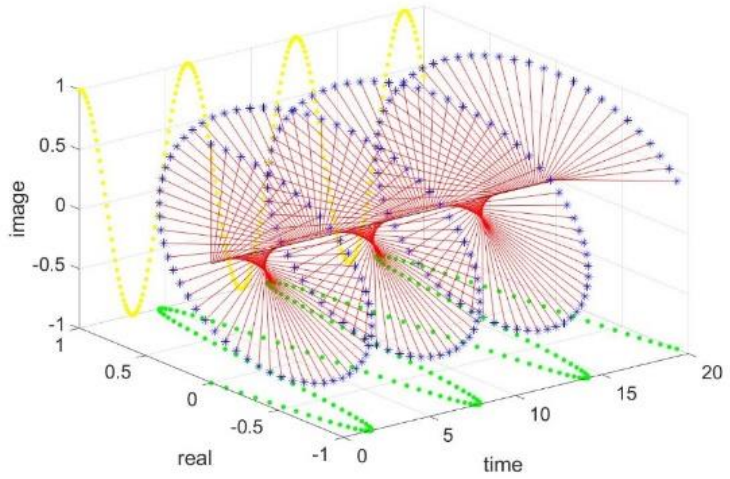

Fig. 3.1 The 3D screen of $e^{-i\omega t}$

Finally, the linear free surface condition can be simplified to as follows:

$$\frac{\partial\phi}{\partial z} - \frac{\omega^2}{g}\phi = 0 \ \ (z=0) \tag{3.17}$$

Because of $\frac{\omega}{C} = k$, C is wave speed, k is wave number, the distant condition can be simplified to as follows at last:

$$\lim_{R\to\infty}\sqrt{R}\left(\frac{\partial\phi}{\partial R} - ik\phi\right) = 0 \tag{3.18}$$

3.1.3 The Solution of Formulation

1. Incident wave potential

$$\begin{cases} \nabla^2\phi_0 = 0 & \text{(control equation)} \\ \dfrac{\partial\phi_0}{\partial z} - \dfrac{\omega^2}{g}\phi_0 = 0 \qquad (z=0) & \text{(free surface condition)} \\ \dfrac{\partial\phi_0}{\partial z} = 0 \qquad (z=\text{-}h) & \text{(seabed condition)} \\ \lim\limits_{R\to\infty}\left(\dfrac{\partial\phi_0}{\partial R} - ik\phi_0\right) = 0 & \text{(distant condition)} \end{cases} \tag{3.19}$$

This differential equation group can be solved using the separation of variables method. The incident wave potential of the frequency can be show by dispersion relation formula $\omega^2 = kg \cdot \tanh\ kh$.

$$\begin{aligned} \phi_0(x,y,z) &= \frac{A}{i\omega} g \times \frac{\cosh k(z+h)}{\cosh kh} e^{ik(x\cos\beta + y\sin\beta)} \\ &= \frac{A\omega}{ik} \frac{\cosh k(z+h)}{\sinh kh} e^{ik(x\cos\beta + y\sin\beta)} \end{aligned} \tag{3.20}$$

It should be noted that the fluid particle itself does not rotate, but the orbital equation of the fluid particle is

$$\frac{(x\cos\beta + y\sin\beta)^2}{\left(\frac{A\cosh k(z_0+h)}{\sinh kh}\right)^2} + \frac{z^2}{\left(\frac{A\sinh k(z_0+h)}{\sinh kh}\right)^2} = 1 \tag{3.21}$$

Consequently, it's an elliptical orbit at finite water depth and a circular orbit at infinite water depth. The fluid wave is not a simple transverse wave or longitudinal wave, which is the **Rayleigh** waves that a type of surface acoustic wave. In the vertical direction, its amplitude decreases exponentially with increasing distance from the surface, with a phase difference between motions. In the horizontal direction, when the wave propagates from left to right, the in-plane motion of the particle is counterclockwise; its in-plane amplitude is only attenuated by $\frac{1}{\sqrt{R}}$; its propagation speed depends on the wavelength, as formula $C = \sqrt{\frac{g}{k}\tanh\ kh}$, waves of longer wavelengths (low frequencies) travel faster than waves of shorter wavelengths (high frequencies).

2. Reflected wave

2.1. Radiation problem

After space-time are separated, $v_j = \mathrm{Re}\{-i\omega x_j e^{-i\omega t}\}$, radiation potential ϕ_R can be expressed as:

$$\frac{\partial\phi}{\partial n} = -i\omega \sum_{j=1}^{6} x_j n_j \tag{3.22}$$

and if a unit radiation potential $\phi_R(x,y,z) = -i\omega \sum_{j=1}^{6} x_j \phi_j(x,y,z)$ is introduced, radiation potential ϕ can be expressed as:

$$\frac{\partial \phi_j}{\partial n} = n_j \tag{3.23}$$

Therefore,

$$\begin{cases} \nabla^2 \phi_j = 0 & \text{(control equation)} \\ \dfrac{\partial \phi_j}{\partial z} - \dfrac{\omega^2}{g}\phi_j = 0 \quad (z=0) & \text{(free surface condition)} \\ \dfrac{\partial \phi_j}{\partial n} = n_j & \text{(surface condition of floating body)} \\ \dfrac{\partial \phi_j}{\partial z} = 0 \quad (z=-h) & \text{(seabed condition)} \\ \lim\limits_{R\to\infty} \sqrt{R}\left(\dfrac{\partial \phi_j}{\partial R} - ik\phi_j\right) = 0 & \text{(distant condition)} \end{cases} \tag{3.24}$$

For solving this group of differential equations, the numerical solution method must be used. Commonly used methods are FEM (finite element method), difference method, series expansion method (multi-pole expansion method), eigenfunction expansion method, domain decomposition method [48] and boundary element method. Among them, the boundary element method is used in this paper.

If the solution of the differential equation satisfies the governing equation in the region, and does not require precise satisfaction of the boundary conditions. Using the **Green** formula to transform the differential equation of the solving region into an integral equation of the boundary. Then discrete on the boundary (usually divide the boundary surface discrete into quadrilateral elements), selecting the appropriate interpolation function-**Green**'s function $G(P;Q)$, and change the integral equation of the boundary into a set of algebraic equations, so as to obtain the numerical solution of the problem on the boundary.

By the **Green** third formula derived by **Gaussian** formula $\iiint_V \nabla \cdot \boldsymbol{A} dV = \iint_S \boldsymbol{n} \cdot \boldsymbol{A} dS$, when point $P \in S$, and S is all the boundaries of the solution region.

$$\phi(P) = -\frac{1}{2\pi}\iint_S \left[\phi(Q)\frac{\partial G(P;Q)}{\partial n} - G(P;Q)\frac{\partial \phi(Q)}{\partial n}\right] dS_Q \tag{3.25}$$

If the boundary S meets **Nuamann** boundary condition $\frac{\partial \phi(P)}{\partial n}$:

$$\phi(P) = \frac{1}{4\pi}\iint_S \left[\sigma(Q)G(P;Q)\right] dS \tag{3.26}$$

$$\frac{\partial \phi(P)}{\partial n} = \frac{1}{2}\sigma(P) + \frac{1}{4\pi}\iint_S \left[\sigma(Q)\frac{\partial G(P;Q)}{\partial n}\right] dS \tag{3.27}$$

Equation 3.26 is the first kind of **Fredholm** integral equation, and equation 3.27 is the second kind of **Fredholm** integral equation, the left term has been given as a known value on the boundary. It is called one layer potential (point source distribution).

If the boundary S meets **Dirichlet** boundary condition $\phi(P)$:

$$\phi(P)=\frac{1}{4\pi}\iint_S\left[m(Q)\frac{\partial G(P;Q)}{\partial n}\right]dS-\frac{1}{2}m(P) \tag{3.28}$$

This is the second kind of **Fredholm** integral equation, the left term has been given as a known value on the boundary. It is called double layer potential (dipole distribution).

In addition to the free surface condition and distant condition belonging to the third type of boundary conditions, the other boundary conditions belong to **Neumann** boundary condition, which gives the normal derivative value on the boundary, usually one layer potential (point source distribution $\sigma(Q)$) is used.

Green's function $G(P;Q)$ is aliased as point source function or influence function. A **Green**'s function $G(P;Q)$ is the response to an impulse force, representing the field and influence of a point source under specific boundary conditions or initial value conditions. Because the field generated by arbitrarily distributed sources can be viewed as a superposition of fields generated by many point sources, any force can be analyzed by putting together the responses of individual impulses. Once the **Green**'s function $G(P;Q)$ is found, the field of an arbitrarily distributed source can be found.

Green's function $G(P;Q)$ can be a solution that not only satisfies the definition of the basic solution of the differential equation, but also satisfies certain boundary conditions on the boundary S of the solution domain V. For a given boundary problem of an infinite region or half-space infinite region of partial differential equations, using the basic solution of the differential equation or the point source defined in fluid mechanics, the boundary conditions of the problem can be satisfied by the superposition of basic solutions, and the field function that meets the boundary conditions induced by the source intensity $\sigma(Q)$ of a certain density distribution in the infinite region or the half-space infinite region that is the solution of the problem in the region. However, for a given boundary problem in a limited domain of partial differential equations, the solution of **Green**'s function $G(P;Q)$ will be much more difficult. Depending on the specific situation, mirror method, mode expansion method, **Fourier** method may be used.

Green's function theory can be used not only to solve homogeneous linear differential equations, but also an effective method to solve inhomogeneous linear differential equations. In physical, the non-homogeneous term of the linear differential equation indicates external disturbances, but the differential equation satisfied by the **Green**'s function $G(P;Q)$ will degenerate into a homogeneous equation when $P\neq Q$, so the **Green**'s function $G(P;Q)$ only depends on the boundary value conditions, and has nothing to do with inhomogeneous terms

of the linear differential equation. When constructing the **Green**'s function $G(P;Q)$, it is enough to derive the differential equations and boundary value conditions that the **Green**'s function $G(P;Q)$ should satisfy.

The attribute of **Green**'s function $G(P;Q)$: [49]

1). **Green**'s function satisfies the equation $\nabla^2\phi = 0$ everywhere except for point $P = Q$, when $P \to Q$, $G(P;Q) \to +\infty$.

2). At the border $\partial\Omega$, $G(P;Q) = 0$.

3). In the area Ω, $0 < G(P;Q) < \frac{1}{4\pi r(P;Q)}$.

4). $\iint_{\partial\Omega} \frac{\partial G}{\partial n} dS = -1$.

5). **Green**'s function has symmetry, which is for $\forall P;Q \in \Omega$, $G(P;Q) = G(Q;P)$. It is also called the reciprocity theorem.

If **Green**'s function $G(P;Q)$ only satisfies the definition of the basic solution of the governing equation of inviscid, non-rotating and incompressible fluid $\nabla^2\phi = 0$:

$$G(P;Q) = \frac{1}{r(P;Q)} \tag{3.29}$$

Under these circumstances, all four boundary conditions must be integrated, this is the Rankine source method. But if **Green**'s function $G(P;Q)$ satisfies all boundary conditions except the surface condition of floating body,

$$\begin{cases} \nabla^2 G(P;Q) = \delta(P-Q) & \text{(control equation)} \\ \dfrac{\partial G}{\partial z} - \dfrac{\omega^2}{g} G = 0 \quad (z=0) & \text{(free surface condition)} \\ \dfrac{\partial G}{\partial z} = 0 \quad (z=-h) & \text{(seabed condition)} \\ \lim\limits_{R\to\infty}\left(\dfrac{\partial G}{\partial R} - ikG\right) = 0 & \text{(distant condition)} \end{cases} \tag{3.30}$$

It is only necessary to distribute the source and dipoles on the surface condition of floating body, this is the three-dimensional free surface **Green**'s function method.

$$G(P;Q) = \frac{1}{r(P;Q)} + G^*(P;Q) \tag{3.31}$$

Using the **Fourier** multiple integral,

$$G(P;Q) = \frac{1}{r(P;Q)} = \frac{1}{2\pi}\int_0^{\infty}\int_{-\pi}^{\pi} e^{-k|z|} e^{ik(x\cos\theta + y\sin\theta)} d\theta dk \tag{3.32}$$

Green's function $G(P;Q)$ has first-order singularity and high-frequency oscillation near the singular point, and the partition series method was proposed by **Newman**. When the velocity of the floating body = 0, series and integral indications are as follows:

when $kR \geq 0.1$:

$$-4\pi G(P;Q)=\frac{2\pi(K^2-k^2)}{k^2h-K^2h+K}\cosh k(p_3+h)\cosh k(q_3+h)\{Y_0(kR)-iJ_0(kR)\}+4\sum_{n=1}^{\infty}\frac{(K^2+k_n{}^2)}{k_n{}^2h+K^2h-K}\cos k_n(p_3+h)\cos k_n(q_3+h)K_0(k_nR) \tag{3.33}$$

when $kR \leq 0.1$:

$$-4\pi G(P;Q)=\frac{1}{r}+\frac{1}{r_1}+2P.V.\int_0^{\infty}\frac{(\mu+K)e^{-\mu h}\cosh\mu(p_3+h)\cosh\mu(q_3+h)J_0(\mu R)}{\mu\sinh\mu h-K\cosh\mu h}d\mu+i\frac{2\pi(k^2-K^2)\cosh k(p_3+h)\cosh k(q_3+h)J_0(kR)}{k^2h-K^2h+K} \tag{3.34}$$

where, $P=(p_1,p_2,p_3)$, $Q=(q_1,q_2,q_3)$, $K=\frac{\omega^2}{g}$, J_0 is the first-type **Bessel** function for integer orders = 0, Y_0 is a second-type **Bessel** function for integer orders = 0, and K_0 is a second-type modified **Bessel** function for integer orders = 0. Moreover:

$$\omega^2=kg\cdot\tanh kh \quad \text{(progressing wave)} \tag{3.35}$$

$$\omega^2=-k_ng\cdot\tan k_nh \quad \text{(local wave)} \tag{3.36}$$

$$r=\sqrt{(p_1-q_1)^2+(p_2-q_2)^2+(p_3-q_3)^2} \tag{3.37}$$

$$r_1=\sqrt{(p_1-q_1)^2+(p_2-q_2)^2+(p_3+2h+q_3)^2} \tag{3.38}$$

$$R=\sqrt{(p_1-q_1)^2+(p_2-q_2)^2} \tag{3.39}$$

$P.V.$ means that the integral takes a **Cauchy** principal value [50].

I calculated the **Green**'s function $G(P;Q)$ when ω=1rad/s, $P=(p_1,0,0)$ and $Q=(0,0,1)$, p_1 changes from 1 to 100 using MATLAB software:

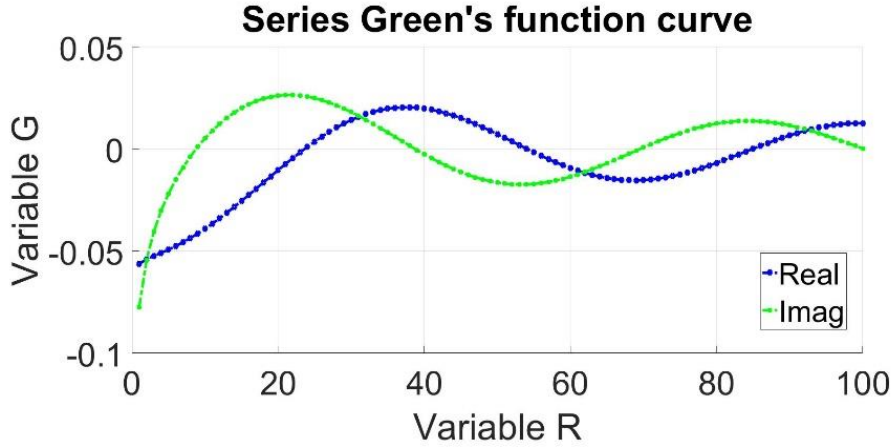

Fig. 3.2 Calculation example of **Green**'s function of series formula

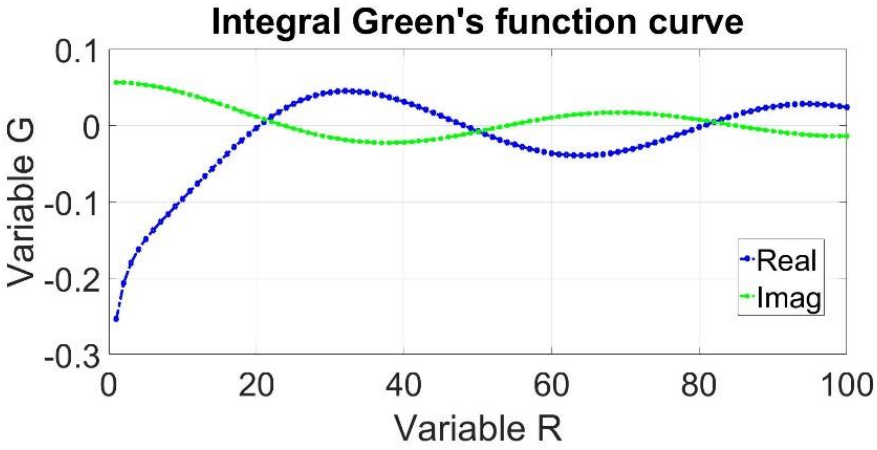

Fig. 3.3 Calculation example of the **Green**'s function of the integral formula

The significant advantage of this method is that it transforms the definite solution problem with arbitrary non-homogeneous terms and boundary values into solving a specific boundary value problem, making it only dependent on the differential operator, the form of the boundary conditions and the shape of the region. It is possible to study both bounded problems and unbounded problems. Its calculation workload is small, the calculation accuracy is high, and the adaptability is strong.

Once the **Green**'s function $G(P;Q)$ is got, put the boundary integral equation on the surface condition of floating body discretize a set of linear algebraic equations to solve (panel method).

$$n_{jn}\left(P_n\right)=\frac{1}{2}\sigma_n\left(P_n\right)+\frac{1}{4\pi}\sum_{\substack{i=1\\ i\neq n}}^{N}\iint_{\Delta S_i}\left[\sigma_i\left(Q\right)\frac{\partial G\left(P_n;Q_i\right)}{\partial n}\right]dS_{Q_i}\quad\left(n=1,2,\cdots\cdots,N\right)\qquad(3.40)$$

After the $\sigma_i(Q)$ is acquired, the radiation potential $\phi_{jn}(P_n)$ can be obtained by the following equation.

$$\phi_{jn}\left(P_n\right)=\frac{1}{4\pi}\sum_{\substack{i=1\\ i\neq n}}^{N}\iint_{\Delta S_i}\left[\sigma_i\left(Q\right)G\left(P_n;Q_i\right)\right]dS_{Q_i}\qquad(3.41)$$

2.2. Diffraction problem

$$\begin{cases} \nabla^2\phi_D = 0 & \text{(control equation)} \\ \dfrac{\partial\phi_D}{\partial z} - \dfrac{\omega^2}{g}\phi_D = 0 \quad (z=0) & \text{(free surface condition)} \\ \dfrac{\partial\phi_D}{\partial n} = -\dfrac{\partial\phi_0}{\partial n} & \text{(surface condition of floating body)} \\ \dfrac{\partial\phi_D}{\partial z} = 0 \quad (z=-h) & \text{(seabed condtion)} \\ \lim\limits_{R\to\infty}\sqrt{R}\left(\dfrac{\partial\phi_D}{\partial R} - ik\phi_D\right) = 0 & \text{(distant condition)} \end{cases} \tag{3.42}$$

Comparing the equation 3.42 with equation 3.24, apart from the surface condition of floating body is different, the other conditions are all same. Consequently, the **Green**'s function $G(P;Q)$ used for solving the radiation problem can also be used in solving the diffraction problem. Just need to change the left term of boundary integral equation on the surface condition of floating body.

In addition, when the initial velocity of floating body is 0, the **Haskind** equation (**Haskind** relation) can give the diffraction potential ϕ_D from the incident wave potential ϕ_0 and the radiation potential ϕ_j [51].

$$\iint_{S_0}\phi_D\cdot n_j ds = \iint_{S_0}\phi_D\cdot\frac{\partial\phi_j}{\partial n}ds = \iint_{S_0}\phi_j\cdot\frac{\partial\phi_D}{\partial n}ds = -\iint_{S_0}\phi_j\cdot\frac{\partial\phi_0}{\partial n}ds \tag{3.43}$$

3.1.4 The Motion Equation in Frequency Domain

Once obtained the velocity potential, we can get the hydrodynamic parameters and hydrodynamic force. The equation of the ideal fluid motion is first derived by **Euler** according to the principle of conservation of momentum, is a part of **Euler** equation in hydrodynamics.

$$\frac{d\boldsymbol{v}}{dt} = \frac{\partial\boldsymbol{v}}{\partial t} + (\boldsymbol{v}\cdot\nabla)\boldsymbol{v} = -\nabla\left(\frac{\boldsymbol{p}}{\rho} + gz\right) \tag{3.44}$$

For non-rotational non-viscosity incompressible ideal fluid, the **Lagrange** integral formula can be derived from the above formula.

$$\frac{\boldsymbol{p}}{\rho} + gz + \frac{\boldsymbol{v}}{2} + \frac{\partial\phi}{\partial t} = c(t) \tag{3.45}$$

This equation is actually an equation of the law of conservation of mechanical energy of fluid. The dynamic pressure $\boldsymbol{p}$ can be obtained by Equation 3.45 after omitting the nonlinear term.

$$\boldsymbol{p} = -\rho\frac{\partial\phi}{\partial t} \tag{3.46}$$

Then, dynamic fluid force can be obtained:

$$\boldsymbol{F_{Wj}} = -\rho \iint_{S_0} \frac{\partial \boldsymbol{\phi}}{\partial t} \boldsymbol{n}_j dS \tag{3.47}$$

The force $\boldsymbol{F_{Wj}^R}$ caused by the radiation potential is as follows:

$$\boldsymbol{F_{Wj}^R} = \mathrm{Re}\left\{ \omega^2 \sum_{k=1}^{6} x_k \rho \iint_{S_0} \phi_k \frac{\partial \phi_j}{\partial n} dS \cdot e^{-i\omega t} \right\} \tag{3.48}$$

Introducing the symbol of $\mu_{jk} + \frac{i\lambda_{jk}}{\omega} = \rho \iint_{S_0} \phi_k \frac{\partial \phi_j}{\partial n} dS \quad (j,k = 1 \sim 6)$, then

$$\boldsymbol{F_{Wj}^R} = -\sum_{k=1}^{6} \left(\ddot{x}_k \mu_{jk} + \dot{x}_k \lambda_{jk} \right) \quad (j = 1 \sim 6) \tag{3.49}$$

Where, μ_{jk} is called the added mass, is also called as **Newton**'s zeroth law in which the additivity of mass, and is caused by the inertia force because of the movement of the surrounding flow field of the floating body. The added mass force corresponds to the standing wave near the floating body, when the submersion depth of the floating body floating on the water surface changes, the added mass will change, and the shape of the standing wave near the floating body will also changes due to the movement. In addition, if the frequency of motion is different, the shape of the standing wave near the floating body that accompanies the motion will also changes. λ_{j_k} is called the damping coefficient, is caused by the existence of free surface condition. The damping force corresponds to the divergent wave whose wave-making diverges outward.

The scattering wave force can be obtained by combining the incident wave potential and the diffraction potential.

$$\boldsymbol{F_{Wj}^k} = i\omega\rho \iint_{S_0} \phi_0 \frac{\partial \phi_j}{\partial n} dS \tag{3.50}$$

$$\boldsymbol{F_{Wj}^D} = i\omega\rho \iint_{S_0} \phi_D \frac{\partial \phi_j}{\partial n} dS \tag{3.51}$$

The wave force $\boldsymbol{F_{Wj}^k}$ caused by the incident wave potential is called **Froude-Krylov** force, which is obtained without considering the influence of the floating body on the flow field of the incident wave. The force $\boldsymbol{F_{Wj}^D}$ caused by the diffraction potential is called diffraction force.

At this moment, the displacement of floating body $x_j(t)$, the velocity $\dot{x}_j(t)$, the acceleration $\ddot{x}_j(t)$ and the external wave force $F_i(t)$ in a stable steady state can be expressed as $x_j(t) = \mathrm{Re}\{x_j e^{-i\omega t}\}$, $\dot{x}_j(t) = \mathrm{Re}\{-i\omega x_j e^{-i\omega t}\}$, $\ddot{x}_j(t) = \mathrm{Re}\{-\omega^2 x_j e^{-i\omega t}\}$, $F_i(t) = \mathrm{Re}\{f_i e^{-i\omega t}\}$, so the motion equation of floating body under the steady frequency ω regular waves in the frequency domain is as follows:

$$\sum_{i,j=1}^{6}\{-\omega^2(m_{ij}+\mu_{ij})-i\omega\lambda_{ij}+C_{ij}\}x_j=f_i \tag{3.52}$$

where, m_{ij} is the mass matrix, C_{ij} is the restoring force coefficient matrix, and f_i is the scattering wave force contained the **Froude-Krylov** force and the diffraction force. The motion equation of floating body in DOFs of surge, sway and heave is similar to the forced compulsory motion of a harmonic oscillator. The motion equation of floating body in DOFs of roll, pitch and yaw is similar to the forced compulsory motion of a simple pendulum that can produce chaotic phenomena although it is not as obvious as the chaotic motion of a double pendulum. But its motion is predictable under certain assumptions. Then:

$$x_j(\omega)=\frac{f_i}{\sum_{i,j=1}^{6}\{-\omega^2(m_{ij}+\mu_{ij})-i\omega\lambda_{ij}+C_{ij}\}} \tag{3.53}$$

$x_j(\omega)$ is a complex number, called the transfer function, contain the Response Amplitude Operators (**RAO**) and phase difference.

3.1.5 The Motion Equation in Time Domain

The vibration response under the unit impulse excitation (**Dirac** delta function) is called the unit impulse response function. The excitation frequency range of the ideal unit impulse load is infinite. As the response under unit impulse excitation, the unit impulse response function contains all the dynamic characteristic parameters of the vibration system. Using **Duhamel** integral, the vibration response of the system under the excitation of general non-periodic dynamic load can be obtained. Therefore, under the action of an unit impulse function, the response of the system can be expressed as an unit impulse response function $h(t)$. If the system is under the action of a continuous force function $f(t)$, its response can be obtained by **Duhamel** integral. The basic principle of **Duhamel** integration is to use a series of rectangular pulse functions with a time interval of $\Delta\tau$ to approximately replace the role of $f(t)$, and its response can be obtained by the superposition of this series of impulse responses.

$$\sum_{i,j=1}^{6}(m_{ij}+\mu_{ij}(\infty))\ddot{x}_j(t)+\int_{-\infty}^{t}K_{ij}(t-\tau)\dot{x}_j(\tau)d\tau+C_{ij}x_j(t)=F_i(t) \tag{3.54}$$

where, damping term is the convolution integral of retardation function $K_{ij}(t)$ and $\dot{x}_j(t)$, reflects the memory effect exist in the hydrodynamic reaction force [52].

$$\begin{aligned}K(\tau)&=\frac{2}{\pi}\int_0^{\infty}\lambda(\omega)\cos\omega\tau d\omega\\ \mu(\omega)&=\mu(\infty)+\frac{1}{\omega}\int_0^{\infty}\lambda(\tau)\sin\omega\tau d\omega\end{aligned} \tag{3.55}$$

$x_j(t)$ and $\dot{x}_j(t)$ can be calculated by **Newmark**'s method.

$$\dot{x}(t+\Delta t)=\dot{x}(t)+b_6\ddot{x}(t)+b_7\ddot{x}(t+\Delta t)$$
$$x(t+\Delta t)=x(t)+\Delta t\dot{x}(t)+b_8\ddot{x}(t)+b_9\ddot{x}(t+\Delta t) \tag{3.56}$$

where,

$$b_6=\Delta t\left(1-\delta\right)\quad b_7=\Delta t\delta\quad b_8=\Delta t^2\left(\frac{1}{2}-\alpha\right)$$
$$b_9=\Delta t^2\alpha\quad \alpha=0.25\left(0.5+\delta\right)^2\quad \delta=0.50002 \tag{3.57}$$

3.2 The Response in Irregular Wave

In fact, the waves at the actual sea state mainly due to the wind blowing are irregular waves, is a complex random process. However, from the perspective of **Fourier**, irregular waves are a superposition of regular waves with different frequency, different amplitude and different phase. Probability theory and mathematical statistics are used for the study of irregular waves.

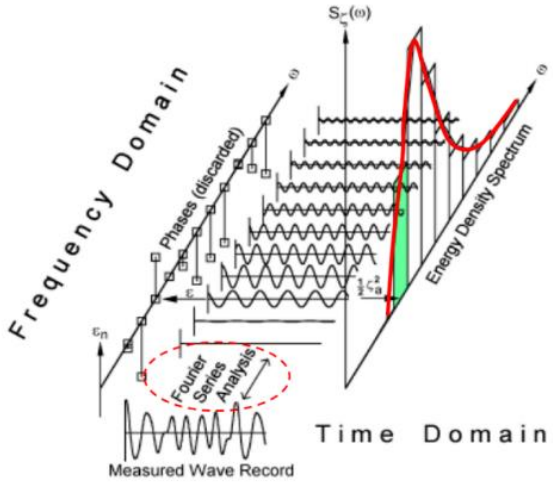

Fig. 3.4 Relationship between regular and irregular waves from the perspective of **Fourier** [53]

In accordance with **Longuet-Higgins** statistics, the displacement of the wave surface at a fixed point can be expressed as the following random process:

$$\xi(t)=\sum_{i=1}^{n}\varsigma_{ai}\cos(\omega_i t+\varepsilon_i) \tag{3.58}$$

ε_i is a random phase evenly distributed in $0\sim 2\pi$, the mean value of the random process $\xi(t)$ is zero, the autocorrelation function $R_{\zeta\zeta}(t)$ only depends on the time interval. The irregular wave is defined by means of the wave spectrum $S_\zeta(\omega)$, the spectral density function $S_{\zeta\zeta}(\omega)$ reflects the distribution state of wave energy, and the integrated area of the spectral density function $S_{\zeta\zeta}(\omega)$ is the average wave energy. Between the autocorrelation function and the spectral density function exist **Fourier** transform relationship that is also called **Wiener-**

Khintchine theorem. The expected value θ_{pitch} of hydrodynamic response during the irregular wave can be calculated making use of the **RAO** of regular waves and the spectral density function $S_{\zeta\zeta}(\omega)$. Finally, the expected value θ_{pitch} is calculated by the integrated amount of floating body response spectrum $S_z(\omega)$.

$$E[\zeta^2(x,y,t)] = \int_0^\infty S_\zeta(\omega)d\omega \tag{3.59}$$

$$S_{\zeta\zeta}(\omega) = \frac{2}{\pi}\int_0^\infty R_{\zeta\zeta}(\tau)cos\ (\omega\tau)d\tau \tag{3.60}$$

$$S_z(\omega) = |RAO(\omega)|^2 S_{\zeta\zeta}(\omega) \tag{3.61}$$

$$\theta_{pitch} = \sqrt{2\int_0^\infty S_z(\omega)d\omega} \tag{3.62}$$

The spectral density function $\Phi_{\zeta\zeta}(\omega)$ in this paper is the **Pierson-Moskowitz** (**P-M**) spectrum.

$$\Phi_{\zeta\zeta}(\omega) = \frac{\alpha g^2}{\omega^5} e^{-\beta\left(\frac{g}{\omega V}\right)^4} \tag{3.63}$$

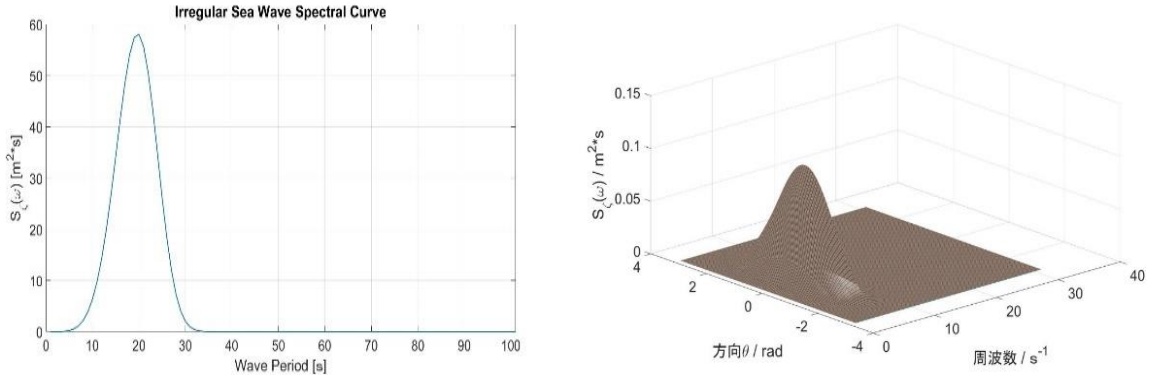

Fig. 3.5 The P-M spectrum

Define the spectral moment m_n to express the characteristic quantity of the spectrum in a certain aspect. The 0-order spectral moment m_0 equal to the variance of the wave surface displacement, the 2-order spectral moment m_2 equal to the variance of velocity, the 4-order spectral moment m_4 equal to the variance of acceleration.

$$m_n = \int_0^\infty \omega^n S_\zeta(\omega)d\omega \tag{3.64}$$

Average period is

$$\overline{T} = 2\pi\sqrt{\frac{m_0}{m_2}} \tag{3.65}$$

Average wave height is

$$\overline{h} = 2.5\sqrt{m_0} \tag{3.66}$$

Significant wave height is

$$\overline{h}_{1/3} = 4.0\sqrt{m_0} \tag{3.67}$$

3.3 The Spinning Top in Torus Structure

This paper gets better seakeeping through rotating motion. The inside of the torus can not only be placed with solid that can rotate, but also can be filled with liquids to make it rotate. For example, laying rails at the torus bottom, placing trams driven by electricity generated from FOWT on the rails in the four bearing of east, west, south and north for balance and at the same time evacuating the air inside the torus to reduce friction force. Replacing solids with liquids, it does not need to consider the issue of balance.

In 2013, the strange behavior of liquid metal that can move autonomously at high speed and deform after swallowing a small amount of aluminum was discovered for the first time in the world [54], because of the richness of materials in this world, an annular flow in the torus structure has many unexpected possibilities.

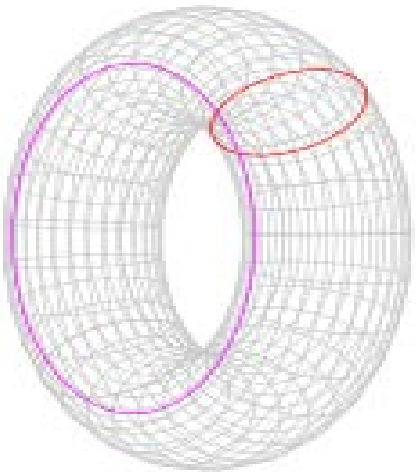

Fig. 3.6 The torus structure

Moment of inertia of the torus structure is:

About diameter:

$$\frac{1}{8}(4a^2 + 5b^2)m \tag{3.68}$$

About the vertical axis:

$$(a^2 + \frac{3}{4}b^2)m \tag{3.69}$$

where, the distance from the center of ring tube section to the center of torus is the radius of torus that is a, the radius of ring tube section is b, and m is the mass of torus structure. Then using the parallel shift theorem of moment of inertia $J_B = J_A + md^2$ to convert to the space fixed coordinate system $o_0x_0y_0z_0$, d is the distance between A axis and B axis.

Next, the responses of the pitch, roll and yaw DOFs are expressed within the range of linear theory, deducing two kinds of moments generated by the axial retention effect due to the

rotating motion and the gyroscopic effect because of the precession motion based on the conservation law of angular momentum [55].

1. The axial retention effect

When the rigid body rotates, it should have an axial retention effect from the conservation principle of angular momentum. The moment of the rotating rigid body that makes a rotational motion is as follows:

$$\boldsymbol{M} = \frac{\mathrm{d}\boldsymbol{L}}{\mathrm{d}t} \tag{3.70}$$

where, $\boldsymbol{M}$ is the moment of force under external force; $\boldsymbol{L}$ is the angular momentum of rotating rigid body, and $\boldsymbol{L} = \boldsymbol{r} \times \boldsymbol{p} = J \cdot \boldsymbol{\omega}$, $\boldsymbol{r}$ is the position vector of the rotating rigid body particle relative to coordinate origin, $\boldsymbol{p}$ is the momentum of rotating rigid body, J is moment of inertia and $\boldsymbol{\omega}$ is the angular velocity of rotating rigid body. Then:

$$\boldsymbol{M} = \frac{\mathrm{d}\boldsymbol{L}}{\mathrm{d}t} = J\frac{\mathrm{d}\boldsymbol{\omega}(t)}{\mathrm{d}t} \tag{3.71}$$

At this time, the rotating rigid body under external moment of force in a stable steady state, the moment generated from the rotational motion of the rotating rigid body will become a stable steady swaying state. Therefore, the angular velocity of the rotating rigid body $\boldsymbol{\omega}(\boldsymbol{t})$ is as follows:

$$\begin{cases} \omega_{xr}(t) = \mathrm{Re}[\omega_{xr}x_j e^{-i\omega t}] \\ \omega_{yr}(t) = \mathrm{Re}[\omega_{yr}x_j e^{-i\omega t}] \\ \omega_{zr}(t) = \mathrm{Re}[\omega_{zr}x_j e^{-i\omega t}] \end{cases} \tag{3.72}$$

Substituting Equation 3.72 into Equation 3.71:

$$\begin{cases} M_4 e^{-i\omega t} = J_{xx}\frac{\mathrm{d}\omega_{xr}(t)}{\mathrm{d}x} = -i\omega J_{xx}\omega_{xr}x_j e^{-i\omega t} \\ M_5 e^{-i\omega t} = J_{yy}\frac{\mathrm{d}\omega_{yr}(t)}{\mathrm{d}x} = -i\omega J_{yy}\omega_{yr}x_j e^{-i\omega t} \\ M_6 e^{-i\omega t} = J_{zz}\frac{\mathrm{d}\omega_{zr}(t)}{\mathrm{d}x} = -i\omega J_{zz}\omega_{zr}x_j e^{-i\omega t} \end{cases} \tag{3.73}$$

In other words:

$$\begin{cases} M_4 e^{-i\omega t} = -i\omega J_{xx}\omega_{xr}x_4 e^{-i\omega t} - i\omega J_{yy}\omega_{yr}x_4 e^{-i\omega t} - i\omega J_{zz}\omega_{zr}x_4 e^{-i\omega t} \\ M_5 e^{-i\omega t} = -i\omega J_{xx}\omega_{xr}x_5 e^{-i\omega t} - i\omega J_{yy}\omega_{yr}x_5 e^{-i\omega t} - i\omega J_{zz}\omega_{zr}x_5 e^{-i\omega t} \\ M_6 e^{-i\omega t} = -i\omega J_{xx}\omega_{xr}x_6 e^{-i\omega t} - i\omega J_{yy}\omega_{yr}x_6 e^{-i\omega t} - i\omega J_{zz}\omega_{zr}x_6 e^{-i\omega t} \end{cases} \tag{3.74}$$

Except the moment of own DOF, the other terms are written in the matrix form:

$$\begin{bmatrix} M_{4keep} \\ M_{5keep} \\ M_{6keep} \end{bmatrix} = -i\omega \begin{bmatrix} J_{yy}\omega_{yr} + J_{zz}\omega_{zr} & 0 & 0 \\ 0 & J_{xx}\omega_{xr} + J_{zz}\omega_{zr} & 0 \\ 0 & 0 & J_{xx}\omega_{xr} + J_{yy}\omega_{yr} \end{bmatrix} \begin{bmatrix} x_4 \\ x_5 \\ x_6 \end{bmatrix} \tag{3.75}$$

This moment as a damping force is generated from the coupling effect of holding the axis of the rotating rigid body.

2. The gyroscopic effect

However, the conservation principle of angular momentum can be used only in the inertial

coordinate system. In order to use the conservation law of angular momentum, looking at the change in the angular momentum of rotating rigid body $\boldsymbol{L}$ from a fixed coordinate system (an inertial coordinate system) to a rotating coordinate system (a non-inertial coordinate system), then the motion equation of a rotating rigid body is derived as follows:

$$\boldsymbol{M} = J\frac{\mathrm{d}^{*}\boldsymbol{\omega}}{\mathrm{d}t} + \boldsymbol{\omega} \times (J \cdot \boldsymbol{\omega}) \tag{3.76}$$

where, $\frac{\mathrm{d}^{*}\boldsymbol{\omega}}{\mathrm{d}t} = \frac{\mathrm{d}\omega_{\mathrm{x}}}{\mathrm{d}t}\hat{x} + \frac{\mathrm{d}\omega_{\mathrm{y}}}{\mathrm{d}t}\hat{y} + \frac{\mathrm{d}\omega_{\mathrm{z}}}{\mathrm{d}t}\hat{z}$ is the angular acceleration in the rotating coordinate system, $\frac{\mathrm{d}\boldsymbol{\omega}}{\mathrm{d}t} = \frac{\mathrm{d}}{\mathrm{d}t}(\omega_{\mathrm{x}}\hat{x} + \omega_{\mathrm{y}}\hat{y} + \omega_{\mathrm{z}}\hat{z})$ is the angular acceleration in the fixed coordinate system. When unfolded and written in matrix form:

$$\begin{bmatrix} M_4 \\ M_5 \\ M_6 \end{bmatrix} = \begin{bmatrix} J_{xx} & 0 & 0 \\ 0 & J_{yy} & 0 \\ 0 & 0 & J_{zz} \end{bmatrix} \begin{bmatrix} \dot{\omega}_4 \\ \dot{\omega}_5 \\ \dot{\omega}_6 \end{bmatrix} + \begin{bmatrix} \omega_4 \\ \omega_5 \\ \omega_6 \end{bmatrix} \times \begin{bmatrix} J_{xx} & 0 & 0 \\ 0 & J_{yy} & 0 \\ 0 & 0 & J_{zz} \end{bmatrix} \begin{bmatrix} \omega_4 \\ \omega_5 \\ \omega_6 \end{bmatrix} \tag{3.77}$$

That is:

$$\begin{cases} M_4 = J_{xx}\dot{\omega}_4 - (J_{zz} - J_{yy})\omega_5\omega_6 \\ M_5 = J_{yy}\dot{\omega}_5 - (J_{xx} - J_{zz})\omega_4\omega_6 \\ M_6 = J_{zz}\dot{\omega}_6 - (J_{yy} - J_{xx})\omega_4\omega_5 \end{cases} \tag{3.78}$$

This motion equation of rotating rigid body is also called **Euler**'s equation of motion. When a rotating rigid body goes through sufficient time under a steady frequency ω oscillating input, it will all become a stable steady-state of swing, according to the vector addition theorem, the angular velocity of the rotating rigid body is as follows:

$$\omega_j(t) = \mathrm{Re}[\omega_{jr} - i\omega x_j e^{-i\omega t}] \tag{3.79}$$

ω_{jr} is the angular velocity of the rotating rigid body in j direction before the rotating rigid body become a stable steady-state of swing. Substituting Equation 3.79 into Equation 3.78:

$$\begin{cases} M_4 e^{-i\omega t} = -J_{xx}\omega^2 x_4 e^{-i\omega t} + (J_{zz} - J_{yy})(\omega_{yr} - i\omega x_5 e^{-i\omega t})(\omega_{zr} - i\omega x_6 e^{-i\omega t}) \\ M_5 e^{-i\omega t} = -J_{yy}\omega^2 x_5 e^{-i\omega t} + (J_{xx} - J_{zz})(\omega_{xr} - i\omega x_4 e^{-i\omega t})(\omega_{zr} - i\omega x_6 e^{-i\omega t}) \\ M_6 e^{-i\omega t} = -J_{zz}\omega^2 x_6 e^{-i\omega t} + (J_{yy} - J_{xx})(\omega_{xr} - i\omega x_4 e^{-i\omega t})(\omega_{yr} - i\omega x_5 e^{-i\omega t}) \end{cases} \tag{3.80}$$

Assuming that $x_4,\ x_5,\ x_6$ is small and when expanded and the squared term can be ignored:

$$\begin{cases} M_4 = -J_{xx}\omega^2 x_4 - (J_{zz} - J_{yy})(i\omega\omega_{yr}x_6 + i\omega\omega_{zr}x_5) \\ M_5 = -J_{yy}\omega^2 x_5 - (J_{xx} - J_{zz})(i\omega\omega_{xr}x_6 + i\omega\omega_{zr}x_4) \\ M_6 = -J_{zz}\omega^2 x_6 - (J_{yy} - J_{xx})(i\omega\omega_{xr}x_5 + i\omega\omega_{yr}x_4) \end{cases} \tag{3.81}$$

If the inertial part of the first term on the left side of Equation 3.81 is abbreviated and Equation 3.81 is written in the form of a matrix:

$$\begin{bmatrix} M_{4gyro} \\ M_{5gyro} \\ M_{6gyro} \end{bmatrix} = -i\omega \begin{bmatrix} 0 & (J_{zz} - J_{yy})\omega_{zr} & (J_{zz} - J_{yy})\omega_{yr} \\ (J_{xx} - J_{zz})\omega_{zr} & 0 & (J_{xx} - J_{zz})\omega_{xr} \\ (J_{yy} - J_{xx})\omega_{yr} & (J_{yy} - J_{xx})\omega_{xr} & 0 \end{bmatrix} \begin{bmatrix} x_4 \\ x_5 \\ x_6 \end{bmatrix} \tag{3.82}$$

This moment as a damping force arises from the gyroscopic effect and is called the

gyroscopic moment. The gyroscopic moment is obtained from the precession motion, a phenomenon in which the rotation axis of a rotating rigid body that rotates around another fixed axis. It is like the Coriolis force calculated by $\boldsymbol{F}_c = -2m(\boldsymbol{\omega} \times \boldsymbol{v})$, $\boldsymbol{\omega}$ is the angular velocity of the rotating reference frame, and $\boldsymbol{v}$ is the velocity of the object relative to the rotating reference frame.

In this way, the axial retention effect and the gyroscopic effect can be recognized as a damping term proportional to the angular velocity of external disturbance vibration by linearizing, and the greater the mass moment of inertia of the rotor, the greater the angular velocity of the rotor, the smaller the response to external interference. When the axial retention effect coefficient matrix $\boldsymbol{N_{keep}}$ and the gyroscopic effect coefficient matrix $\boldsymbol{N_{gyro}}$ are acquired, for a floating body with rotational motion internal under the steady frequency ω regular wave, the motion equation of the floating body in frequency domain can be expressed as follows in consideration of the axial retention effect and the gyroscopic effect:

$$\sum_{i,j=1}^{6} \left\{-\omega^2\left(m_{ij} + \mu_{ij}\right) - i\omega(\lambda_{ij} + N_{keepij} + N_{gyroij}) + C_{ij}\right\}x_j = f_i \qquad (3.83)$$

Therefore, once some important parameters of a floating body are treated as the input data of the above mathematical model, the output data of the hydrodynamic response of the floating body in the ocean can be got through numerical calculation.

Chapter 4:Comparison Calculation Based on Formalized Mathematical Model

4.1 Review the Validity of Formalization through Experiment

4.1.1 The Formulation of Simple Pendulum Verification Experimental

To verify the principle of the motion equation of the floating body in frequency domain in consideration of the axial retention effect, which act on the damping effect of the simple pendulum, a simple pendulum experiment to obtain the damping coefficient is carried out. The shape of the object under the rod is a large disk and the air resistance as damping effect is naturally occurring, a tube filled with water and linked with pump is surrounded by the disk, when the water in the tube flows, the damping effect will become bigger. The motion equation of the simple pendulum is obtained from the angular momentum theorem.

$$ml^2\frac{\mathrm{d}^2\theta}{\mathrm{d}t^2} = -mgl\sin\theta + \beta\frac{\mathrm{d}\theta}{\mathrm{d}t} \quad \text{the initial conditions are} \quad \theta\,|_{t=0} = \theta_0, \frac{\mathrm{d}\theta}{\mathrm{d}t}|_{t=0} = \dot{\theta}_0 \qquad (4.1)$$

This equation represents the roll DOF motion measured by a 6-axes motion sensor. When the amplitude is the small angle and less than 10°, it can be linearized into θ by **Taylor** expansion of $\sin\theta$, so the equation of motion can be simplified to

$$\frac{\mathrm{d}^2\theta}{\mathrm{d}t^2} + 2n\frac{\mathrm{d}\theta}{\mathrm{d}t} + k^2\theta = 0 \qquad n = \frac{-\beta}{2ml^2},\ k = \sqrt{\frac{g}{l}} \qquad (4.2)$$

At the small damping situation $n < k$, the roots of the characteristic equation are two unequal complex numbers: $r = -n \pm i\omega(\omega = \sqrt{k^2 - n^2})$. The general solution is

$$\theta = e^{-nt}(C_1\cos\omega t + C_2\sin\omega t) = Ae^{-nt}\sin(\omega t + \phi) \qquad (4.3)$$

A special solution according to the initial conditions is

$$A = \sqrt{\theta_0^2 + \frac{(\dot{\theta}_0 + n\theta_0)^2}{k^2 - n^2}} \quad \tan\phi = -\frac{\theta_0\sqrt{k^2 - n^2}}{\dot{\theta}_0 + n\theta_0} \qquad (4.4)$$

and the angular velocity is

$$\dot{\theta} = -nAe^{-nt}\sin(\omega t + \phi) + \omega Ae^{-nt}\cos(\omega t + \phi) = Ae^{-nt}\sin(\omega t + \phi + \varphi)\ \tan\varphi = -\frac{\omega}{n} \qquad (4.5)$$

The damping ratio is $\xi = \frac{n}{k}$, the circular frequency and period of the attenuated vibration are $\omega = k\sqrt{1 - \xi^2}$, k is the natural frequency of a non-damped free vibration system. At the same mass and length of the pendulum, the period of attenuated vibration is longer than the period of non-damped free vibration. In the case where the damping ratio ξ is less than 1, the larger the damping ratio, the longer the period becomes. At a certain moment t_i, the amplitude is Ae^{-nt_i}, and the next amplitude after one period is $Ae^{-n(t_i+T)}$, and the ratio of

the two amplitudes is $\eta = e^{nT}$, η is amplitude reduction rate. The ratio of two adjacent amplitudes is a constant, so the amplitude of the attenuated vibration decreases geometrically and quickly approaches zero.

By the way, if the resistance cannot be considered, the non-damped free vibration motion equation will be non-linear equation:

$$ml^2 \frac{d^2\theta}{dt^2} = -mgl\sin\theta,\ \theta\,|_{t=0} = \alpha(0 \le \alpha \le \pi), \frac{d\theta}{dt}\,|_{t=0} = 0 \qquad (4.6)$$

This is also the equation for the elastic curve and the meniscus of the liquid contained between the two parallel planes. The elliptic integral $K(m)$ is needed to get the rigorous solution of this non-linear equation, that is $\theta = 2\arcsin(\sin\varphi \sin\frac{\alpha}{2})$, $\sin\varphi = \frac{\sin\frac{\theta}{2}}{\sin\frac{\alpha}{2}}$, $\frac{d\theta}{d\varphi} == \frac{2\cos\varphi \sin\frac{\alpha}{2}}{\sqrt{1-\sin^2\frac{\alpha}{2}\sin^2\varphi}}$, $T = 4\sqrt{\frac{l}{g}}K(\sin^2\frac{\alpha}{2})$, $K(m) = F(\frac{\pi}{2}, m) = \int_0^{\frac{\pi}{2}} \frac{1}{\sqrt{1-m\sin^2\theta}} d\theta$. The rigorous solution can also be represented by the **Jacobi** elliptic function.

4.1.2 The Experimental Results

As shown on the left side of Fig. 4.1, the tube is wrapped around the disk in multiple circles, and the water flow speed inside the tube is controlled by the **Masterflex® L/S®** pump machine as shown on the middle side of Fig. 4.1. It is difficult to turn the water into a uniform flow but trying to make it flow at three different kinds of angular velocity about 0.369 rad/s, 0.737 rad/s and 1.106 rad/s. At the beginning of experiment, giving the initial condition of the tilt angle θ equal with 10° , **ZMP IMU-Z** 6-axis motion sensor equipped with 3-axis accelerometer and 3-axis gyro sensor is used for measuring vibration signal, "**IMU-Z** cube viewer" software as shown on the right side of Fig. 4.1 is used for data collection. This experiment belongs to the known mathematical equation of motion, using the collected experimental data to estimate and identify its parameters.

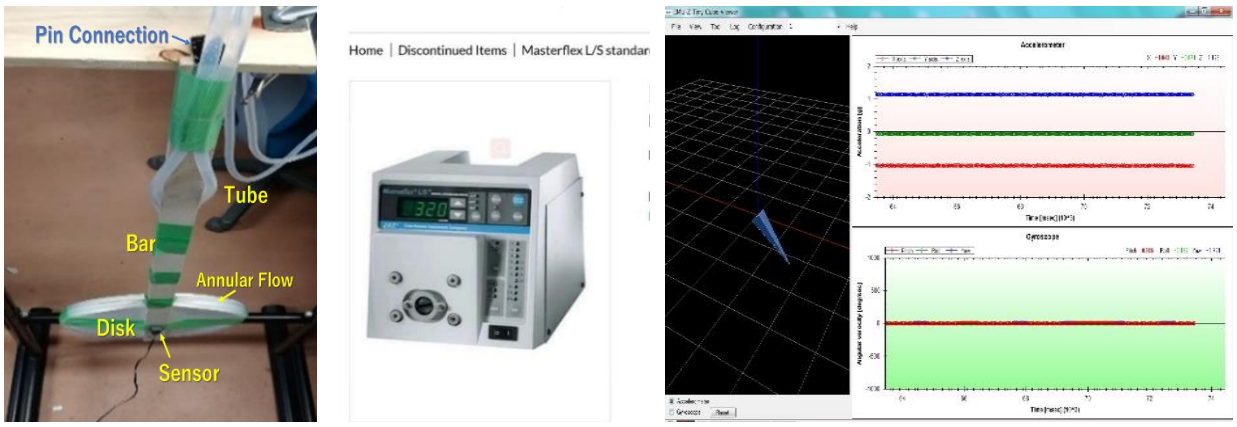

Fig. 4.1 Experimental model, pump and signal collection software

Due to the operation of the machine and other reasons, the obtained vibration curves show many burrs and are not smooth, its analysis shows that these interference noises belong to stationary random vibration signals. This article uses frequency domain method and time domain method to improve the signal-to-noise ratio of the vibration signal.

In 1965, a fast algorithm for discrete **Fourier** transform was first published. For free decay function, the longer the data length, the closer the signal amplitude will eventually become to zero, whether the truncation is at the periodic node will be not very important, therefore FFT as a simple method and fast calculation speed is suitable analysis method for free decay signal. This paper uses high pass filter, cut-off frequency from 2 Hz to 50 Hz. The modal parameter identification is all carried out by complex exponential method.

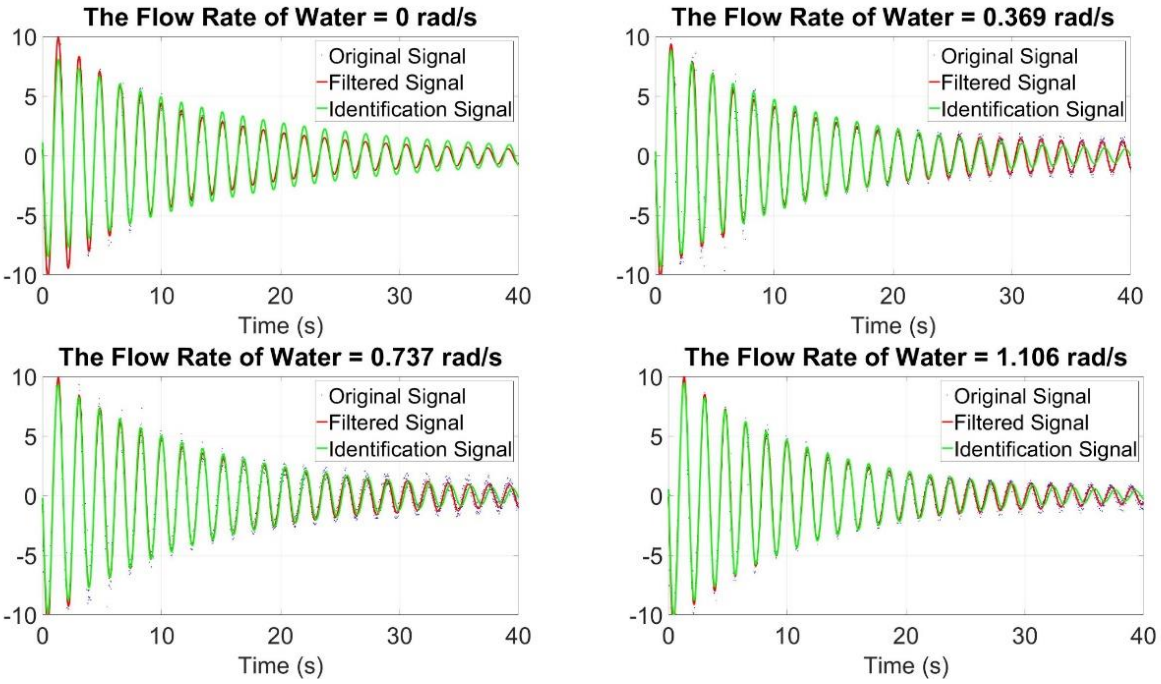

Fig. 4.2 Signal data based on FFT

The time domain method directly uses the free vibration response signal for parameter identification, because it does not need to perform **Fourier** transform processing, it will not cause leakage due to signal truncation. The cross-correlation function can be obtained by measuring the response signal at multiple points to reduce the noise. This article uses multi-point averaging and smoothing to eliminate high-frequency noise in the response signal of a single measuring point.

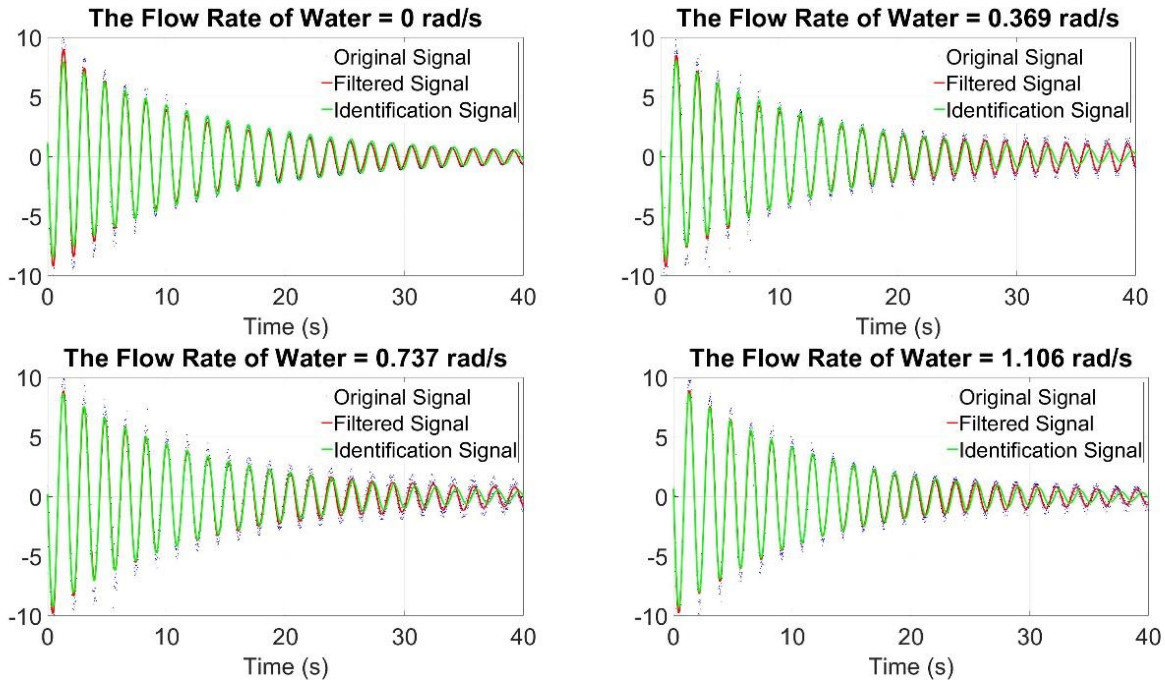

Fig. 4.3 Signal data based on time domain method

Tab. 4.1 Comparison of the experimental results

No.	Initial Angle [°]	ω_{water} [rad/s]	Experimental Result from Frequency Domain Method		Experimental Result from Time Domain Method	
			Frequency [Hz]	Damping Ratio	Frequency [Hz]	Damping Ratio
1	10	0	0.5806	1.5674	0.5787	1.9220
2	10	0.369	0.5753	1.9642	0.5739	2.0817
3	10	0.737	0.5761	1.9592	0.5751	2.1223
4	10	1.106	0.5788	2.1574	0.5771	2.3373

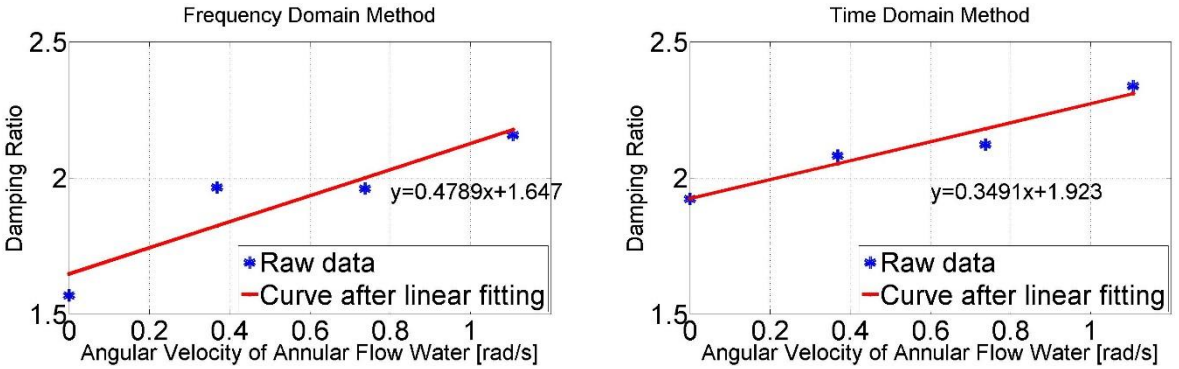

Fig. 4.4 Comparison of the experimental results after linear fitting

When the water inside the tube as a torus structure participates in the pendulum movement of the disc, the damping coefficient increases as the angular velocity of the water increases.

However, because the flow water in the silicone tube is not uniform, and the pump interference vibration signal, the damping coefficient increases with a certain error. After the frequency domain and the time domain noise signal removal and the complex exponential parameter identification method, although the damping coefficient obtained by the time domain noise removal method are significantly larger than the frequency domain noise removal method, the damping coefficient increases linearly very well as the angular velocity of the annular flow water increases, the axial retention effect, which acts on the damping effect of the simple pendulum can be confirmed. Consequently, the validity of the motion equation of the torus structure with the annular flow shown in Equation 3.75 is confirmed.

4.2 The Preliminary Design of FOWT above the Water-plane

First of all, to determine the FOWT part above the water-plane, the design of this part take economy as the main consideration and take into account the effect of reducing wind load. Using the blade element momentum (BEM) theory to calculate the energy absorbed by the blades and the wind load acting on blades. The wind load of the support column from the nacelle to the water-plane can be calculated by empirical formula:

$$dF = \frac{1}{2}\rho_{air} C_d v_n^2 ds \tag{4.7}$$

where, ds is dividing the tower into several facets, drag coefficient C_d will depend on building shape. After determining the FOWT part in the air, to design the supporting part of the floating body in the water at last. According to the **Archimedes** principle:

$$m_{above} + \rho_{Material} V_{Material} + m_{ballast} = \rho_{water} V_{drained} \tag{4.8}$$

where, m_{above} is the mass of the FOWT part above the water-plane, it is decided in the first step of design, which has an impact on the overall GM value and moment of inertia of the FOWT; $m_{ballast}$ is the mass of ballast, it is an adjustable part to keep GM value in the right range, generally steel, soil, and seawater are used to lower the center of gravity; there is a coupling relationship between $\rho_{Material} V_{Material}$ and $\rho_{water} V_{drained}$, it is determined to consider various factors not just hydrodynamic parameters. The position of the center of gravity and the shape of the floating body are the decisive factors for the hydrodynamic parameters.

The capacity factor of onshore wind farms will be 30%, and for offshore wind turbines, 40% or more is desirable. In order to achieve such high capacity factor, it needs an annual average wind speed about 7.5 m/s or more. Although these capacity factors cannot be compared with nuclear power that can be 80%. At present, the research on the power generation efficiency of horizontal-axis wind turbines is basically based on BEM theory, which is based on fluid

mechanics to calculate the wind energy that horizontal-axis wind turbines can absorb from the flowing air and wind load acting on the blades. This article just used the previous part - energy absorbed, so the previous part was only introduced and calculated.

4.2.1 The Absorbed Energy

Blade can be assumed as two-dimensional airfoil along the blade chord and is composed of various units along the blade span. The flowing air is seen as ideal incompressible fluid so as to the **Bernoulli** equation can be applied to aerodynamic analysis of blade.

$$p + \frac{1}{2}\rho v^2 + \rho g h = \text{const} \tag{4.9}$$

The pressure relation between before the blade plate and behind the blade plate can be got.

$$p_d^+ - p_d^- = \frac{1}{2}\rho(v_\infty^2 - v_w^2) \tag{4.10}$$

p_d^+ is the pressure before the blade plate, p_d^- is the pressure behind the blade plate, v_∞ is wind velocity in the upwind side, v_w is wind velocity in the leeward side. The direction that blade rotates is tangential direction and the direction parallel to the wind direction is the axial direction.

The amount of momentum change is equal to the product of the mass flow rate and the rate of velocity change. The force that causes the momentum to change is entirely from the pressure difference between the front and the back of the blade plane. We can get,

$$(v_\infty - v_w)\rho A_d v_d = (p_d^+ - p_d^-)A_d \tag{4.11}$$

v_d is axial induced velocity in the blade plate. Then,

$$v_d = v_\infty(1-a),\ v_w = v_\infty(1-2a) \tag{4.12}$$

a is the defined axial inducer. It means that the velocity loss radio before the blade plate is a and the velocity loss radio behind the blade plate is also a in the axial direction.

So, the energy power absorbed by the blade plane from the airflow is

$$P_{abs} = Fv_d = (v_\infty - v_w)\rho A_d v_d v_d = 2\rho A_d v_\infty^3 a(1-a)^2 \tag{4.13}$$

The wind energy utilization factor is

$$C_p = \frac{2\rho A_d v_\infty^3 a(1-a)^2}{\frac{1}{2}\rho A_d v_\infty^3} = 4a(1-a)^2 \tag{4.14}$$

So $dC_p/da = 12a^2 - 16a + 4$, when $a = 1/3$, the wind energy utilization factor C_p will get the max value 59.26%. It is also called Betz limit. At this time, the energy power absorbed by the blade plane from the airflow is

$$P_{max} = \frac{1}{2}\rho A_d v_\infty^3 \tag{4.15}$$

P_{max} is the max absorbed energy power to electrical energy power [kg·m^2/s^3], ρ is the air density [kg/m^3], A_d is the sweeping area when the blades rotate [m^2], v_∞ is the wind velocity in the upwind side [m/s]. Based on dimensional analysis, this formula is also correct.

4.2.2 The Wind Turbine Blade Design Considering Local Wind Data

Three kinds of rated wind speeds: 10 m/s, 12 m/s and 15 m/s and seven kinds of rated output power of wind turbines: 3 MW, 5 MW, 10 MW, 15 MW, 20 MW, 25 MW and 30 MW are assumed. The relationship between wind speed and power generation is shown in Equation 4.15. Here give power curves of three kinds of rated wind speeds and two kinds of rated output power.

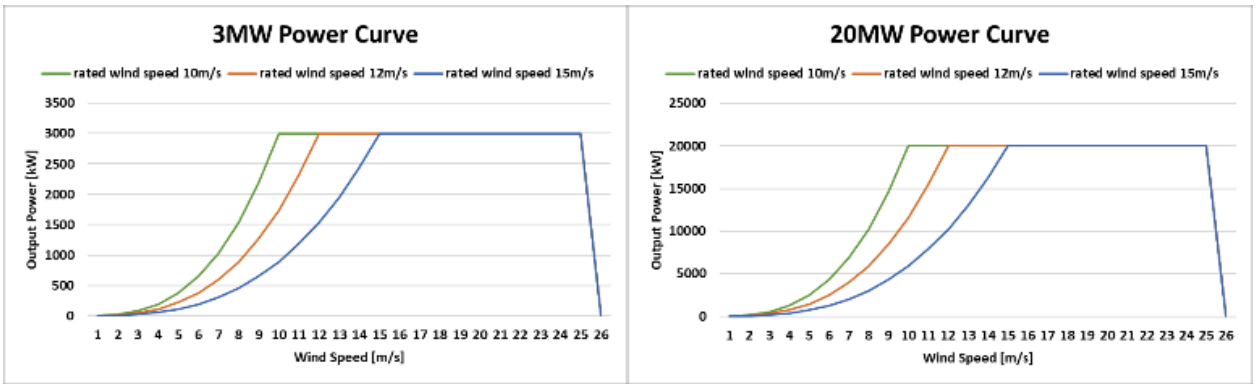

Fig. 4.5 Power curves at different rated wind speeds and different rated output powers

This article does not consider the impact of FOWT's shaking motion on power generation, and assumes that the FOWT has been kept upright. Meanwhile, the length of blade will be different at the case of different rated wind speeds and different rated output powers. The length of blade is as shown in the figure below.

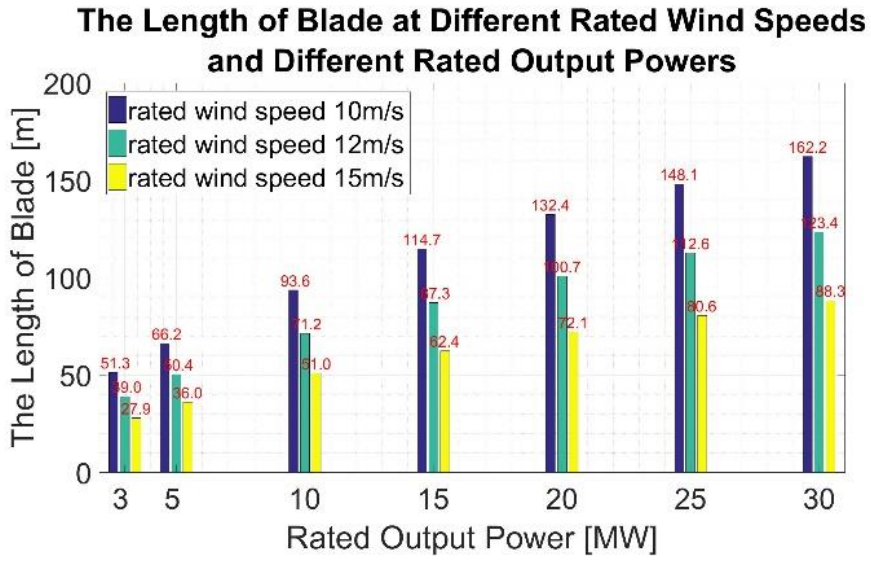

Fig. 4.6 Length of blade at different rated wind speeds and different rated output powers

Because of this, the height of a windmill varies with the rated wind speeds and rated output powers. The wind speed at different heights at the same location is different, and it has the following relationship:

$$v(z) = v(z_0)\left(\frac{z}{z_0}\right)^{\alpha} \tag{4.16}$$

Generally, the recording instrument for meteorological observation data is set at a height of about 10 m, so z_0 generally takes 10m, α is the ground roughness coefficient. The change of wind speed with height is mainly caused by the friction between the fluid and the ground. The higher the height, this effect tends to disappear. Because the surface of the ocean is smooth and flat, the wind speed that is not affected by the surface of the ocean is lower than that on land. Offshore sea surface and coast generally take a value of 0.12 for α.

Once we can transform into electricity generation based on the wind speed value, then knowing all the wind speed values of a certain place for a year, the annual power generation can be calculated as shown in Equation 4.16.

$$E = \int f(v)P(v)dv \tag{4.17}$$

Once the annual power generation is got, capacity factor can be calculated by Equation 4.18.

$$\eta = \frac{E_{(\mathrm{kWh})}}{P(\mathrm{kW})\times 8760(\mathrm{h})} \tag{4.18}$$

From the Japan Oceanographic Data Center (JODC) [56], meteorological data over the years can be download for free, which observed by the meteorological observation devices such as lighthouse, maritime traffic center, ship direction signal station, ship traffic signal station, radio direction signal station and radar built by the Japan Maritime Security Agency along the coast of Japan. The meteorological data has two observation time intervals: hourly and every half-hour. There are 8760 pieces of data per year at an hourly interval, and 17520 pieces of data are doubled every half-hour. For wind observation data, there are two parameters: wind direction and wind speed. The observation data of wind direction and wind speed is the average value from 10 minutes before the observation time to the observation time. Next, based on the wind speed data of "舳倉島" in 2000, capacity factor at three kinds of rated wind speeds and seven kinds of rated output power of wind turbines is calculated.

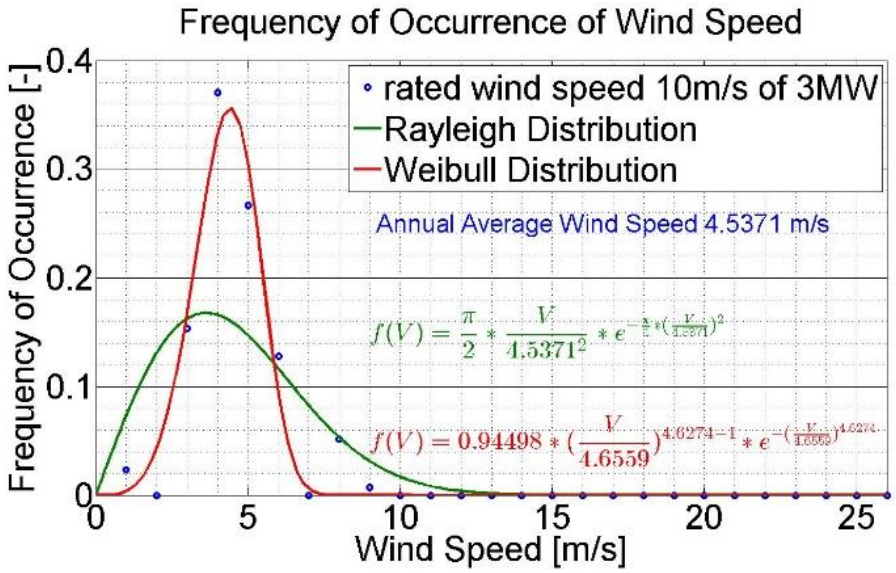

Fig. 4.7 The wind speed information of "舳倉島" in 2000

Although the **Rayleigh** distribution fits very well when the frequency of occurrence of wind speed data value is small, it's consistent with **Weibull** distribution very well when looking at the all data. The scale parameter λ is 4.6559 and the shape parameter k is 4.6274, this shows that these data conform to the theoretical model and are correct.

The probability density function of **Weibull** distribution is:

$$f\left(x;\lambda,k\right)=\begin{cases}\frac{k}{\lambda}\left(\frac{x}{\lambda}\right)^{k-1}e^{-\left(x/\lambda\right)^{k}} & x\geq 0\\ 0 & x<0\end{cases} \tag{4.19}$$

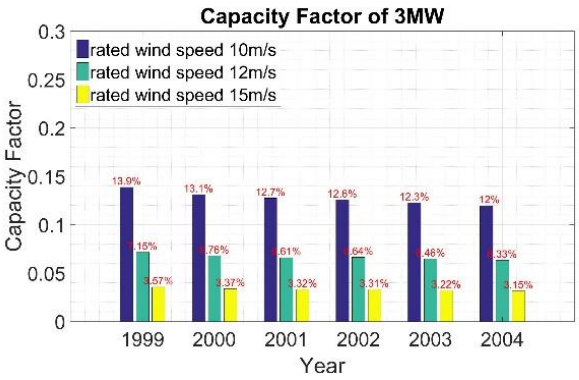

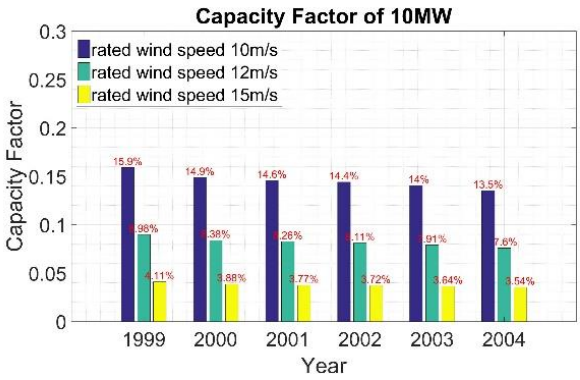

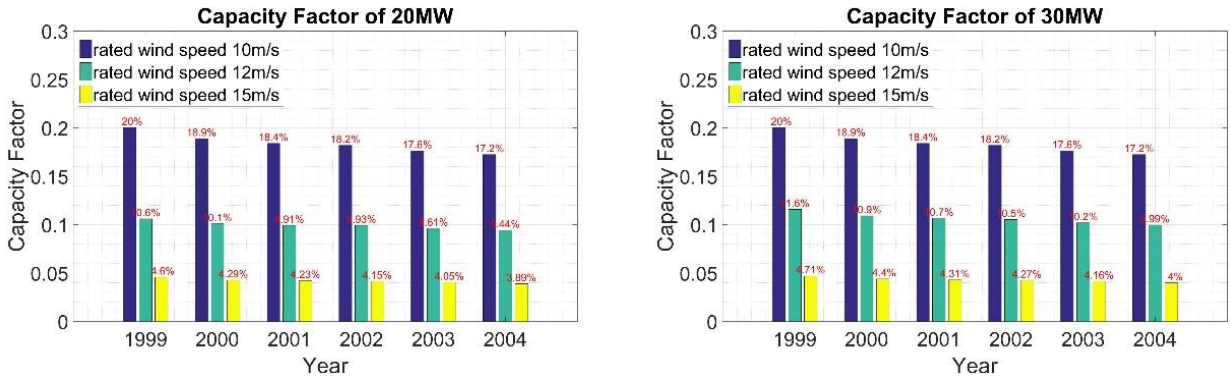

Fig. 4.8 Capacity factor at different rated wind speeds and different rated output powers

For three kinds of rated wind speeds, rated wind speed is bigger, the capacity factor value is smaller, and when rated wind speed is 10 m/s, the capacity factor is the maximum, but it is a small value and almost around 13% ~ 20%, this is because the annual average wind speed of "舳倉島" is not strong enough. For seven kinds of rated output power of wind turbines, rated output power is bigger, the capacity factor value is bigger, and when rated output power is 20 MW and more, the capacity factor will be almost the same, this means that the rated output power of wind turbines is not bigger, the capacity factor value is bigger, there is a limit value and 20 MW seems to be the limit value. In addition, the capacity factor for the six years has remained unchanged, but has a decreasing trend.

In actual production, the capacity factor as the design goal, the rated wind speed, rated output power and size parameters of the wind turbine are determined based on the local meteorological data. This paper selects 20 MW as the research object, and here give the data of the wind turbine blades and tower section above the water-plane.

Tab. 4.2 Parameters above the water-plane

Item	Unit [m]	Item	Unit [m]
Blade Length	100	Nacelle (Hollow but Thick Wall) Length	30
Blade Width	1	Nacelle Width	10
Blade Wall Thickness	0.2	Nacelle Height	8
Support Hollow Cylinder Radius	5	Nacelle Wall Thickness	0.8 and 0.2
Support Hollow Cylinder Length	110		
Support Hollow Cylinder Wall Thickness	0.3 and 0.01		

4.3 The Parametric Study of FOWT under the Water-plane

This paper takes the input parameters of the hydrodynamic analysis model as design

variables for comparative research. The design variables include the presence or absence of the torus structure and different positions placed in the vertical direction; the radius of the torus structure, the radius of the internal annular flow and the angular velocity of the annular flow; the cylindrical radius and draft of the central floating body, and the wall thickness. Two types of FOWT are designed, one is cylinder-type FOWT, and the other is SPAR-type FOWT with wave-free shape. The cylinder-type FOWT has the same blade and nacelle structure as the SPAR-type FOWT. It is also assumed that this torus portion is horizontally and rigidly attached to the central cylinder portion via four rigid beams. Meanwhile, all FOWTs are floating in the ocean with a water depth of 200m, the regular wave was propagated in the direction of pitch when performing simulation calculation.

4.3.1 The Cylinder-type FOWT

In response to this contradiction problem that the torus structure is embedded at different heights, the hydrodynamic responses are respectively discussed based on potential theory.

The first kind of FOWT with cylinder-shaped buoyancy providing part is discussed as shown in Fig. 4.9 and Tab. 4.3. Because of the spatial asymmetry of FOWT, the moments of inertia of blade and nacelle around the two vertical axes of horizontal plane are different, what's more, with the rotation of the blade, the moment of inertia of the z-axis perpendicular to the water surface and the y-axis perpendicular to the blade will alter periodically over time, but the moment of inertia of the x-axis parallel to the blade will not alter with time. The influence of the change of moment of inertia on the hydrodynamic response of FOWT has been analyzed. Because the blade is made of light-weight material, the moment of inertia of blades occupy a relatively small proportion of the whole FOWT, although the blades rotate motion is the spinning top motion, the impact on hydrodynamics is very small. In this paper, the moment of inertia of the blade attitude as shown in Fig. 4.8 was adopted.

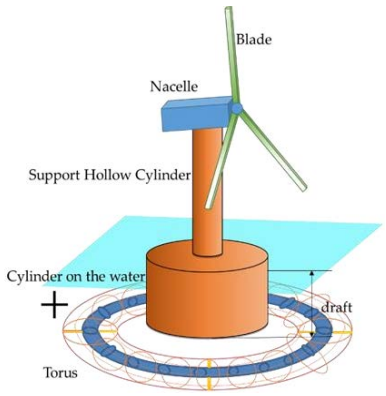

Fig. 4.9 Designed cylinder-type FOWT

Tab. 4.3 Parameters of cylinder-type FOWT

Item	Unit [m]	Unit [m]
Cylinder Radius	30	30
Cylinder Height	45	35
Cylinder Wall Thickness	0.15	0.05
Steel Ballast Height	12	12
Support Hollow Cylinder Radius	5	5
Support Hollow Cylinder Length	110	110
Support Hollow Cylinder Wall Thickness	0.3	0.01

For the comparative research on the design variable of the wall thickness, the height of the supporting part of the column in the water has been reduced from 45 m to 35 m, and the cylinder wall thickness has been reduced from 0.15 m to 0.05 m; the support hollow cylinder wall thickness has been reduced from 0.3 m to 0.01 m; the nacelle wall thickness has been reduced from 0.8 m to 0.2 m. The heavy cylinder-type FOWT and the light Cylinder-type FOWT are called.

By comparing with or without torus structure and the position of torus in the vertical direction, observe its influence on hydrodynamic performance. Putting the torus structure at the bottom is to place the lowest point of the torus and the lowest point-K point of the cylinder-type FOWT at the same water depth. Placing the torus structure in the middle is to place the center point of the torus structure in the vertical direction at half the draft of the cylinder-type FOWT. Setting the torus structure on the top is to place the center point of the torus structure in the vertical direction at a height of 10 m from the water-plane. When calculating the moments of inertia of blade and nacelle, some simplifications were employed in the structure compared with the actually running FOWT.

4.3.1.1 Change the Heights of the Torus Structure

In this Section, the presence or absence of the torus structure and the different positions placed in the vertical direction, these two variables are design parameters.

1. The heavy cylinder-type FOWT

Tab. 4.4 Parameters of model without torus, M40-3 and M40-7

Item	without Torus	M40-3 bottom	M40-3 middle	M40-3 top	M40-7 bottom	M40-7 middle	M40-7 top
Distance from Center of Tube to Torus [m]	0	40	40	40	40	40	40
Radius of Tube of External Torus [m]	0	3.724	3.724	3.724	7.718	7.718	7.718
Radius of Tube of Internal Torus [m]	**0**	**3**	**3**	**3**	**7**	**7**	**7**
KB [m]	21.76	20.26	21.73	22.67	17.82	21.65	24.84
KG [m]	24.51	22.79	24.25	25.20	19.81	23.63	26.82
GM [m]	2.51	2.30			1.80		
Draft [m]	42.75						
Displacement [m^3]	120884	131838			167919		
Total Mass[t]	123906	135134			172117		
Moment of Inertia Jz [$t \cdot m^2 \times 10^4$]	5279	6822			10717		
Moment of Inertia Jx [$t \cdot m^2 \times 10^4$]	28830	31034	29838	29437	37010	33295	31574
Moment of Inertia Jy [$t \cdot m^2 \times 10^4$]	28902	31107	29910	29508	37082	33367	31646
Proportion of Moment of Inertia of water Jz [%]	0	14.20			41.04		

Proportion of Moment of Inertia of water Jx [%]	0	5.02	2.71	1.89	19.04	12.11	8.35
Proportion of Moment of Inertia of water Jy [%]	0	5.01	2.70	1.89	19.00	12.09	8.33

After the neutral torus structure with the same buoyancy and gravity is externally embedded similar to the different heights of FOWT as the wave-free structure, the center of gravity and the center of buoyancy of the floating body will change, especially the moment of inertia around the horizontal axis changes greatly.

1) M40-3

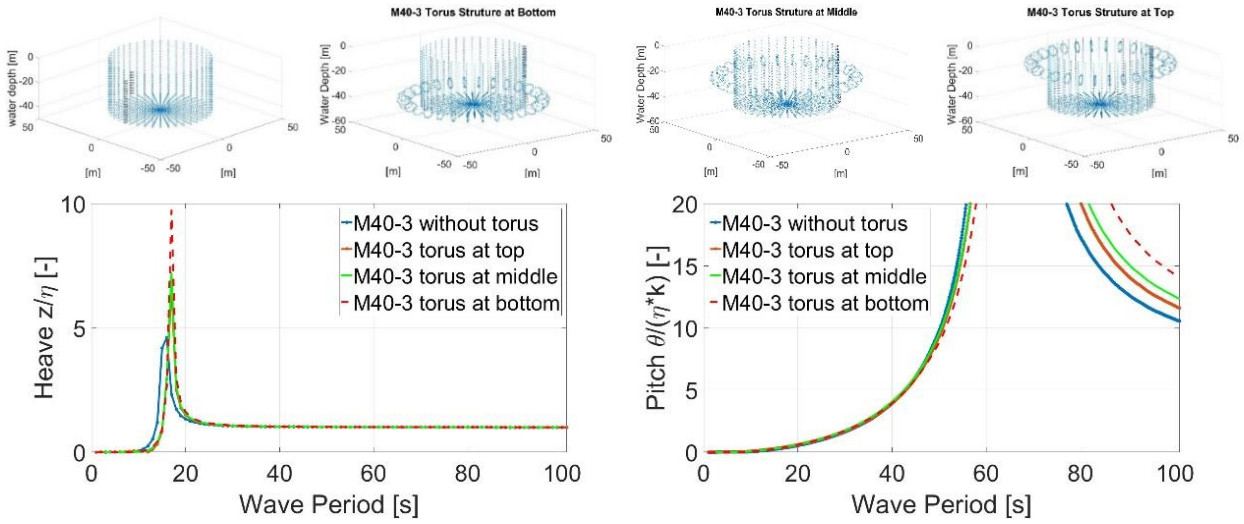

Fig. 4.10 Wet surface mesh and RAO of heave and pitch DOFs of M40-3

The blue curve drawn by the data from the motion6.dat file is the calculation result of the existing program in the laboratory, and the red curve is calculated by MATLAB based on the hydrodynamic parameters in the calculation result of the existing program.

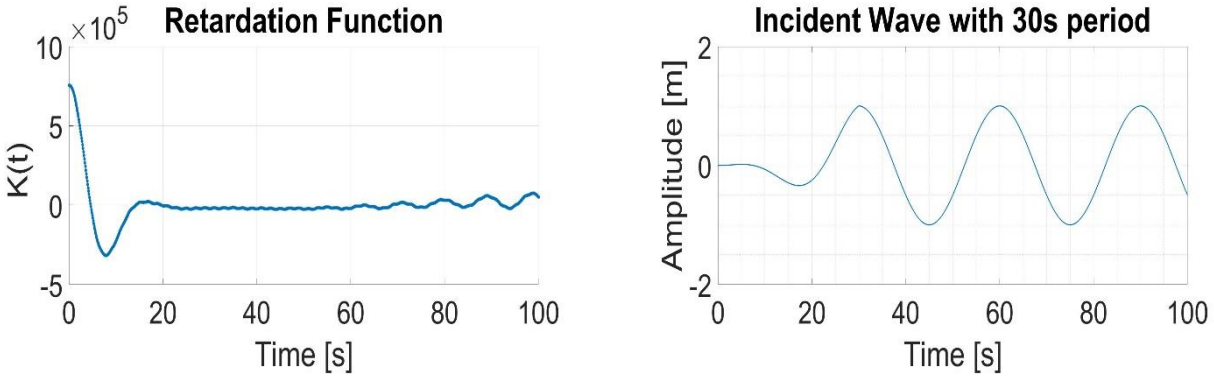

Fig. 4.11 The retardation function and the incident wave with 30s period

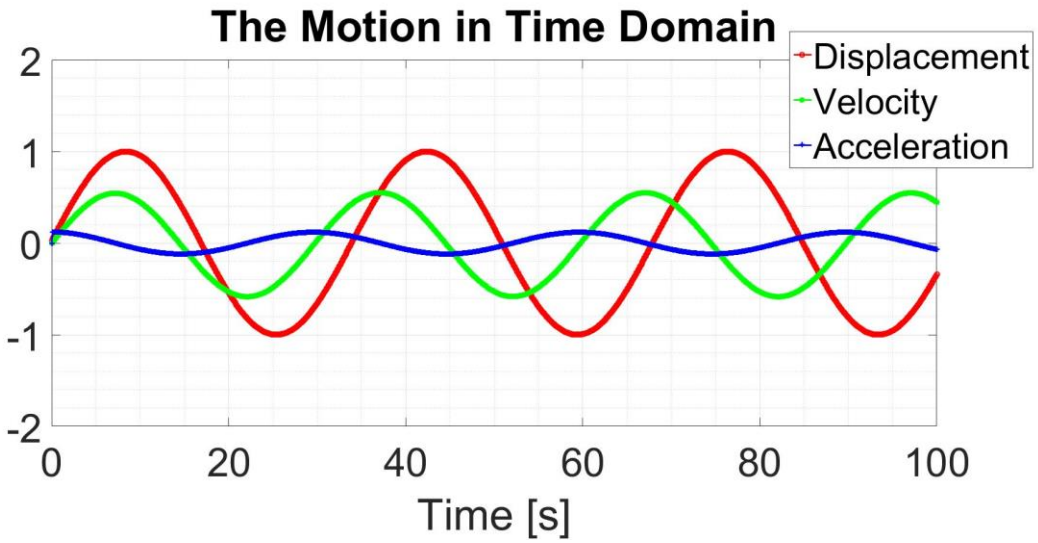

Fig. 4.12 The displacement, velocity, acceleration in time domain

When the incident wave period is 30s, the amplitude response value in the frequency domain and in time domain is the same. This comparison illustrates the high accuracy of the program used.

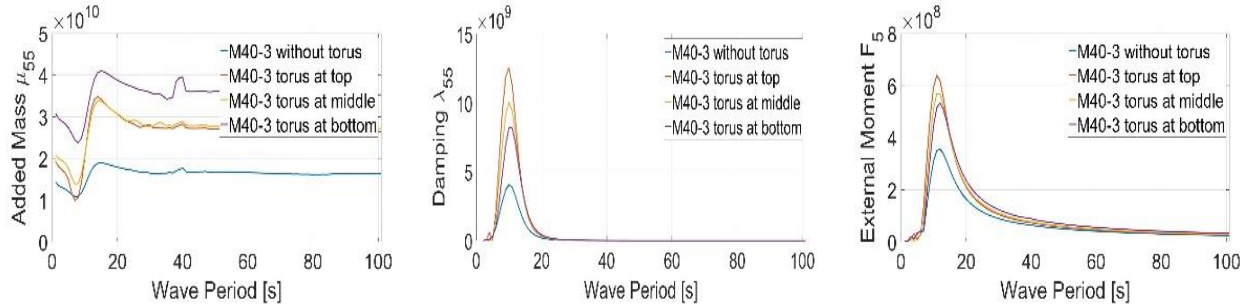

Fig. 4.13 The hydrodynamic parameters of M40-3

In terms of heave DOF, the torus structure of different heights will mainly cause a slight change in the added mass in the hydrodynamic parameters. The lower the vertical height of the torus structure, the greater the added mass, while the damping coefficient and external wave force hardly change. In the pitch DOF, the torus structure of different heights will also mainly cause the change of the added mass in the hydrodynamic parameters, but the magnitude of the change will be relatively large, and the trend of change is also that the torus structure goes down in the vertical height, the more the added mass is large, and the damping coefficient will hardly change, but the external wave force will change slightly.

2) M40-7

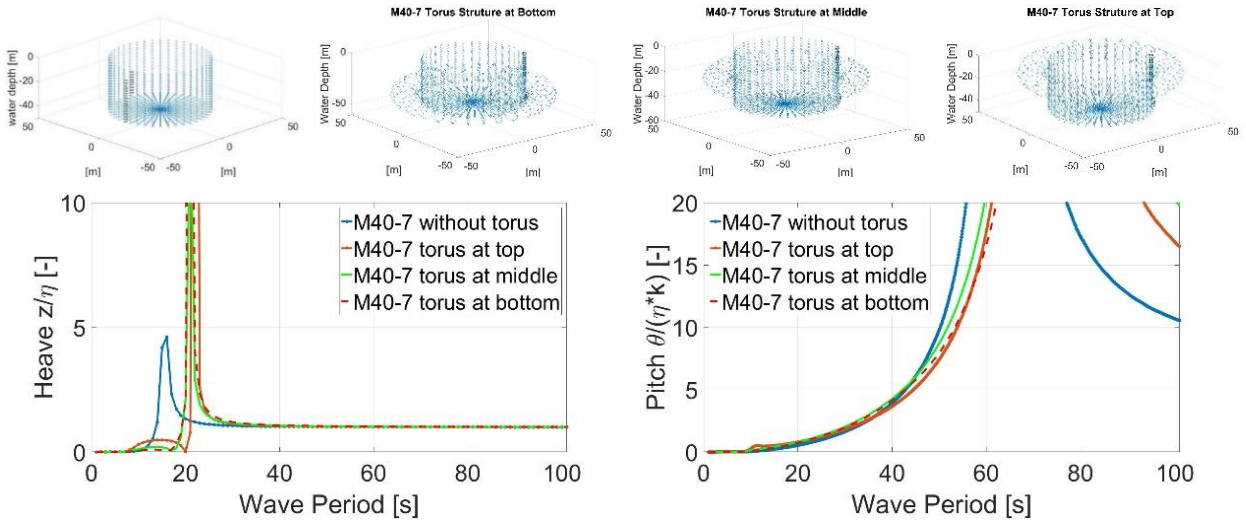

Fig. 4.14 Wet surface mesh and RAO of heave and pitch DOFs of M40-7

As can be seen from the RAO diagram of M40-3 and M40-7, when FOWT with a torus structure, a bigger natural period can be obtained than without torus structure, this is because the former has larger the mass coefficient and added mass coefficient, but the resilience coefficient does not change. According to common sense, the torus structure at top can withstand more intense wave, this is beneficial to the overall hydrodynamic response and is what we hope, but it will increase the overall center of gravity and buoyancy and reduce the moment of inertia around the horizontal axis, which will be harmful to the overall hydrodynamic response and is not what we want. However, the torus structure at top has not a better hydrodynamic response than the torus structure at middle, it looks like the advantage and disadvantages are almost neutralized and offset. When the torus structure at bottom has the best hydrodynamic, it looks like the advantages of lowering the overall center of gravity and buoyancy has a slightly greater impact than the disadvantage.

2. The light cylinder-type FOWT

Tab. 4.5 Parameters of model without torus, M40-3 and M40-7 after weight reduction

Item	without Torus	M40-3 bottom	M40-3 middle	M40-3 top	M40-7 botto m	M40-7 middle	M40-7 top
Distance from Center of Tube to Torus [m]	0	40	40	40	40	40	40
Radius of Tube of External Torus [m]	0	3.724	3.724	3.724	7.718	7.718	7.718
Radius of Tube of Internal Torus [m]	**0**	**3**	**3**	**3**	**7**	**7**	**7**
KB [m]	17.02	15.63	16.97	17.66	13.91	16.87	19.07
KG [m]	9.95	9.30	10.65	11.33	9.21	12.16	14.36
GM [m]	13.85	12.40			9.22		
Draft [m]	33.15						
Displacement [m³]	93724	104678			140759		

Total Mass[t]	95987	107215			144198		
Moment of Inertia Jz [t·m²×10⁴]	4371	5914			9810		
Moment of Inertia Jx [t·m²×10⁴]	11510	12976	12313	12117	16890	15097	14254
Moment of Inertia Jy [t·m²×10⁴]	11545	13011	12348	12152	16925	15131	14289
Proportion of Moment of Inertia of water Jz [%]	0	16.38			44.84		
Proportion of Moment of Inertia of water Jx [%]	0	8.44	5.52	4.59	28.27	21.99	18.50
Proportion of Moment of Inertia of water Jy [%]	0	8.42	5.50	4.58	28.21	21.94	18.46

1) M40-3

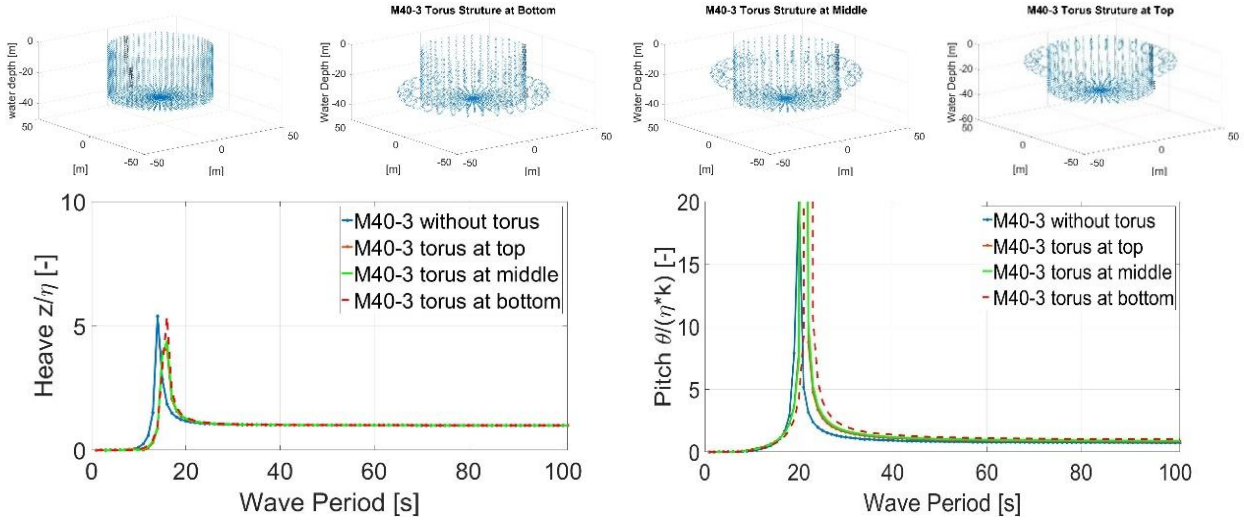

Fig. 4.15 Wet surface mesh and RAO of heave and pitch DOFs of M40-3 after weight reduction

2) M40-7

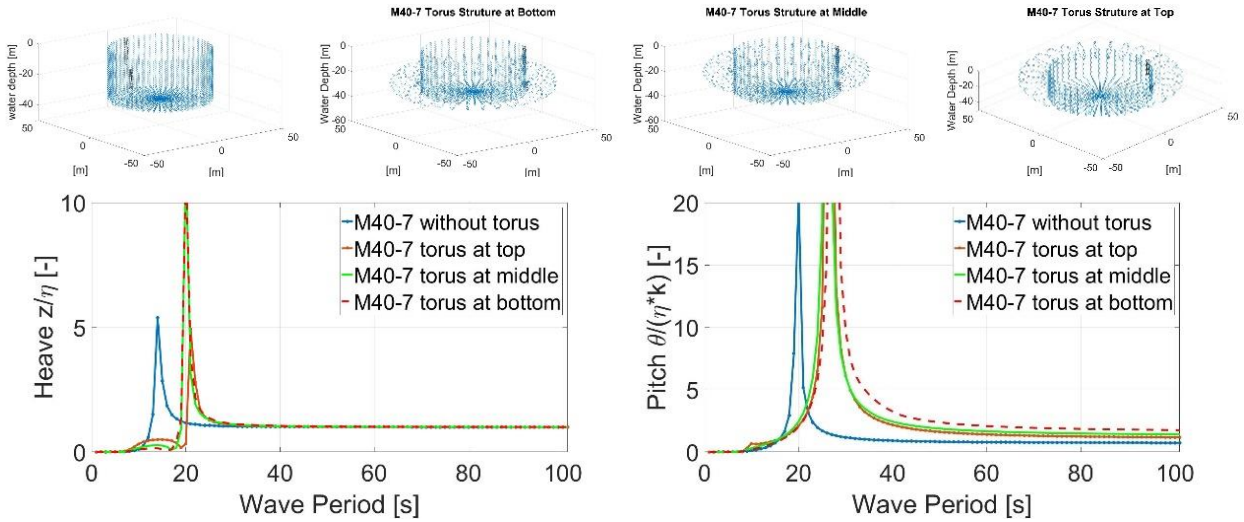

Fig. 4.16 Wet surface mesh and RAO of heave and pitch DOFs of M40-7 after weight reduction

As can be seen from the RAO diagram of M40-3 and M40-7 after weight reduction, the natural period of its heave DOF does not decrease much compared to before weight reduction, it is still around 20s, but the natural period of pitch DOF has been greatly reduced compared with that before weight reduction, it has only $\frac{1}{3}$ of the previous weight. Other conclusions are similar, it is also when FOWT with a torus structure, a bigger natural period can be obtained than without torus structure, the torus structure at top has not a better hydrodynamic response than the torus structure at middle, and when the torus structure at bottom has the best hydrodynamic.

4.3.1.2 Change the Torus Structure

In this Section, the radius of the torus structure, the radius of the internal annular flow and the angular velocity of the annular flow, these three variables are design parameters.

1. The heavy cylinder-type FOWT

Tab. 4.6 Cylinder-type FOWT parameters with the radius change of ring tube of internal torus

Item	M40-1	M40-2	M40-3	M40-4	M40-5	M40-6
Distance from Center of Tube to Center of Torus [m]	40					
Radius of Tube of External Torus [m]	1.74	2.7285	3.724	4.7214	5.72	6.7188
Radius of Tube of Internal Torus [m]	**1**	**2**	**3**	**4**	**5**	**6**
KB [m]	21.37	20.87	20.26	19.59	18.93	18.33
KG [m]	24.07	23.50	22.79	22.00	21.20	20.46
GM [m]	2.46	2.39	2.30	2.19	2.07	1.94
Draft [m]	42.75					
Displacement [m^3]	123280	126767	131838	138489	146719	156529
Total Mass [t]	126362	129936	135134	141951	150387	160443
Moment of Inertia Jz [$t \cdot m^2 \times 10^4$]	5651	6150	6822	7638	8573	9606
Moment of Inertia Jx [$t \cdot m^2 \times 10^4$]	29304	30026	31034	32281	33718	35307
Moment of Inertia Jy [$t \cdot m^2 \times 10^4$]	29376	30098	31107	32353	33790	35379
Proportion of Moment of Inertia of water Jz [%]	1.97	7.24	14.20	21.62	28.76	35.27
Proportion of Moment of Inertia of water Jx [%]	0.61	2.38	5.02	8.23	11.76	15.41
Proportion of Moment of Inertia of water Jy [%]	0.61	2.38	5.01	8.21	11.73	15.38

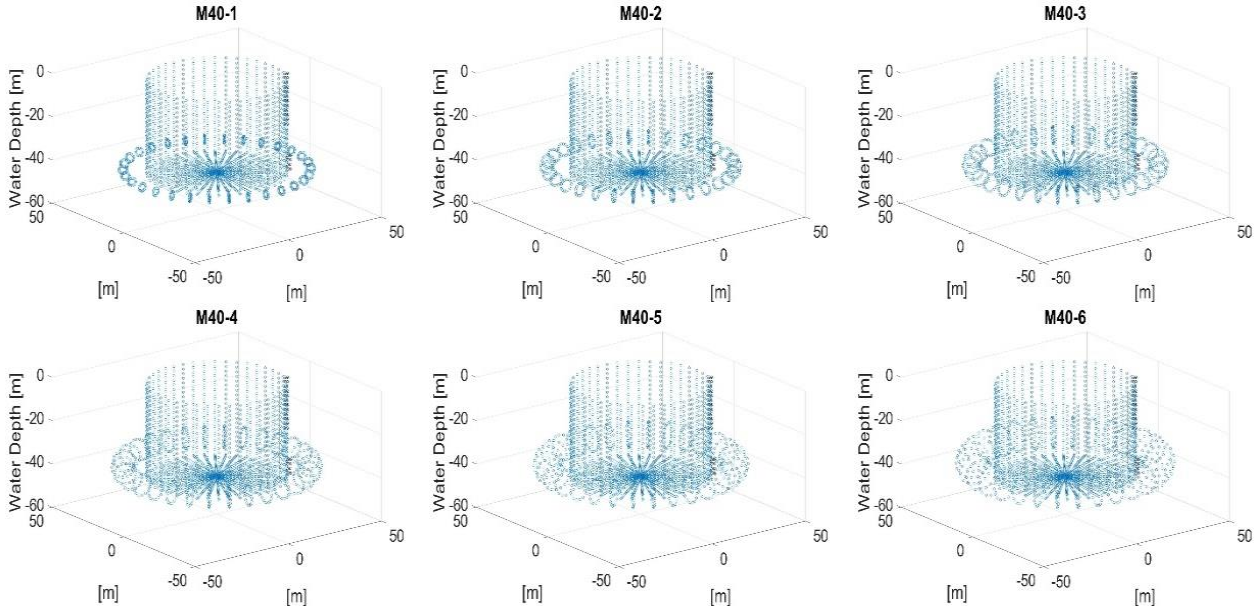

Fig. 4.17 Cylinder-type FOWT wet surface mesh with the radius change of ring tube of internal torus

Tab. 4.7 Cylinder-type FOWT parameters with distance from center of ring tube to center of torus change

Item	M35-3	M40-3	M45-3	M50-3	M55-3	M60-3
Distance from Center of Tube to Center of Torus [m]	**35**	**40**	**45**	**50**	**55**	**60**
Radius of Tube of External Torus [m]	3.719	3.724	3.7275	3.7303	3.7327	3.7346
Radius of Tube of Internal Torus [m]	3					
KB [m]	20.44	20.26	20.09	19.92	19.75	19.59
KG [m]	22.99	22.79	22.59	22.39	22.20	22.01
GM [m]	2.32	2.30	2.27	2.25	2.23	2.21
Draft [m]	42.75					
Displacement [m^3]	130441	131838	133234	134630	136027	137423
Total Mass [t]	133702	135134	136565	137996	139427	140859
Moment of Inertia Jz [$t \cdot m^2 \times 10^4$]	6288	6822	7517	8393	9473	10776
Moment of Inertia Jx [$t \cdot m^2 \times 10^4$]	30647	31034	31473	31969	32528	33159
Moment of Inertia Jy [$t \cdot m^2 \times 10^4$]	30719	31107	31545	32041	32601	33231
Proportion of Moment of Inertia of water Jz [%]	10.10	14.20	18.66	23.24	27.71	31.92
Proportion of Moment of Inertia of water Jx [%]	4.10	5.02	6.07	7.25	8.57	10.04
Proportion of Moment of Inertia of water Jy [%]	4.09	5.01	6.05	7.23	8.56	10.02

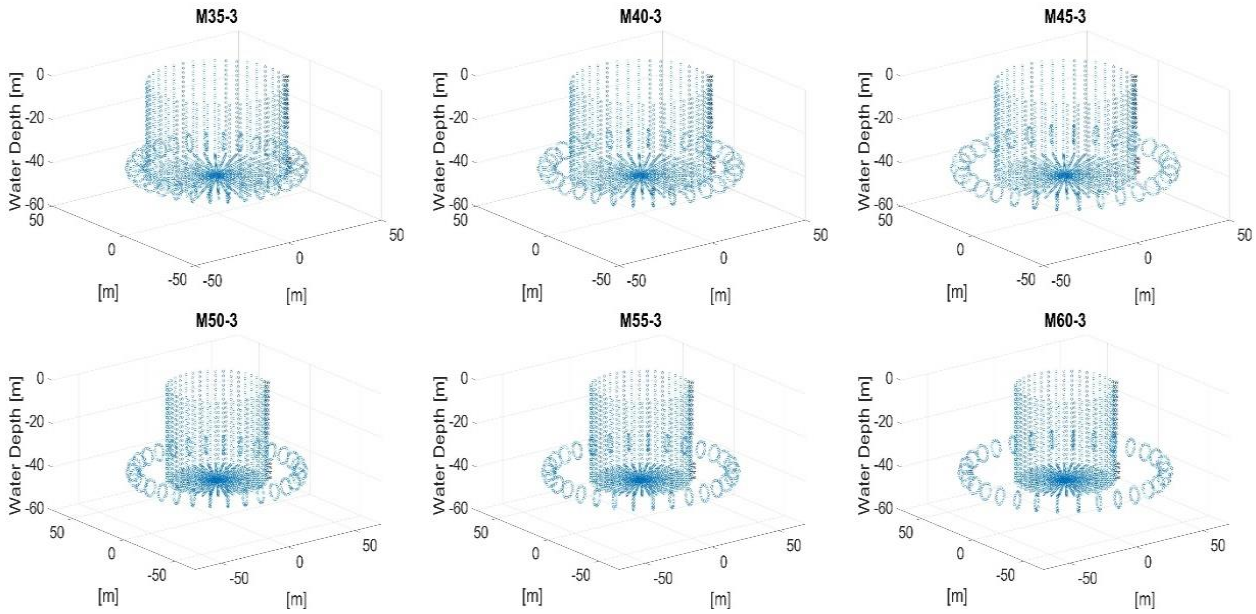

Fig. 4.18 Cylinder FOWT wet surface mesh with distance from center of ring tube to center of torus change

The contour diagram of hydrodynamic response RAO of pitch is shown in Fig. 4.19 and Fig. 4.20. The two coordinate axes of **Cartesian** plane represent the period of regular wave and the angular velocity of annular flow, and the contour lines are made dimensionless by means of the amplitude value of pitch divided by wave height, then divided by wave number.

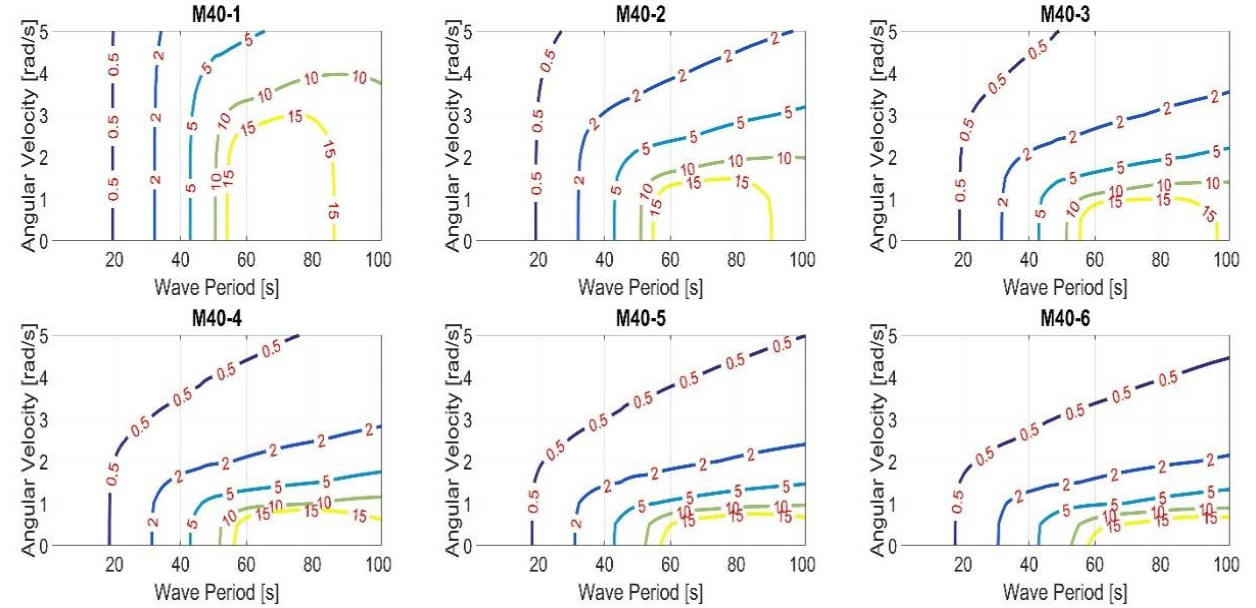

Fig. 4.19 Contour graph of cylinder FOWT pitch RAO with the radius change of ring tube of internal torus

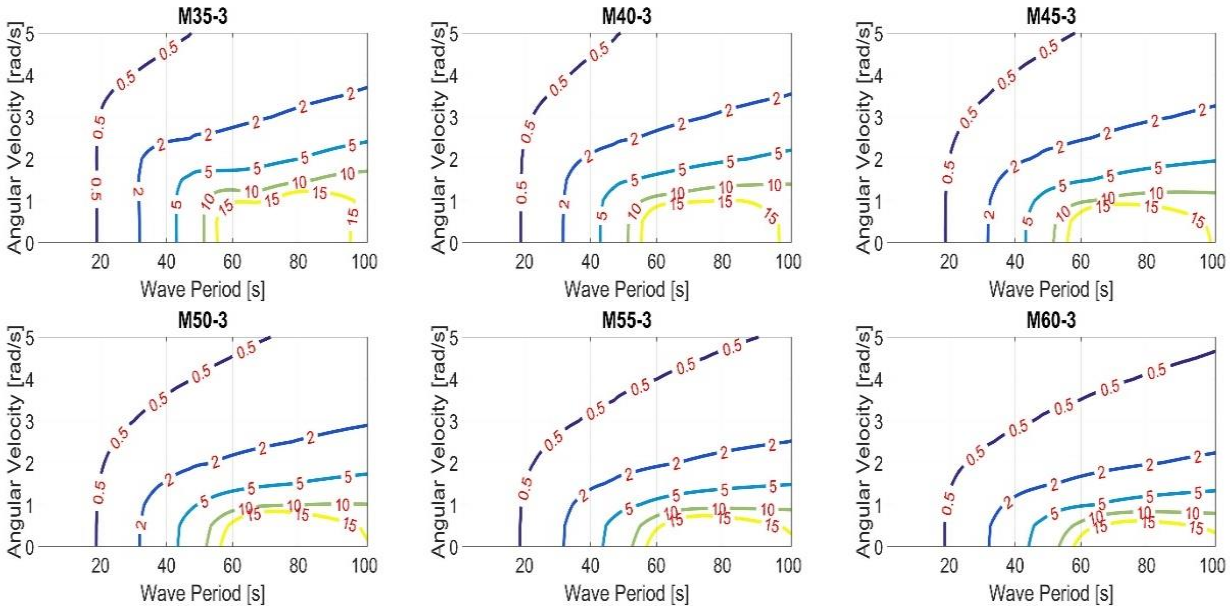

Fig. 4.20 Contour graph of cylinder-type FOWT pitch RAO with distance from center of ring tube to center of torus change

When the angular velocity is 0 rad/s, the natural period of pitch shift from around 70s to the longer period side as the torus volume increase. This is because the increase of weight of cylinder-type FOWT resulting in a smaller GM value, and the rotational inertia and addition mass increase due to the larger torus volume. It can also be confirmed that the RAO of the pitch of FOWT is attenuated quite a few near the natural period as the angular velocity of annular flow increase and a large damping effect could be got even at a relatively small angular velocity. In particular, when the angular velocity is less than 2 rad/s, the distance from center of ring tube to center of torus is over 40m and the radius of ring tube of small torus is over 3m, as with M40-3 in Fig. 4.19 and Fig. 4.20, the dimensionless pitch response value is suppressed to 5 or less in a fairly wide periodic band. It can be considered that a large damping effect could be demonstrated even at a relatively small angular velocity. In addition, the direction of the contour lines is also inclined to parallel to the angular velocity that obviously signify the increase of the angular velocity does not have much effect when the angular velocity exceeds a certain value.

Expected value during irregular wave

In the irregular wave calculation, the **Beaufort** wind scale is assumed as 10 levels of the whole gale, the significant wave height is 9 m and the average wave period is the 20s.

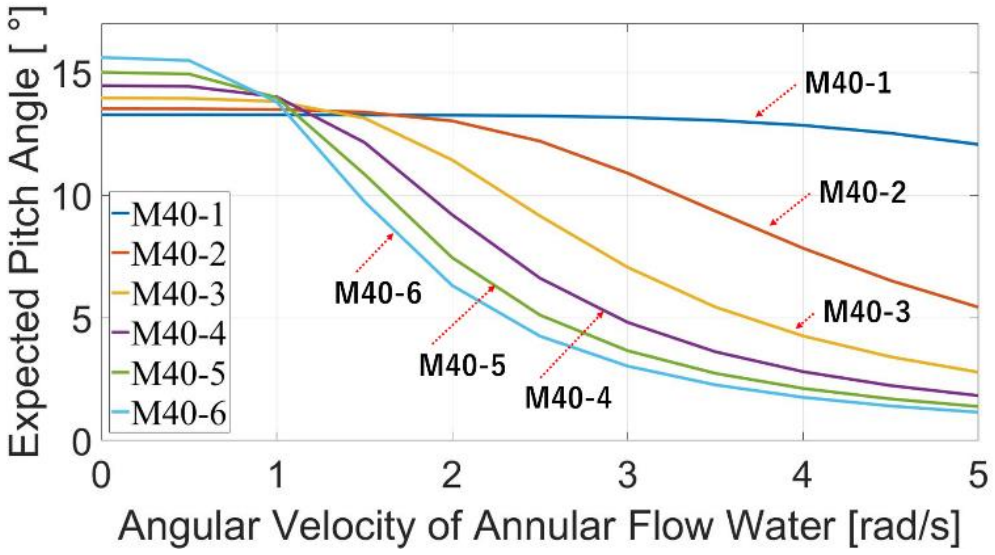

Fig. 4.21 Expected pitch angle of cylinder-type FOWT in the irregular wave with the radius change of ring tube of internal torus

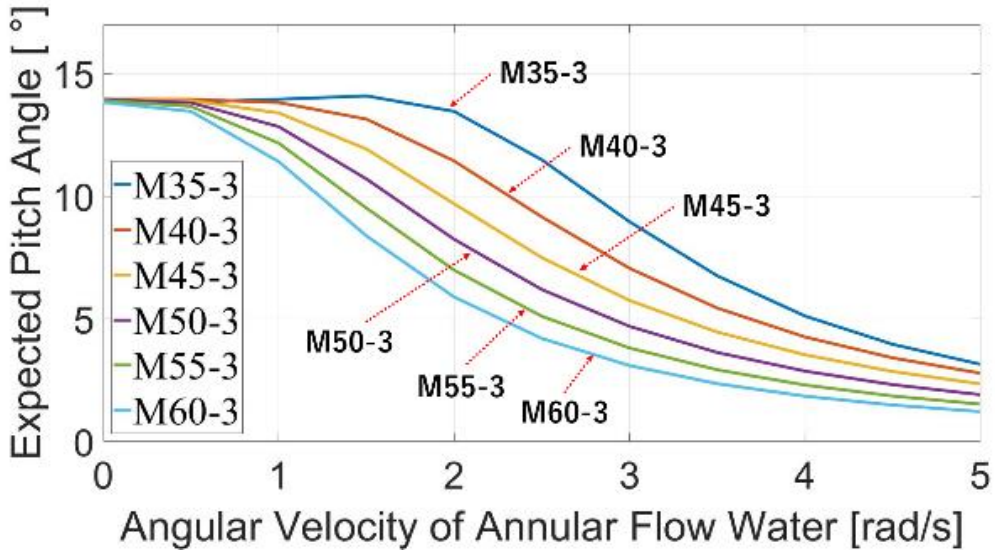

Fig. 4.22 Expected pitch angle of cylinder-type FOWT in the irregular wave with distance from center of ring tube to center of torus change

In the case of the above two kinds of design variables, when any one of the radii is relatively large, the expected value can be suppressed to less than half at the angular velocity is 2 rad/s. At the same time, the expected value can be suppressed to less than half at the angular velocity is 3 rad/s when the radius is relatively small. However, in the case of M40-1, the proportion of moment of inertia of water Jy is less than 1%, the vacillating suppression effect cannot be expected extremely even though the angular velocity is increased tremendously. Moreover, in the case of M40-2, the proportion of moment of inertia of water Jy is less than 3%, the vacillating suppression effect could also be hardly expected highly anyway. Of course, the expected value could not be eliminated to 0 but 0 could be imminent. In addition, with the

proportion of moment of inertia of water Jy get bigger, the vacillating suppression effect does not only increase linearly but also the growth trend become smaller and smaller. Ultimately, it is vindicated that the vacillating suppression effect can be expected even though in the range where the angular velocity is relatively small by setting the proportion of moment of inertia of water Jy to 5% or more.

2. The light cylinder-type FOWT

Tab. 4.8 Cylinder-type FOWT parameters with the radius change of ring tube of internal torus after weight reduction

Item	M40-1	M40-2	M40-3	M40-4	M40-5	M40-6
Distance from Center of Tube to Center of Torus [m]	40					
Radius of Tube of External Torus [m]	1.74	2.7285	3.724	4.7214	5.72	6.7188
Radius of Tube of Internal Torus [m]	**1**	**2**	**3**	**4**	**5**	**6**
KB [m]	16.64	16.17	15.63	15.07	14.58	14.18
KG [m]	9.75	9.53	9.30	9.13	9.04	9.06
GM [m]	13.51	13.03	12.40	11.66	10.86	10.04
Draft [m]	33.15					
Displacement [m^3]	96120	99607	104678	111329	119559	129369
Total Mass [t]	98443	102017	107215	114032	122468	132524
Moment of Inertia Jz [$t \cdot m^2 \times 10^4$]	4743	5242	5914	6731	7666	8698
Moment of Inertia Jx [$t \cdot m^2 \times 10^4$]	11813	12298	12976	13809	14759	15795
Moment of Inertia Jy [$t \cdot m^2 \times 10^4$]	11848	12333	13011	13844	14794	15830
Proportion of Moment of Inertia of water Jz [%]	2.34	8.49	16.38	24.53	32.16	38.95
Proportion of Moment of Inertia of water Jx [%]	1.08	4.13	8.44	13.40	18.54	23.56
Proportion of Moment of Inertia of water Jy [%]	1.08	4.12	8.42	13.37	18.50	23.50

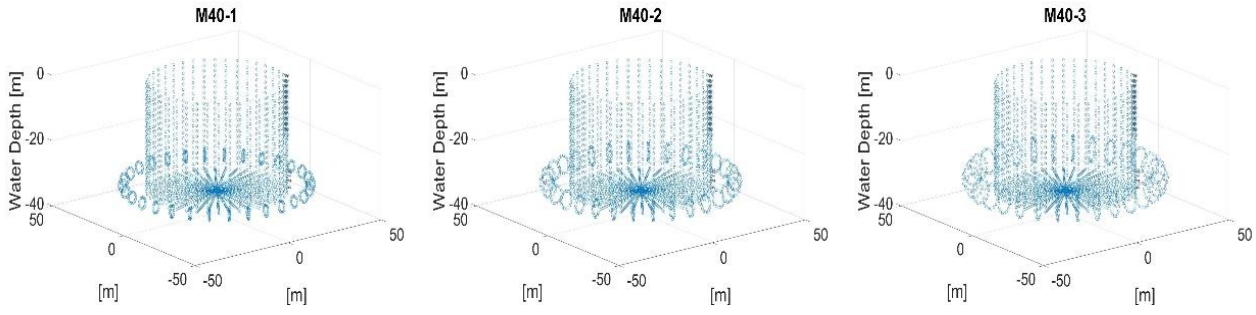

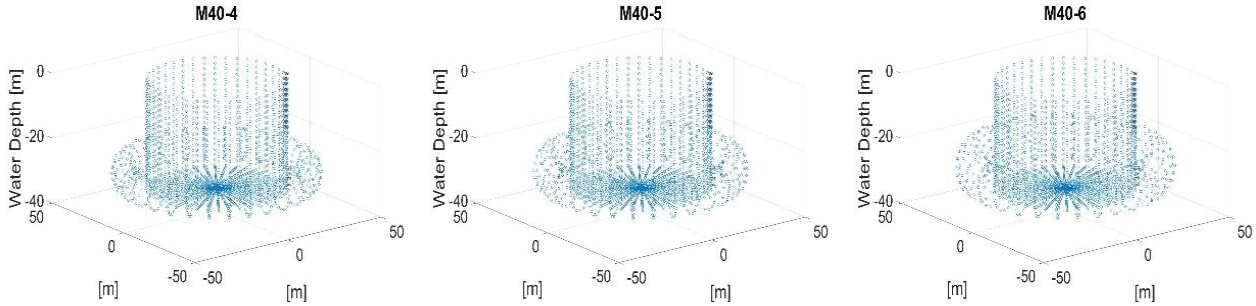

Fig. 4.23 Cylinder-type FOWT wet surface mesh with the radius change of ring tube of internal torus after weight reduction

Tab. 4.9 Cylinder-type FOWT parameters with distance from center of ring tube to center of torus change after weight reduction

Item	M35-3	M40-3	M45-3	M50-3	M55-3	M60-3
Distance from Center of Tube to Center of Torus [m]	**35**	**40**	**45**	**50**	**55**	**60**
Radius of Tube of External Torus [m]	3.719	3.724	3.7275	3.7303	3.7327	3.7346
Radius of Tube of Internal Torus [m]	3					
KB [m]	15.79	15.63	15.47	15.32	15.17	15.02
KG [m]	9.38	9.30	9.23	9.16	9.09	9.02
GM [m]	12.57	12.40	12.24	12.08	11.93	11.77
Draft [m]	33.15					
Displacement [m^3]	103281	104678	106074	107470	108867	110263
Total Mass [t]	105783	107215	108646	110077	111508	112940
Moment of Inertia Jz [$t \cdot m^2 \times 10^4$]	5380	5914	6609	7485	8565	9868
Moment of Inertia Jx [$t \cdot m^2 \times 10^4$]	12683	12976	13321	13723	14188	14725
Moment of Inertia Jy [$t \cdot m^2 \times 10^4$]	12718	13011	13356	13757	14223	14760
Proportion of Moment of Inertia of water Jz [%]	11.80	16.38	21.23	26.06	30.65	34.85
Proportion of Moment of Inertia of water Jx [%]	6.72	8.44	10.43	12.67	15.17	17.90
Proportion of Moment of Inertia of water Jy [%]	6.70	8.42	10.40	12.64	15.13	17.86

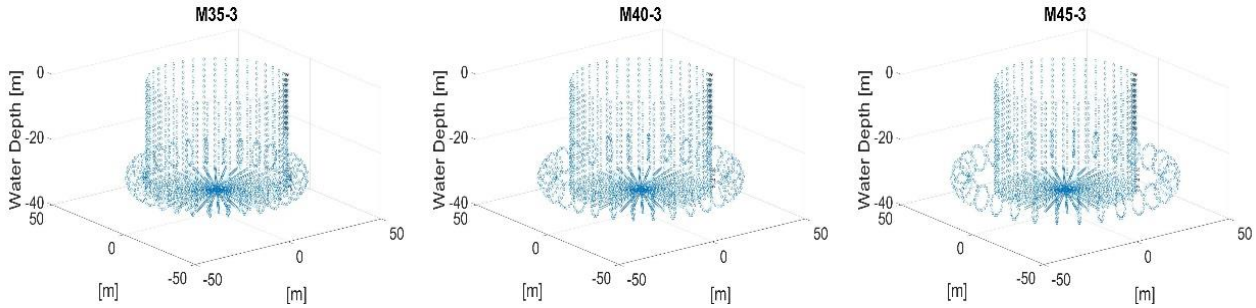

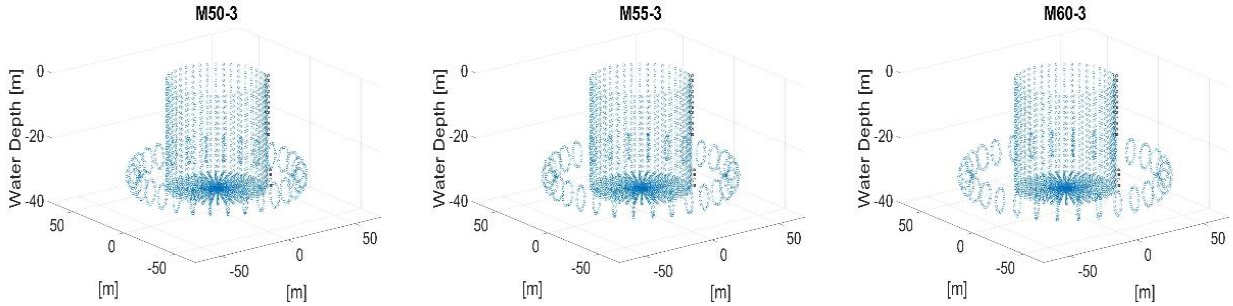

Fig. 4.24 Cylinder FOWT wet surface mesh with distance from center of ring tube to center of torus change after weight reduction

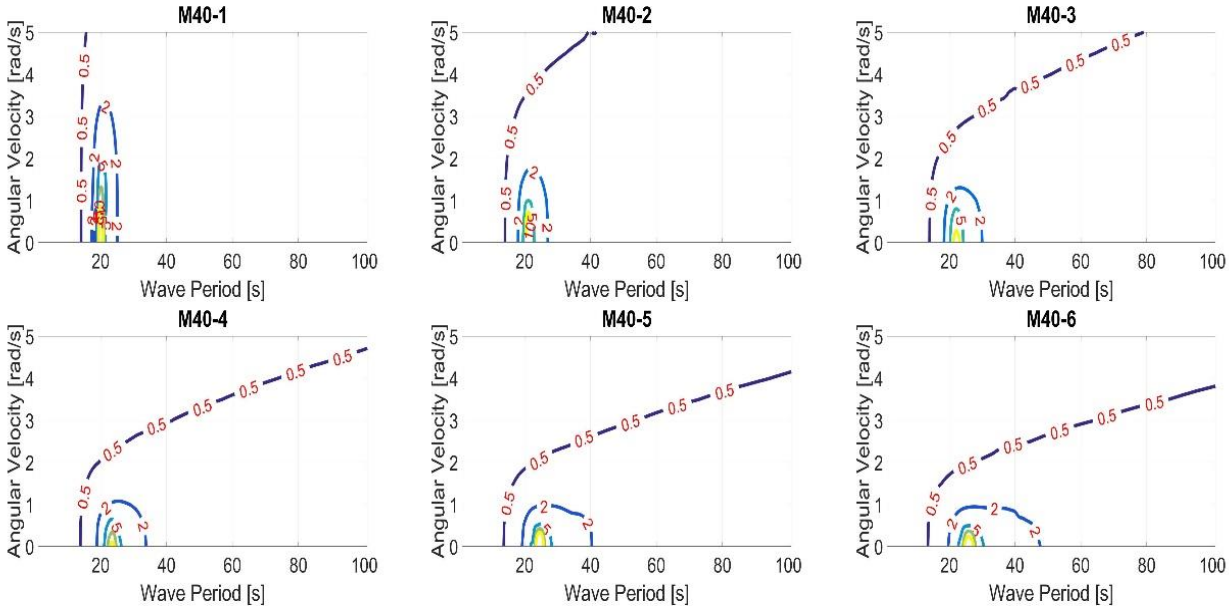

Fig. 4.25 Contour graph of cylinder FOWT pitch RAO with the radius change of ring tube of internal torus after weight reduction

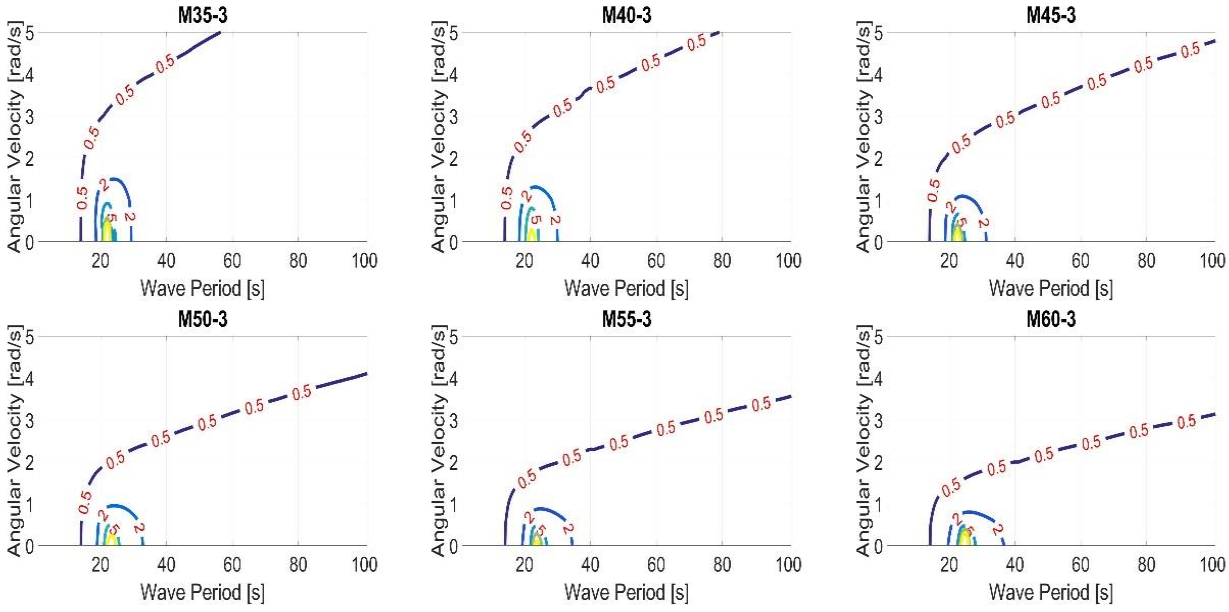

Fig. 4.26 Contour graph of cylinder-type FOWT pitch RAO with distance from center of ring tube to center of torus change after weight reduction

When the angular velocity is 0 rad/s, the natural period of pitch shift from around 20s to the longer period side very small as the torus volume increase. This is because the increase of weight of cylinder-type FOWT resulting in a smaller GM value, and the rotational inertia and addition mass increase due to the larger torus volume. It can also be confirmed that the RAO of the pitch of cylinder-type FOWT is attenuated quite a few near the natural period as the angular velocity of annular flow increase and a large damping effect could be got even at a relatively small angular velocity. In addition, the direction of the contour lines is also inclined to parallel to the angular velocity that obviously signify the increase of the angular velocity does not have much effect when the angular velocity exceeds a certain value.

Expected value during irregular wave

Because the irregular wave with a period of 20s is very close to the natural period of the light cylinder-type FOWT, the expected value of its response will be very large. The calculation in the irregular wave uses the irregular wave with the average wave period is the 10s, and the significant wave height is still 9 m.

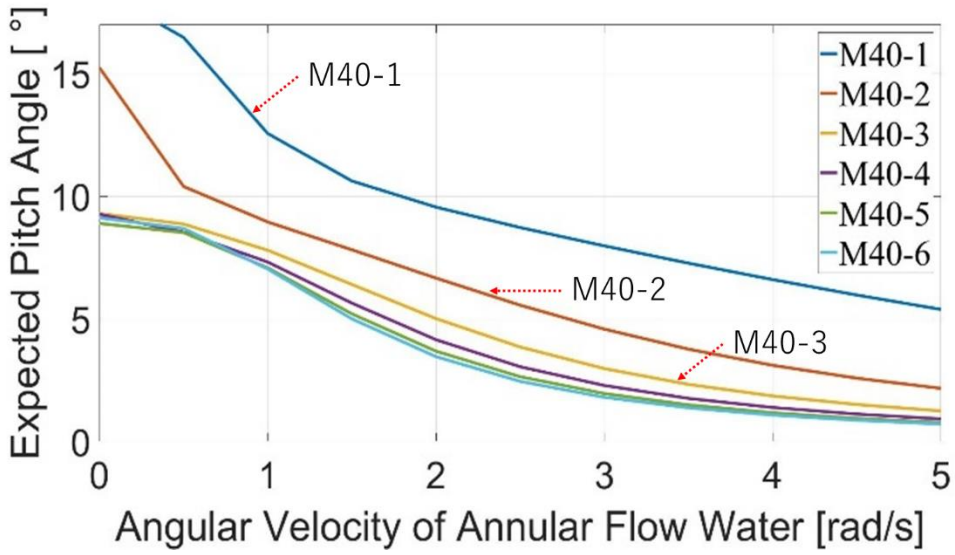

Fig. 4.27 Expected pitch angle of cylinder-type FOWT in the irregular wave with the radius change of ring tube of internal torus after weight reduction

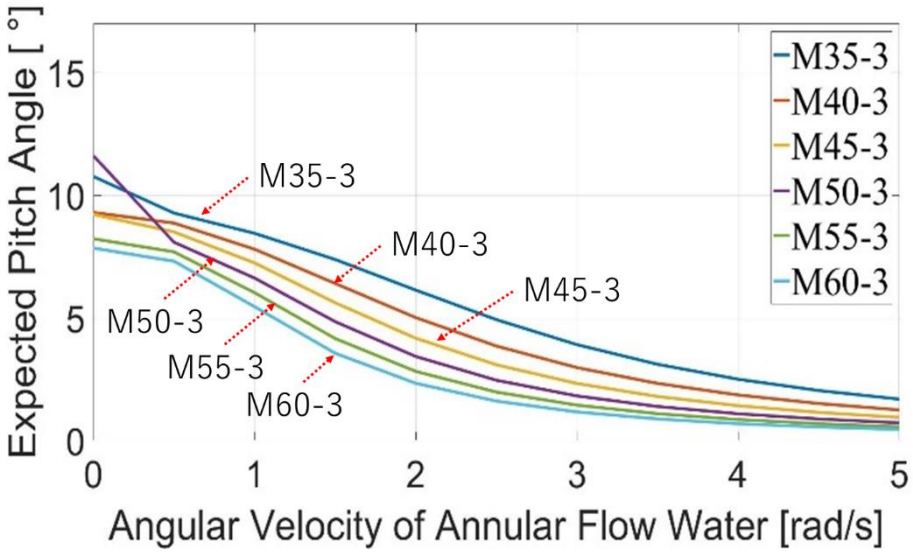

Fig. 4.28 Expected pitch angle of cylinder-type FOWT in the irregular wave with distance from center of ring tube to center of torus change after weight reduction

In the case of the above two kinds of design variables, when any one of the radii is relatively large, the expected value can be suppressed to less than half at the angular velocity is 2 rad/s. At the same time, the expected value can be suppressed to less than half at the angular velocity is 3 rad/s when the radius is relatively small. However, in the case of M40-1, the proportion of moment of inertia of water Jy is about 1%, the vacillating suppression effect cannot be expected extremely even though the angular velocity is increased tremendously. Moreover, in the case of M40-2, the proportion of moment of inertia of water Jy is about 4%, the vacillating suppression effect could be expected a little. Of course, the expected value could not be eliminated to 0 but 0 could be imminent. In addition, with the proportion of moment of inertia of water Jy get bigger, the vacillating suppression effect does not only increase linearly but also the growth trend become smaller and smaller. Ultimately, it is vindicated that the vacillating suppression effect can be expected even though in the range where the angular velocity is relatively small by setting the proportion of moment of inertia of water Jy to 5% or more.

4.3.1.3 Change the Central Cylinder

1. The heavy cylinder-type FOWT

Tab. 4.10 Characteristic parameters of cylinder-type FOWT with central cylinder radius change

Item	M40-3
Distance from Center of Tube to Center of Torus [m]	40

Radius of Tube of External Torus [m]	3.724			
Radius of Tube of Internal Torus [m]	3			
Central Cylinder Height [m]	45			
Ballast Height [m]	12			
Radius of Central Cylinder [m]	**28**	**29**	**31**	**32**
KB [m]	20.48	20.36	20.17	20.08
KG [m]	24.39	23.56	22.06	21.38
GM [m]	0.15	1.24	3.34	4.35
Draft [m]	43.82	43.26	42.29	41.87
Water-plane Area	2463	2642	3019	3217
Displacement [m^3]	118891	125258	138631	145637
Total Mass[t]	121864	128389	142097	149278
Moment of Inertia Jz [$t \cdot m^2 \times 10^4$]	5611	6186	7522	8291
Moment of Inertia Jx [$t \cdot m^2 \times 10^4$]	29210	30101	32012	33036
Moment of Inertia Jy [$t \cdot m^2 \times 10^4$]	29282	30173	32084	33108
Proportion of Moment of Inertia of water Jz [%]	17.27	15.66	12.88	11.68
Proportion of Moment of Inertia of water Jx [%]	5.54	5.27	4.79	4.57
Proportion of Moment of Inertia of water Jy [%]	5.53	5.26	4.78	4.56

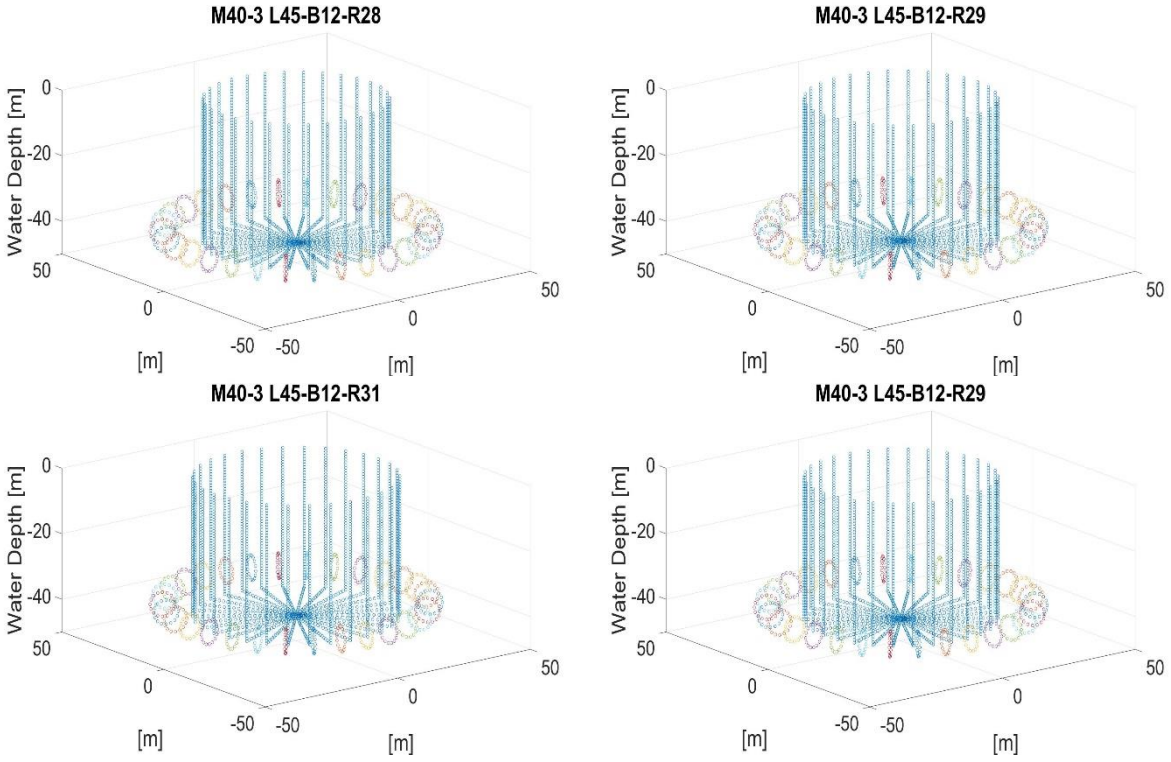

Fig. 4.29 Cylinder-type FOWT wet surface mesh with central cylinder radius change

Tab. 4.11 Characteristic parameters of cylinder-type FOWT with central cylinder height change

Item	M40-3			
Distance from Center of Tube to Center of Torus [m]	40			
Radius of Tube of External Torus [m]	3.724			
Radius of Tube of Internal Torus [m]	3			
Radius of Central Cylinder [m]	30			
Ballast Height [m]	12			
Central Cylinder Height [m]	**43**	**44**	**46**	**47**
KB [m]	19.95	20.11	20.41	20.55
KG [m]	22.41	22.60	22.98	23.17
GM [m]	2.39	2.35	2.24	2.19
Draft [m]	42.55	42.65	42.86	42.96
Displacement [m^3]	131260	131549	132127	132415
Total Mass[t]	134542	134838	135430	135726
Moment of Inertia Jz [$t \cdot m^2 \times 10^4$]	6782	6802	6842	6862
Moment of Inertia Jx [$t \cdot m^2 \times 10^4$]	30292	30661	31413	31798
Moment of Inertia Jy [$t \cdot m^2 \times 10^4$]	30364	30733	31486	31870
Proportion of Moment of Inertia of water Jz [%]	14.28	14.24	14.16	14.12
Proportion of Moment of Inertia of water Jx [%]	5.11	5.07	4.98	4.94
Proportion of Moment of Inertia of water Jy [%]	5.10	5.05	4.97	4.93

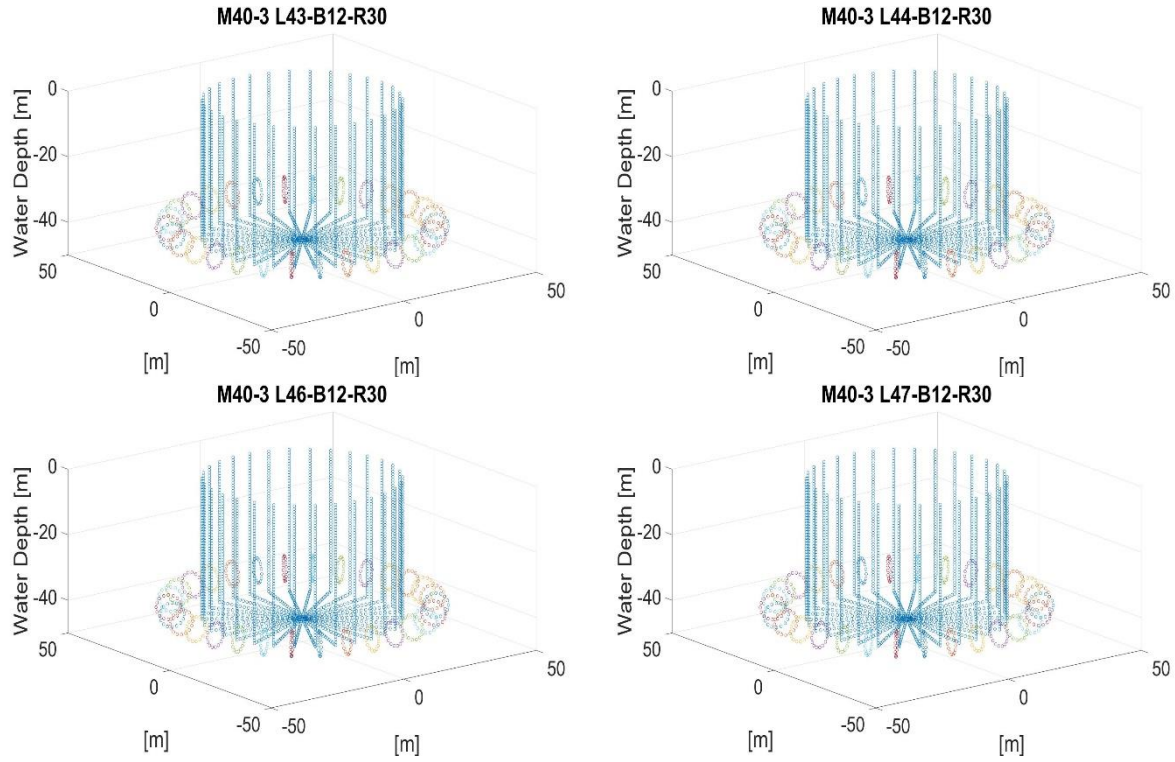

Fig. 4.30 Cylinder-type FOWT wet surface mesh with central cylinder height change

Tab. 4.12 Characteristic parameters of FOWT with central cylinder wall thickness change

Item	M40-3			
Distance from Center of Tube to Center of Torus [m]	40			
Radius of Tube of External Torus [m]	3.724			
Radius of Tube of Internal Torus [m]	3			
Radius of Central Cylinder [m]	30			
Ballast Height [m]	12			
Central Cylinder Height [m]	45			
Central Cylinder wall thickness [m]	**0.01**	**0.05**	**0.1**	**0.2**
KB [m]	18.42	18.95	19.60	20.91
KG [m]	22.60	22.66	22.73	22.84
GM [m]	1.23	1.52	1.90	2.71
Draft [m]	37.70	39.14	40.95	44.56
Displacement [m^3]	117538	121627	126735	136936
Total Mass[t]	120476	124668	129903	140359
Moment of Inertia Jz [$t \cdot m^2 \times 10^4$]	5749	6057	6440	7203
Moment of Inertia Jx [$t \cdot m^2 \times 10^4$]	27550	28434	29662	32562
Moment of Inertia Jy [$t \cdot m^2 \times 10^4$]	27622	28506	29734	32634
Proportion of Moment of Inertia of water Jz [%]	16.85	16.00	15.04	13.45
Proportion of Moment of Inertia of water Jx [%]	4.71	4.82	4.93	5.10
Proportion of Moment of Inertia of water Jy [%]	4.70	4.80	4.92	5.09

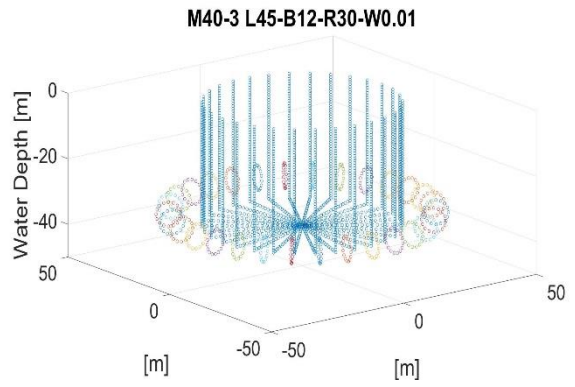

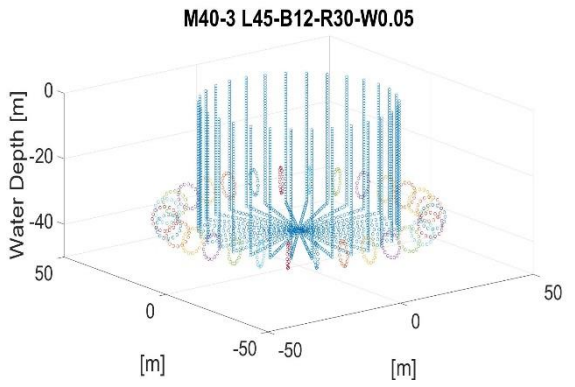

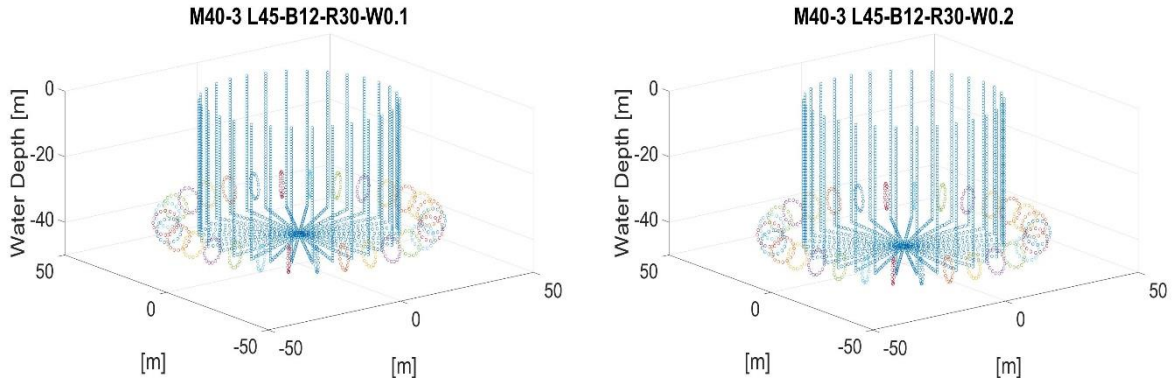

Fig. 4.31 Cylinder-type FOWT wet surface mesh with central cylinder wall thickness change

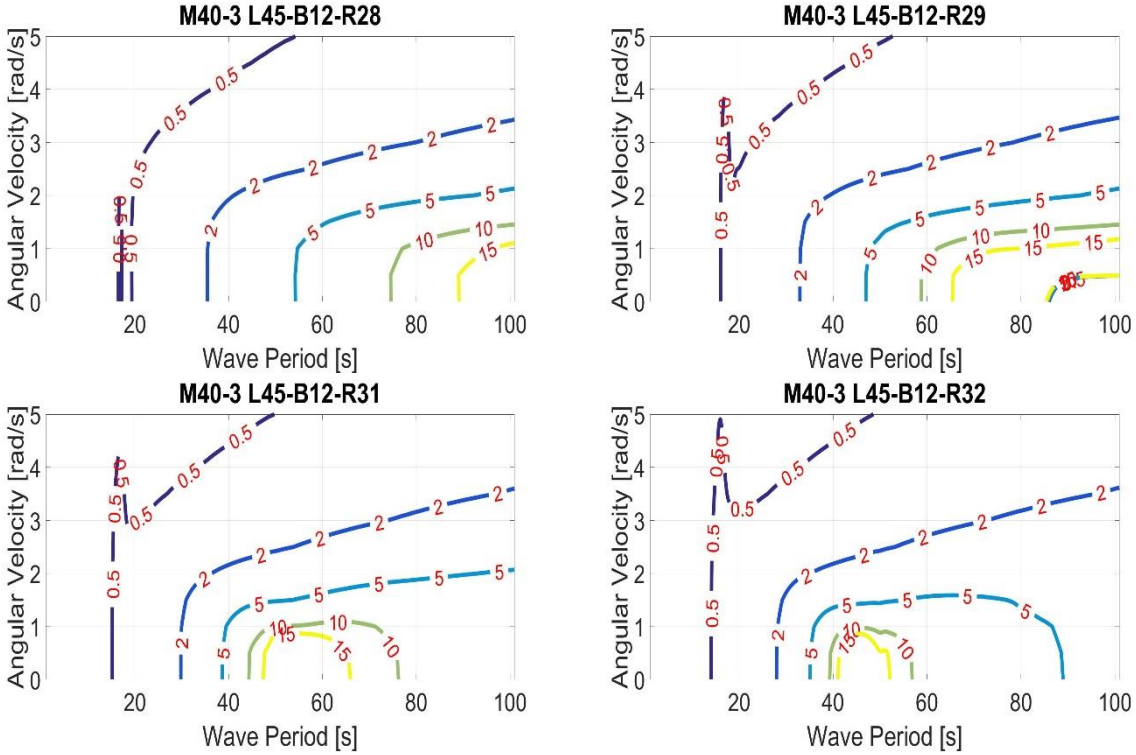

Fig. 4.32 Contour graph of cylinder-type FOWT pitch RAO with central cylinder radius change

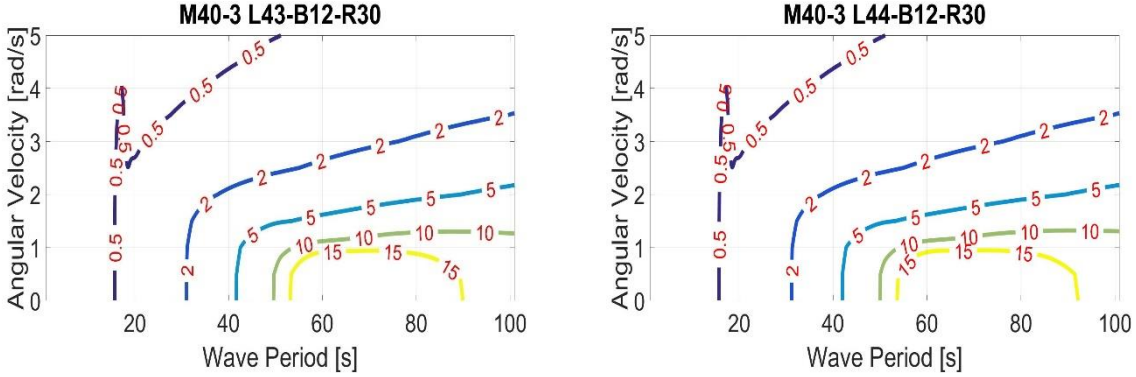

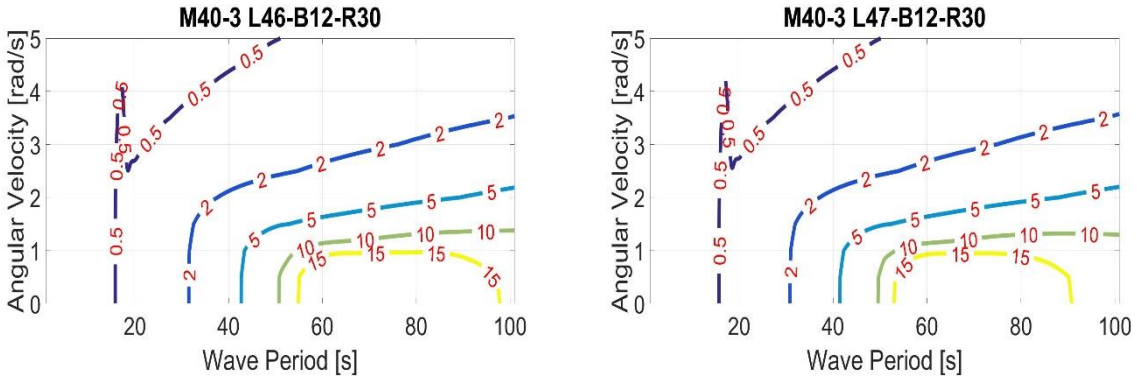

Fig. 4.33 Contour graph of cylinder-type FOWT pitch RAO with central cylinder height change

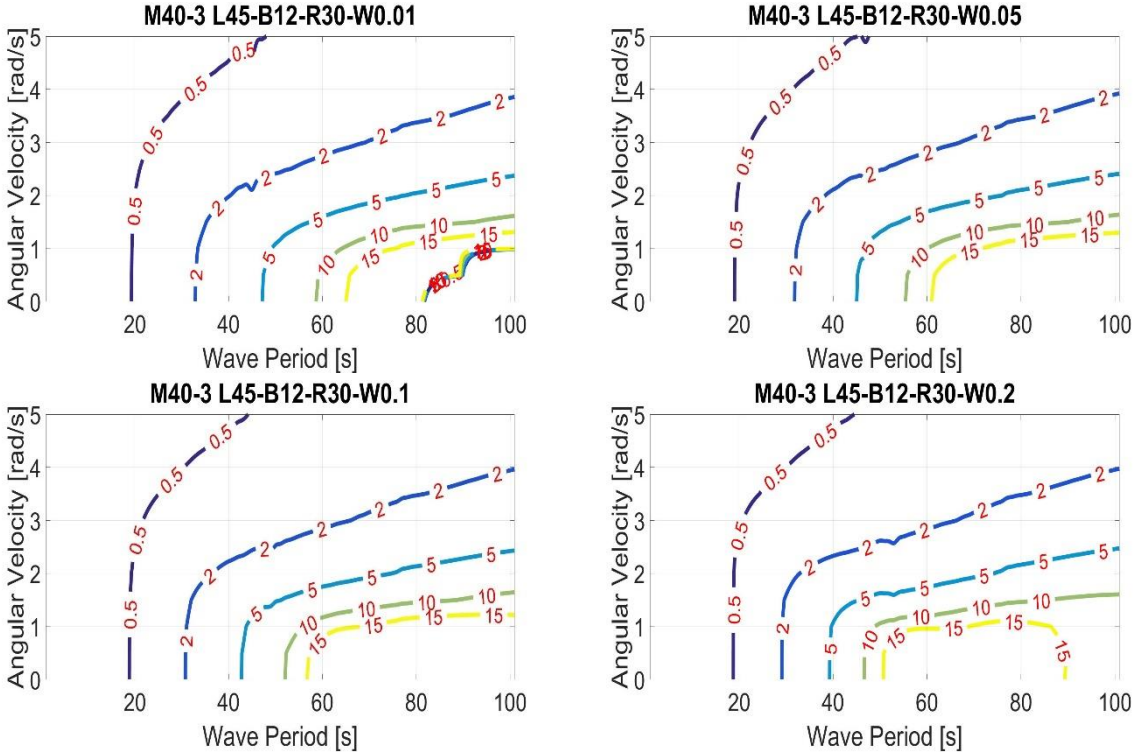

Fig. 4.34 Contour graph of cylinder-type FOWT pitch RAO with central cylinder wall thickness change

When the angular velocity is 0 rad/s, the natural period of pitch shift from around 70s to the shorter period side as the torus volume increase. This is because the increase of weight of cylinder-type FOWT resulting in a bigger GM value, and the rotational inertia and addition mass increase due to the larger torus volume. It can also be confirmed that the RAO of the pitch of FOWT is attenuated quite a few near the natural period as the angular velocity of annular flow increase and a large damping effect could be got even at a relatively small angular velocity. In particular, when the angular velocity is less than 2 rad/s, the dimensionless pitch response value is suppressed to 5 or less in a fairly wide periodic band. It can be considered

that a large damping effect could be demonstrated even at a relatively small angular velocity. In addition, the direction of the contour lines is also inclined to parallel to the angular velocity that obviously signify the increase of the angular velocity does not have much effect when the angular velocity exceeds a certain value.

Expected value during irregular wave

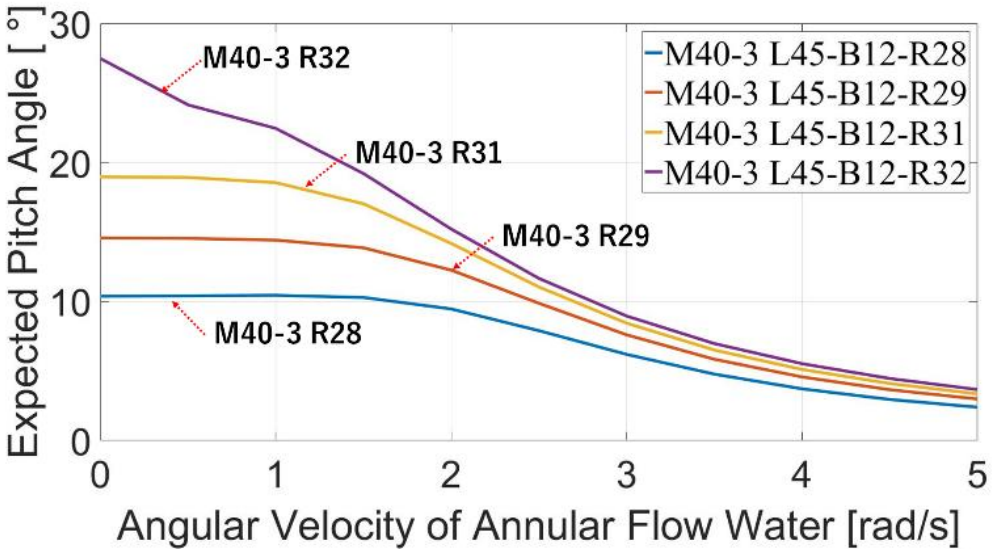

Fig. 4.35 Expected pitch angle in the irregular wave with the central cylinder radius change

From Fig. 4.35, we can see that as the central cylinder radius increases from 28 m to 32 m, when the angular velocity of annular flow is relatively low, its hydrodynamic performance becomes worse and worse very much. At this time, although GM increases from 0.15 m to 4.35 m, but the water-plane area become larger from 2463 m^2 to 3217 m^2, which lead to the natural period of FOWT is reduced from over 100s to about 40s, which is very close to the average wave period of the irregular wave, so expected value become lager, even up to 28° , far greater than the limit value used in the FOWT design. When the angular velocity of the annular flow reaches 3 rad/s, the hydrodynamic response tends to be the same, because the proportion of the moment of inertia Jy occupied by the water part of the annular flow only slightly reduces from 5.54% to 4.57%.

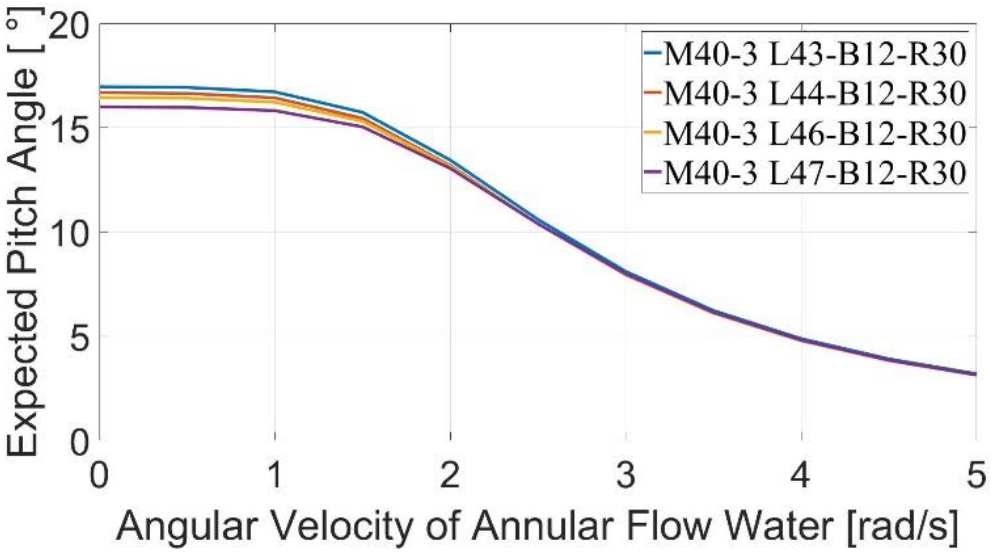

Fig. 4.36 Expected pitch angle in the irregular wave with the central cylinder height change

From Fig. 4.36, we can see that as the central cylinder height increases from 43 m to 47 m, no matter how large the angular velocity of annular flow is, its hydrodynamic performance is similar, since the GM only changes from 2.39 m to 2.19 m, and the proportion of the moment of inertia Jy occupied by the water part of the annular flow only slightly reduces from 5.11% to 4.94%.

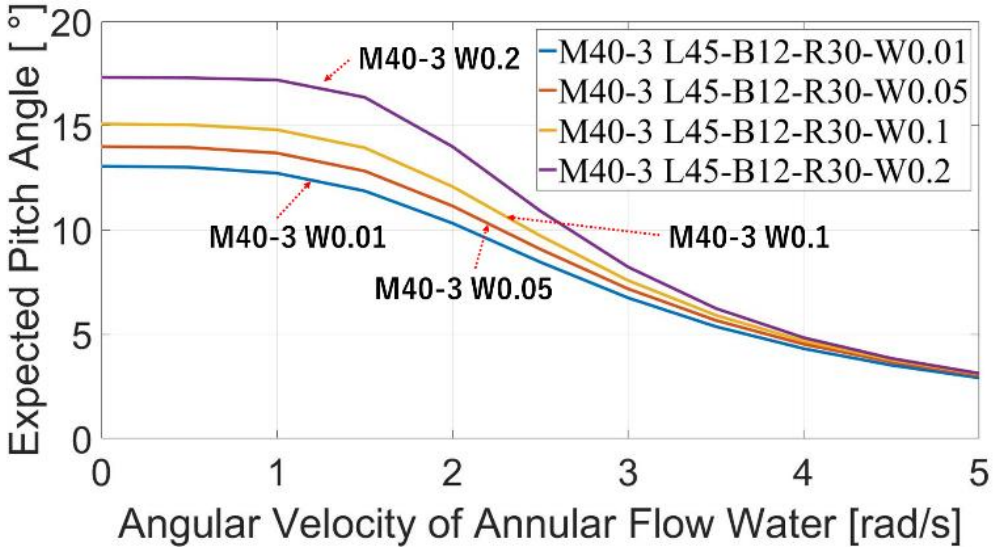

Fig. 4.37 Expected pitch angle in the irregular wave with the central cylinder wall thickness change

From Fig. 4.37, we can see that as the central cylinder wall thickness increases from 0.01 m to 0.2 m, when the angular velocity of annular flow is relatively low, its hydrodynamic

performance becomes worse and worse. At this time, GM increases from 1.23 m to 2.71 m. When the angular velocity of the annular flow reaches 3 rad/s, the hydrodynamic response tends to be the same, because the proportion of the moment of inertia Jy occupied by the water part of the annular flow only slightly increases from 4.70% to 5.10%. Therefore, the calculation of appropriate scale design parameters for annular flow in this Section is universal.

2. The light cylinder-type FOWT

Tab. 4.13 Characteristic parameters of cylinder-type FOWT with central cylinder radius change

Item	M40-3			
Distance from Center of Tube to Center of Torus [m]	40			
Radius of Tube of External Torus [m]	3.724			
Radius of Tube of Internal Torus [m]	3			
Central Cylinder Height [m]	35			
Ballast Height [m]	12			
Radius of Central Cylinder [m]	28	29	31	32
KB [m]	15.48	15.56	15.69	15.75
KG [m]	9.66	9.47	9.14	8.99
GM [m]	11.03	11.72	13.09	13.77
Draft [m]	33.20	33.17	33.12	33.10
Water-plane Area	2463	2642	3019	3217
Displacement [m^3]	92734	98604	110955	117435
Total Mass[t]	95053	101069	113729	120371
Moment of Inertia Jz [$t \cdot m^2 \times 10^4$]	4870	5365	6521	7189
Moment of Inertia Jx [$t \cdot m^2 \times 10^4$]	11593	12264	13732	14533
Moment of Inertia Jy [$t \cdot m^2 \times 10^4$]	11628	12299	13767	14568
Proportion of Moment of Inertia of water Jz [%]	19.89	18.06	14.86	13.48
Proportion of Moment of Inertia of water Jx [%]	9.47	8.94	7.97	7.53
Proportion of Moment of Inertia of water Jy [%]	9.44	8.92	7.95	7.51

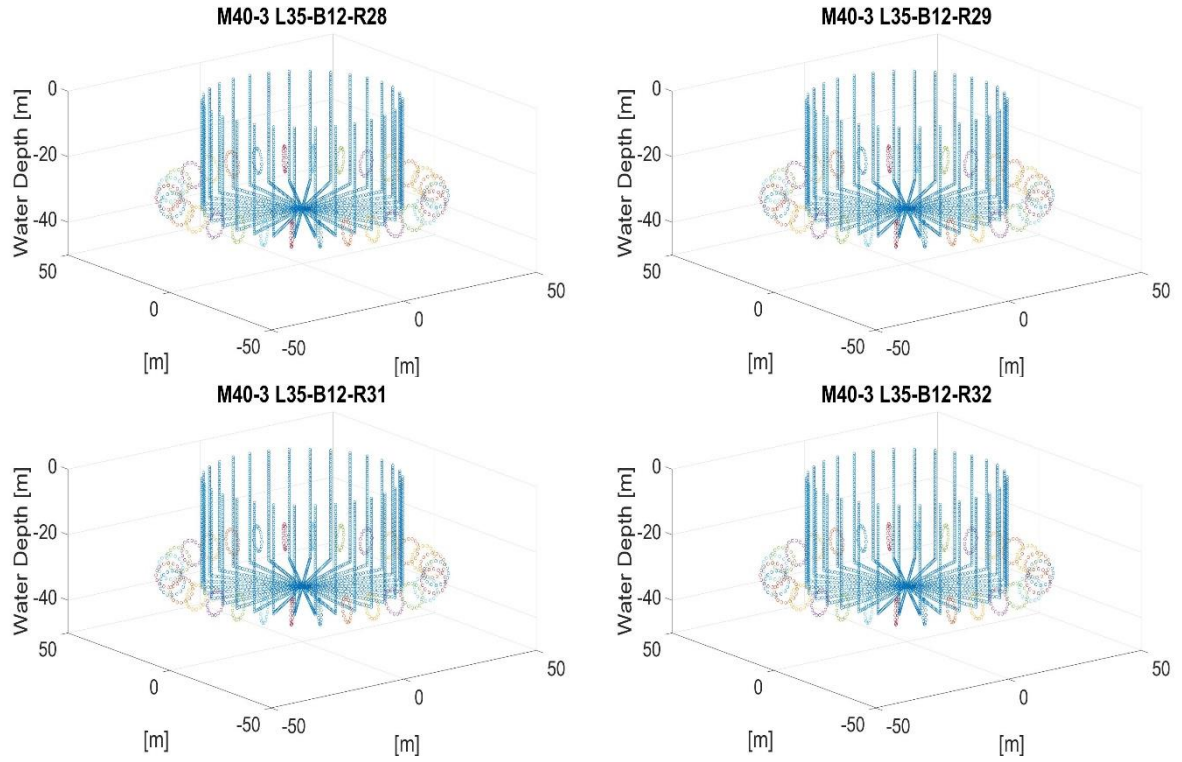

Fig. 4.38 Cylinder-type FOWT wet surface mesh with central cylinder radius change

Tab. 4.14 Characteristic parameters of cylinder-type FOWT with central cylinder height change

Item	M40-3			
Distance from Center of Tube to Center of Torus [m]	40			
Radius of Tube of External Torus [m]	3.724			
Radius of Tube of Internal Torus [m]	3			
Radius of Central Cylinder [m]	30			
Ballast Height [m]	12			
Central Cylinder Height [m]	33	34	36	37
KB [m]	15.32	15.47	15.77	15.91
KG [m]	9.20	9.25	9.35	9.40
GM [m]	12.20	12.31	12.49	12.57
Draft [m]	33.09	33.12	33.18	33.20
Displacement [m^3]	104523	104600	104755	104832
Total Mass[t]	107136	107215	107374	107453
Moment of Inertia Jz [$t \cdot m^2 \times 10^4$]	5901	5908	5921	5928
Moment of Inertia Jx [$t \cdot m^2 \times 10^4$]	12843	12909	13044	13113
Moment of Inertia Jy [$t \cdot m^2 \times 10^4$]	12878	12944	13079	13148
Proportion of Moment of Inertia of water Jz [%]	16.42	16.40	16.36	16.34
Proportion of Moment of Inertia of water Jx [%]	8.51	8.48	8.41	8.37
Proportion of Moment of Inertia of water Jy [%]	8.49	8.46	8.39	8.35

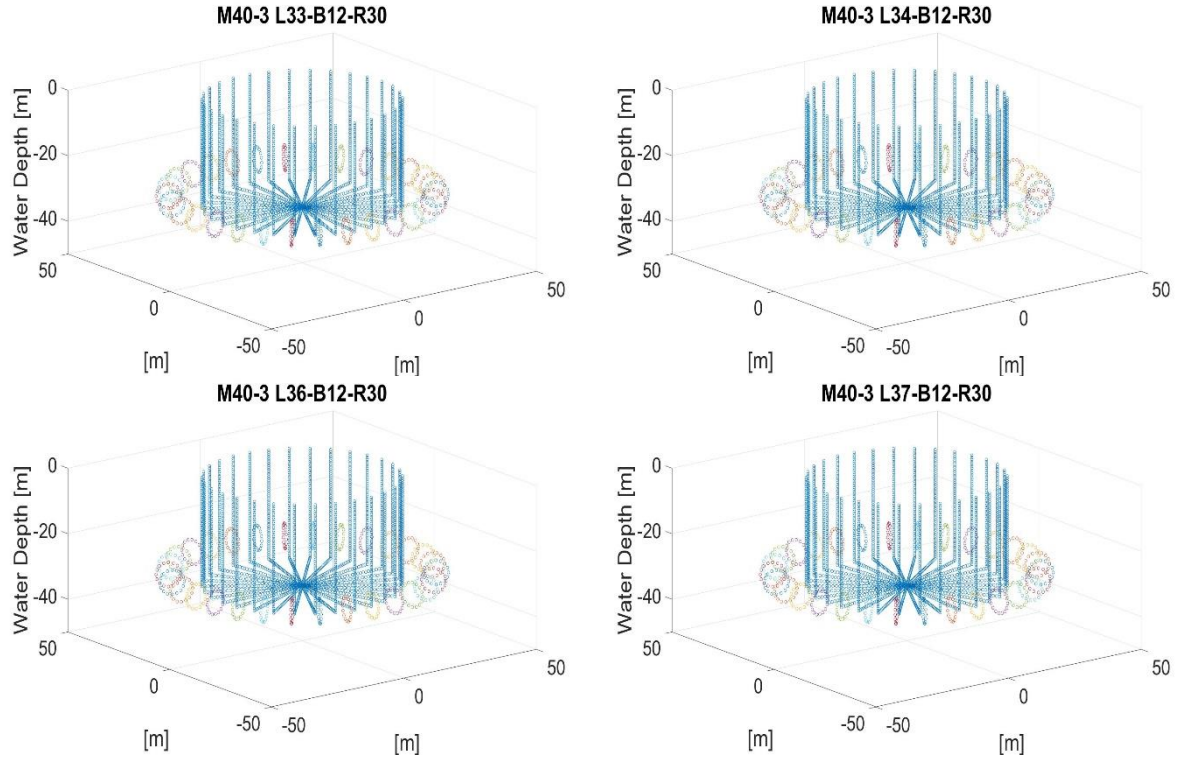

Fig. 4.39 Cylinder-type FOWT wet surface mesh with central cylinder height change

Tab. 4.15 Characteristic parameters of cylinder-type FOWT with central cylinder wall thickness change

Item	M40-3		
Distance from Center of Tube to Center of Torus [m]	40		
Radius of Tube of External Torus [m]	3.724		
Radius of Tube of Internal Torus [m]	3		
Radius of Central Cylinder [m]	30		
Ballast Height [m]	12		
Central Cylinder Height [m]	35		
Central Cylinder wall thickness [m]	**0.01**	**0.05**	**0.1**
KB [m]	15.22	15.63	16.13
KG [m]	8.95	9.30	9.70
GM [m]	12.55	12.40	12.26
Draft [m]	31.91	33.15	34.70
Displacement [m^3]	101165	104678	109066
Total Mass[t]	103694	107295	111792
Moment of Inertia Jz [$t \cdot m^2 \times 10^4$]	5660	5914	6232
Moment of Inertia Jx [$t \cdot m^2 \times 10^4$]	12107	12976	14144
Moment of Inertia Jy [$t \cdot m^2 \times 10^4$]	12142	13011	14179

Proportion of Moment of Inertia of water Jz [%]	17.12	16.38	15.55
Proportion of Moment of Inertia of water Jx [%]	8.63	8.44	8.21
Proportion of Moment of Inertia of water Jy [%]	8.61	8.42	8.19

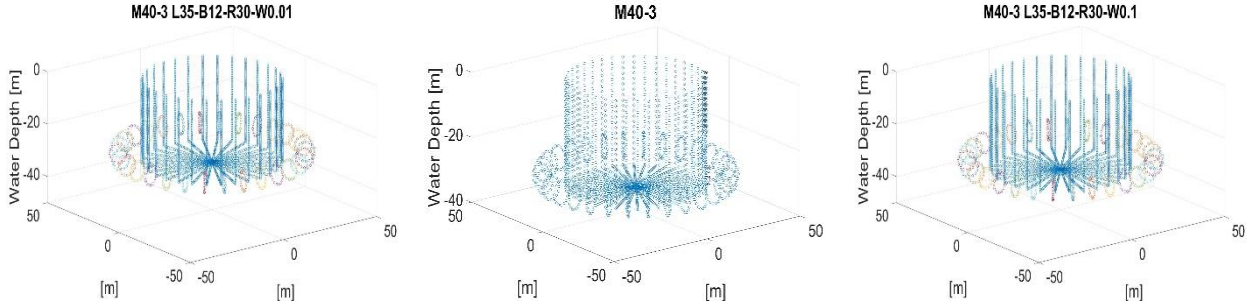

Fig. 4.40 Cylinder-type FOWT wet surface mesh with central cylinder wall thickness change

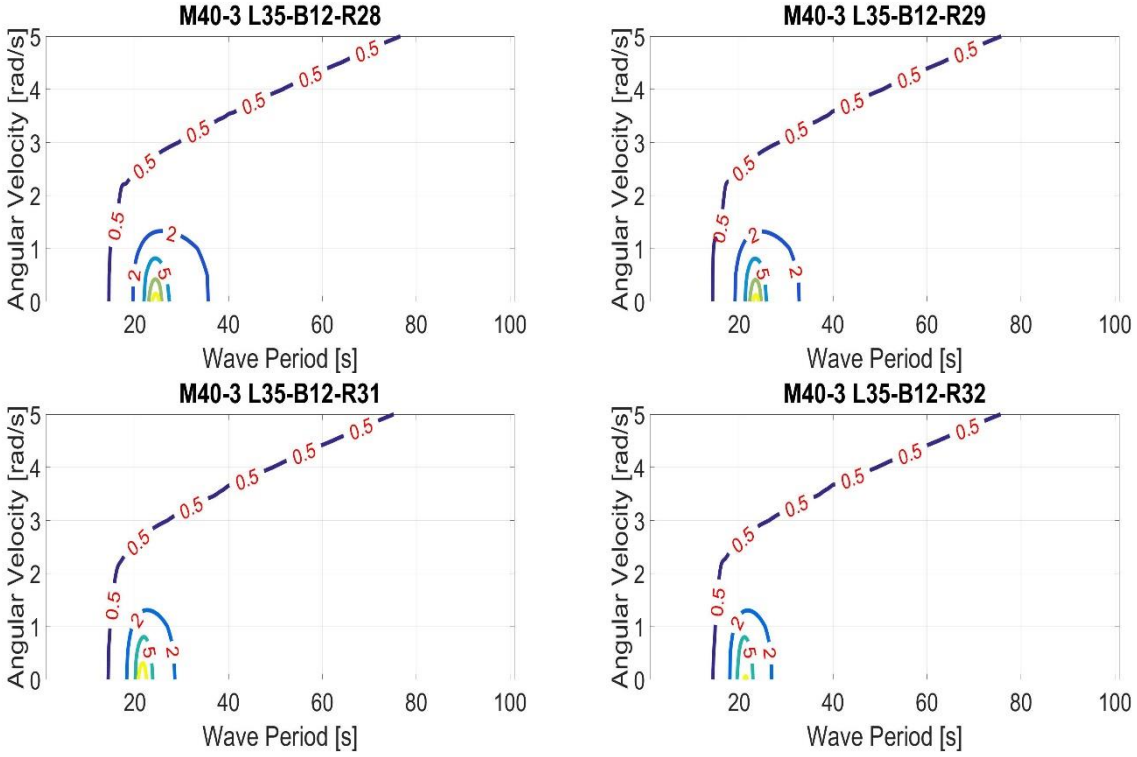

Fig. 4.41 Contour graph of cylinder-type FOWT pitch RAO with central cylinder radius change

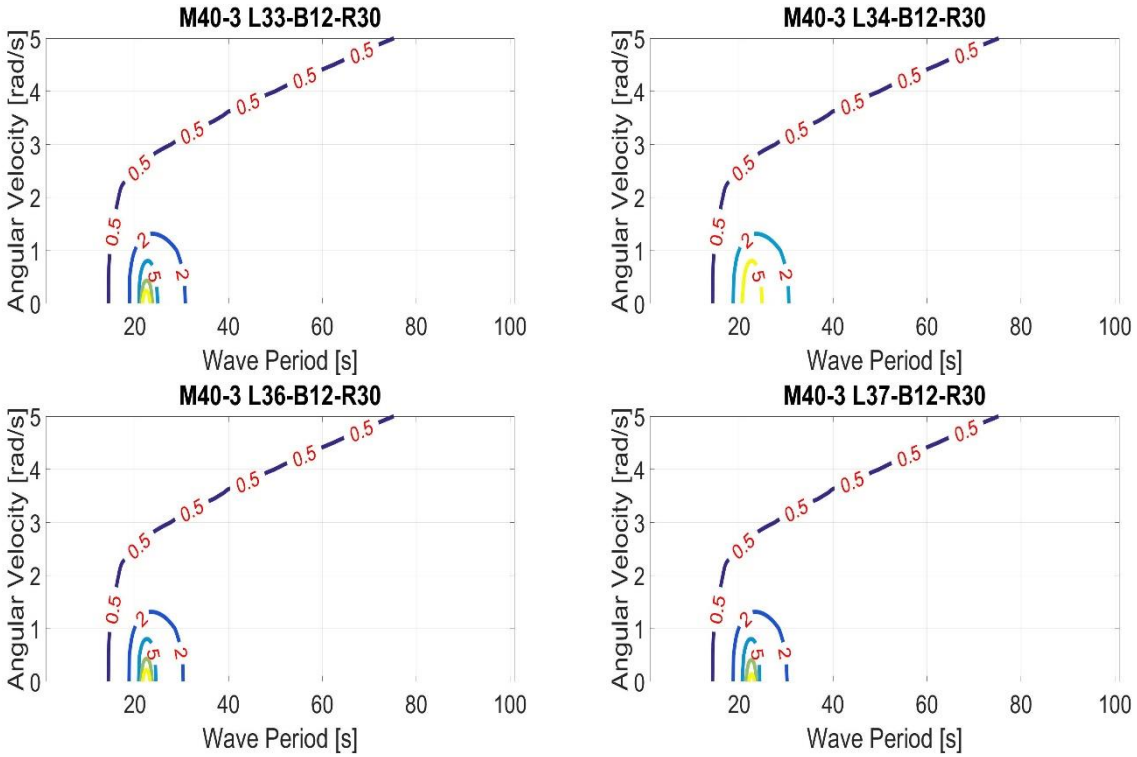

Fig. 4.42 Contour graph of cylinder-type FOWT pitch RAO with central cylinder height change

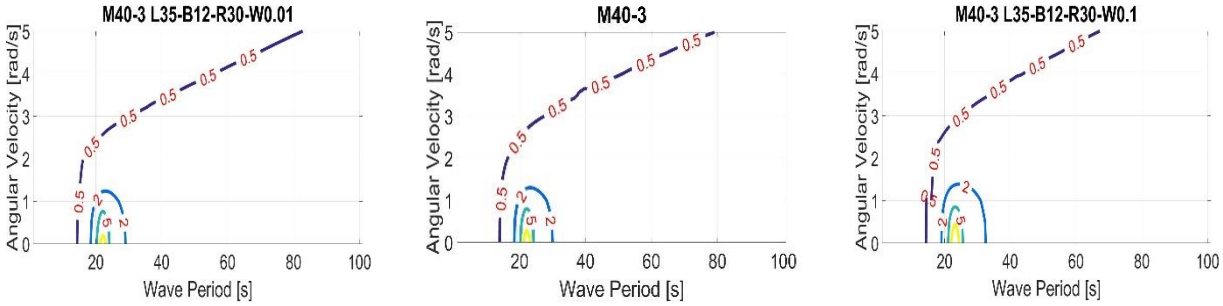

Fig. 4.43 Contour graph of cylinder-type FOWT pitch RAO with central cylinder wall thickness change

When the angular velocity is 0 rad/s, the natural period of pitch shift from around 20s to the shorter period side as the torus volume increase. This is because the increase of weight of cylinder-type FOWT resulting in a bigger GM value. It can also be confirmed that the RAO of the pitch of FOWT is attenuated quite a few near the natural period as the angular velocity of annular flow increase and a large damping effect could be got even at a relatively small angular velocity. In addition, the direction of the contour lines is also inclined to parallel to the angular velocity that obviously signify the increase of the angular velocity does not have much effect when the angular velocity exceeds a certain value.

Expected value during irregular wave

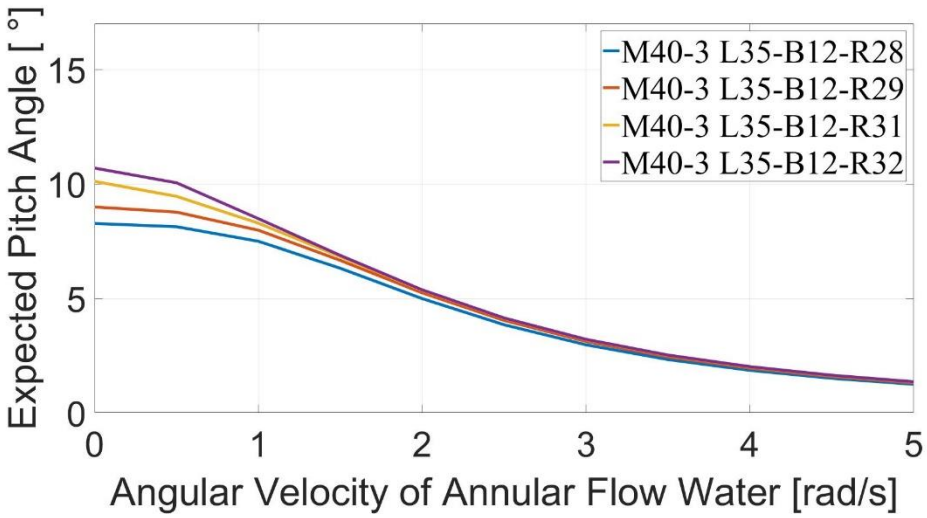

Fig. 4.44 Expected pitch angle in the irregular wave with the central cylinder radius change

From Fig. 4.44, we can see that as the central cylinder radius increases from 28 m to 32 m, when the angular velocity of annular flow is relatively low, its hydrodynamic performance becomes worse and worse very much. At this time, GM increases from 11.03 m to 13.77 m, and the change is very large, When the angular velocity of the annular flow reaches 3rad/s, the hydrodynamic response tends to be the same, because the proportion of the moment of inertia Jy occupied by the water part of the annular flow only slightly reduces from 9.44% to 7.51%.

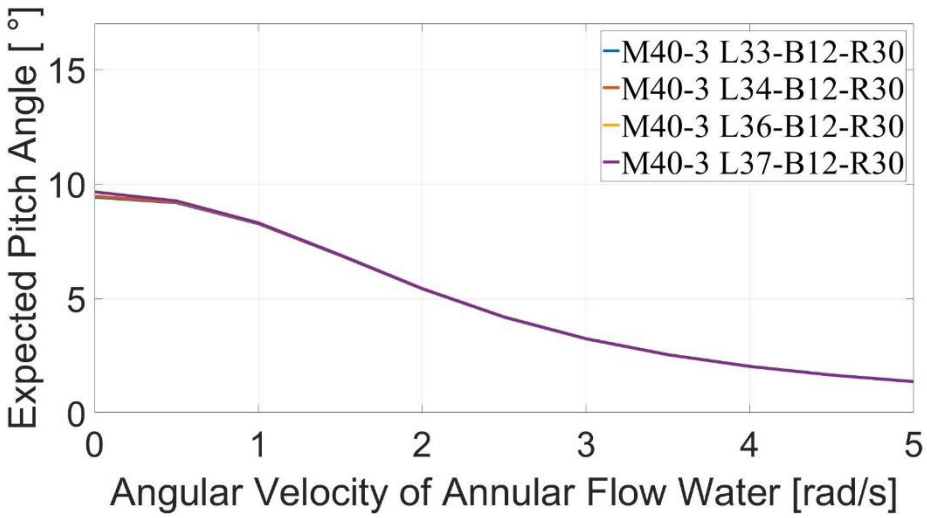

Fig. 4.45 Expected pitch angle in the irregular wave with the central cylinder height change

From Fig. 4.45, we can see that as the central cylinder height increases from 43 m to 47 m, no matter how large the angular velocity of annular flow is, its hydrodynamic performance is

similar, since the GM only changes from 12.02 m to 12.57 m, and the proportion of the moment of inertia Jy occupied by the water part of the annular flow only slightly reduces from 8.51% to 8.37%.

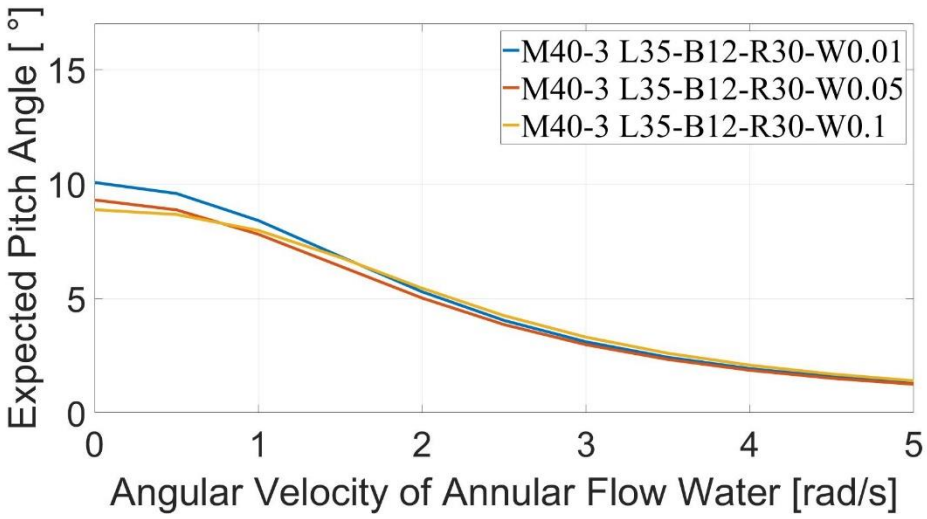

Fig. 4.46 Expected pitch angle in the irregular wave with the central cylinder wall thickness change

From Fig. 4.46, we can see that as the central cylinder wall thickness increases from 0.01 m to 0.2 m, when the angular velocity of annular flow is relatively low, its hydrodynamic performance becomes worse and worse. At this time, GM increases from 12.55 m to 12.26 m. When the angular velocity of the annular flow reaches 3 rad/s, the hydrodynamic response tends to be the same, because the proportion of the moment of inertia Jy occupied by the water part of the annular flow only slightly increases from 8.61% to 8.19%. Therefore, the calculation of appropriate scale design parameters for annular flow in this Section is universal.

4.3.2 The SPAR-type FOWT

4.3.2.1 Change the Heights of the Torus Structure

The SPAR-type FOWT with buoyancy providing part and tower section shown in Fig. 4.47 and Tab. 4.16. Particularly, when the torus is located in the middle, it means move the torus structure up 30 m; when the torus is located in the top, it means move the torus structure up 60 m.

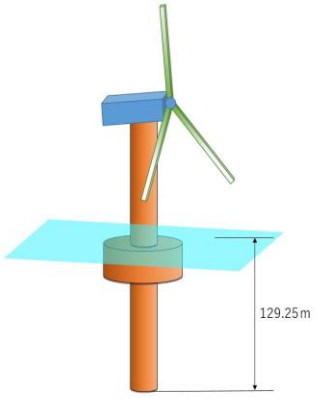

Fig. 4.47 designed SPAR-type FOWT

Tab. 4.16 Parameters of SPAR-type FOWT

Item	Unit [m]	Unit [m]
Cylinder Radius	**20**	**10**
Cylinder Height	38	38
Cylinder Wall Thickness	**0.1**	**0.05**
Stone Ballast Height	80	80
Nacelle Wall Thickness	**0.8**	**0.2**
Support Hollow Cylinder Radius	5	5
Support Hollow Cylinder Length	248	248
Support Hollow Cylinder Wall Thickness	**0.2**	**0.05**

1. The heavy SPAR-type FOWT

Tab. 4.17 Parameters of model without torus, M20-3 and M20-7

Item	without Torus	M20-3 bottom	M20-3 middle	M20-3 top	M20-7 bottom	M20-7 middle	M20-7 top
Distance from Center of Tube to Torus [m]	0	20	20	20	20	20	20
Radius of Tube of External Torus [m]	0	3.741	3.741	3.741	7.724	7.724	7.724
Radius of Tube of Internal Torus [m]	**0**	**3**	**3**	**3**	**7**	**7**	**7**
KB [m]	92.67	84.53	87.28	90.03	67.17	76.18	85.18
KG [m]	88.42	80.66	83.41	86.16	64.19	73.20	82.20
GM [m]	4.27	3.88			2.99		
Draft [m]	129.25						
Displacement [m^3]	54921	60455			78480		
Total Mass[t]	56294	61966			80442		
Moment of Inertia Jz [$t \cdot m^2 \times 10^4$]	346	516			850		
Moment of Inertia Jx [$t \cdot m^2 \times 10^4$]	52181	61166	57409	54672	88072	72641	61556
Moment of Inertia Jy [$t \cdot m^2 \times 10^4$]	52253	61238	57481	54744	88144	72713	61628
Proportion of Moment of Inertia of water Jz [%]	0	20.16			47.18		
Proportion of Moment of Inertia of water Jx [%]	0	9.15	5.69	2.86	33.03	22.85	12.38
Proportion of Moment of Inertia of water Jy [%]	0	9.14	5.68	2.86	33.00	22.83	12.37

1) M20-3

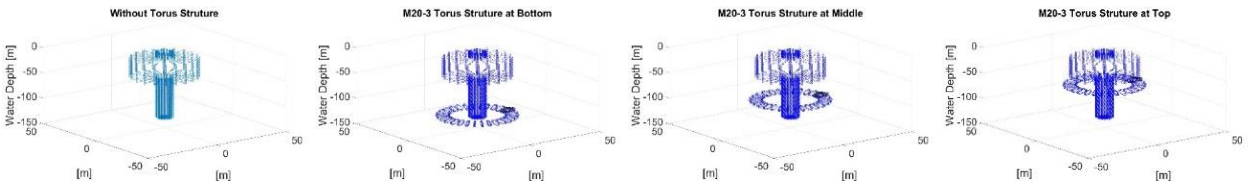

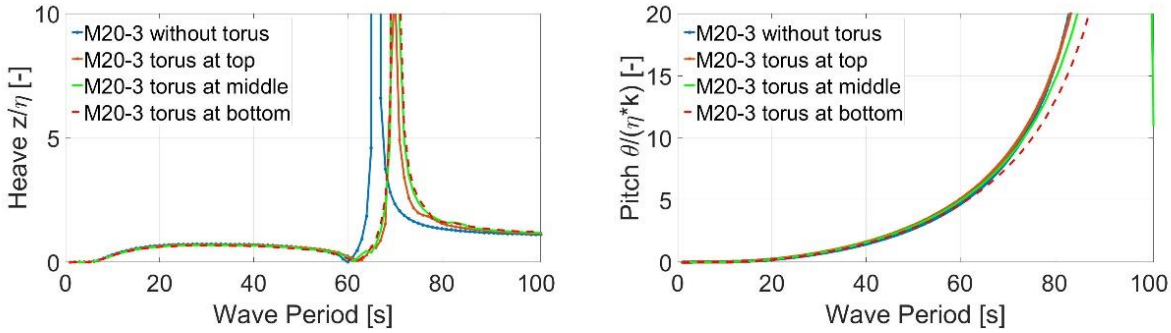

Fig. 4.48 Wet surface mesh and pitch RAO of M20-3

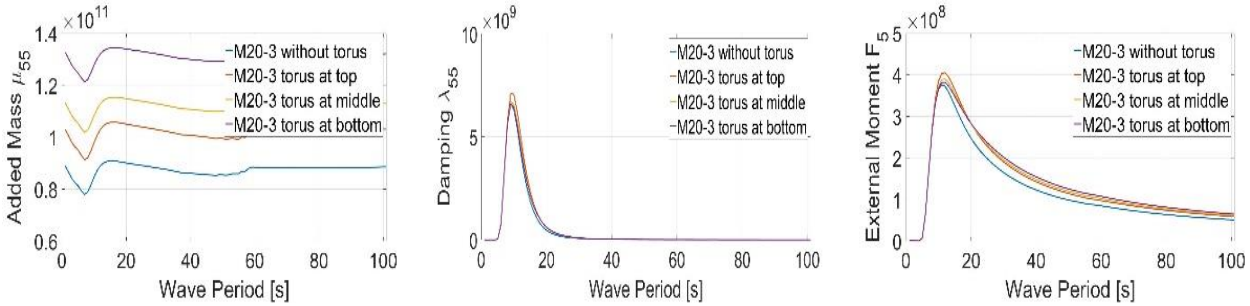

Fig. 4.49 Hydrodynamic parameters of M20-3

In terms of heave DOF, the torus structure of different heights will mainly cause a slight change in the added mass in the hydrodynamic parameters. The lower the vertical height of the torus structure, the greater the added mass, while the damping coefficient and external wave force hardly change. In the pitch DOF, the torus structure of different heights will also mainly cause the change of the added mass in the hydrodynamic parameters, but the magnitude of the change will be relatively large, and the trend of change is also that the torus structure goes down in the vertical height, the more the added mass is large, and the damping coefficient will hardly change, but the external wave force will change slightly. The conclusion is the same as the Cylinder-type FOWT.

2) M20-7

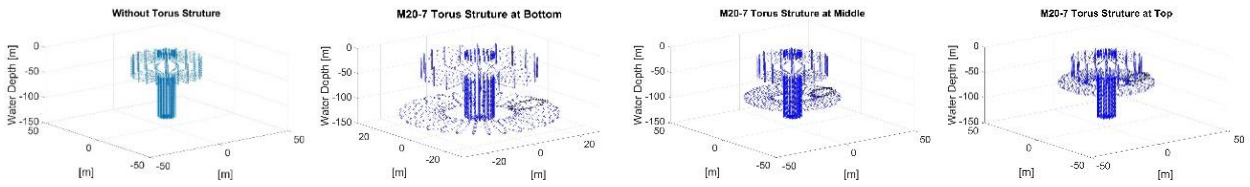

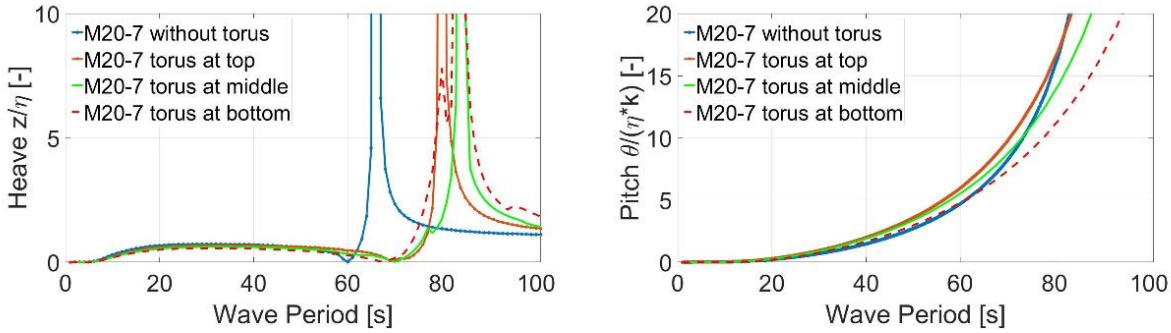

Fig. 4.50 Wet surface mesh and pitch RAO of M20-7

As can be seen from the RAO diagram of M20-3 and M20-7, when SPAR-type FOWT with a torus structure, a bigger natural period can be obtained than without torus structure, this is because the former has larger the mass coefficient and added mass coefficient, but the resilience coefficient does not change. According to common sense, the torus structure at top can withstand more intense wave, this is beneficial to the overall hydrodynamic response and is what we hope, but it will increase the overall center of gravity and buoyancy and reduce the moment of inertia around the horizontal axis, which will be harmful to the overall hydrodynamic response and is not what we want. However, the torus structure at top has not a better hydrodynamic response than the torus structure at middle, it looks like the advantage and disadvantages are almost neutralized and offset. When the torus structure at bottom has the best hydrodynamic, it looks like the advantages of lowering the overall center of gravity and buoyancy has a slightly greater impact than the disadvantage. The conclusion is the same as the Cylinder-type FOWT.

2. The light SPAR-type FOWT

Tab. 4.18 Parameters of model without torus, M10-2 and M10-3

Item	without Torus	M10-2 botto m	M10-2 middle	M10-2 top	M10-3 bottom	M10-3 middle	M10-3 top
Distance from Center of Tube to Torus [m]	0	10			10		
Radius of Tube of External Torus [m]	0	2.736			3.726		
Radius of Tube of Internal Torus [m]	**0**	**2**			**3**		
KB [m]	83.19	78.25	80.12	81.96	74.60	77.87	81.11
KG [m]	73.54	69.20	71.04	72.88	66.00	69.24	72.48
GM [m]	9.67	9.10			8.65		
Draft [m]	125.10						
Displacement [m^3]	22629	24109			25371		
Total Mass[t]	23195	24711			26005		
Moment of Inertia Jz [$t \cdot m^2 \times 10^4$]	85	96			101		

Moment of Inertia Jx [t·m²×10⁴]	18913	21177	20204	19504	23051	21261	19976
Moment of Inertia Jy [t·m²×10⁴]	18948	21212	20239	19538	23086	21296	20011
Proportion of Moment of Inertia of water Jz [%]	0.00	5.38			9.68		
Proportion of Moment of Inertia of water Jx [%]	0.00	5.45	3.26	1.55	11.28	6.94	3.35
Proportion of Moment of Inertia of water Jy [%]	0.00	5.44	3.26	1.54	11.26	6.93	3.34

1) M10-2

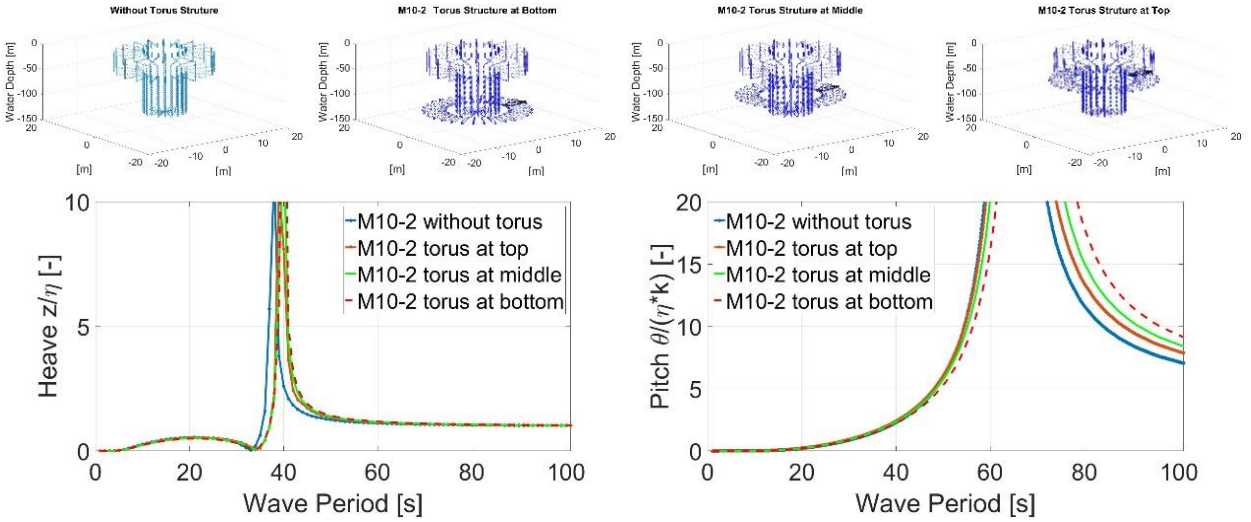

Fig. 4.51 Wet surface mesh and RAO of heave and pitch DOFs of M10-2 after weight reduction

2) M10-3

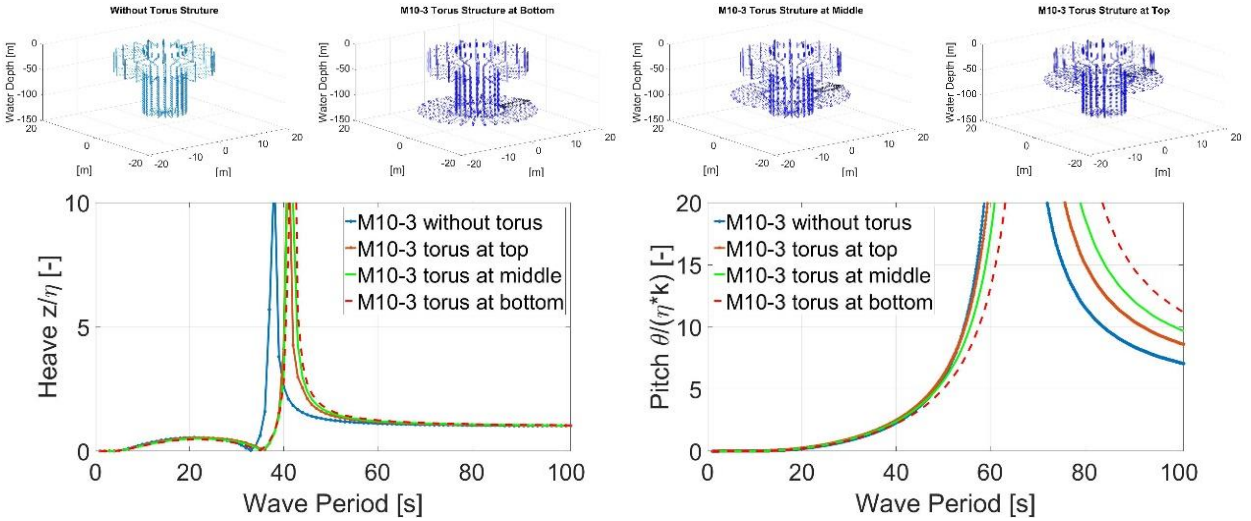

Fig. 4.52 Wet surface mesh and RAO of heave and pitch DOFs of M10-3 after weight reduction

As can be seen from the RAO diagram of M10-2 and M10-3 after weight reduction, the

natural period of its heave DOF decrease from more than 60s to 40s, and the natural period of pitch DOF has been greatly reduced compared with that before weight reduction. Other conclusions are similar, it is also when FOWT with a torus structure, a bigger natural period can be obtained than without torus structure, the torus structure at top has not a better hydrodynamic response than the torus structure at middle, and when the torus structure at bottom has the best hydrodynamic.

4.3.2.2 Change the Torus Structure

1. The heavy SPAR-type FOWT

Tab. 4.19 SPAR-type FOWT parameters with the radius change of ring tube of internal torus

Item	M20-1	M20-2	M20-3	M20-4	M20-5	M20-6
Distance from Center of Tube to Center of Torus [m]	20					
Radius of Tube of External Torus [m]	1.786	2.754	3.741	4.734	5.729	6.726
Radius of Tube of Internal Torus [m]	**1**	**2**	**3**	**4**	**5**	**6**
KB [m]	90.62	88.01	84.53	80.46	76.07	71.58
KG [m]	86.46	83.97	80.66	76.80	72.62	68.36
GM [m]	4.17	4.05	3.88	3.67	3.45	3.22
Draft [m]	129.25					
Displacement [m^3]	56191	57925	60455	63776	67887	72789
Total Mass [t]	57596	59374	61966	65371	69585	74609
Moment of Inertia Jz [$t \cdot m^2 \times 10^4$]	396	449	516	592	673	759
Moment of Inertia Jx [$t \cdot m^2 \times 10^4$]	54299	57132	61166	66333	72599	79862
Moment of Inertia Jy [$t \cdot m^2 \times 10^4$]	54371	57204	61238	66405	72671	79934
Proportion of Moment of Inertia of water Jz [%]	3.33	11.19	20.16	28.56	35.86	42.02
Proportion of Moment of Inertia of water Jx [%]	1.10	4.35	9.15	14.89	21.02	27.15
Proportion of Moment of Inertia of water Jy [%]	1.10	4.35	9.14	14.87	21.00	27.13

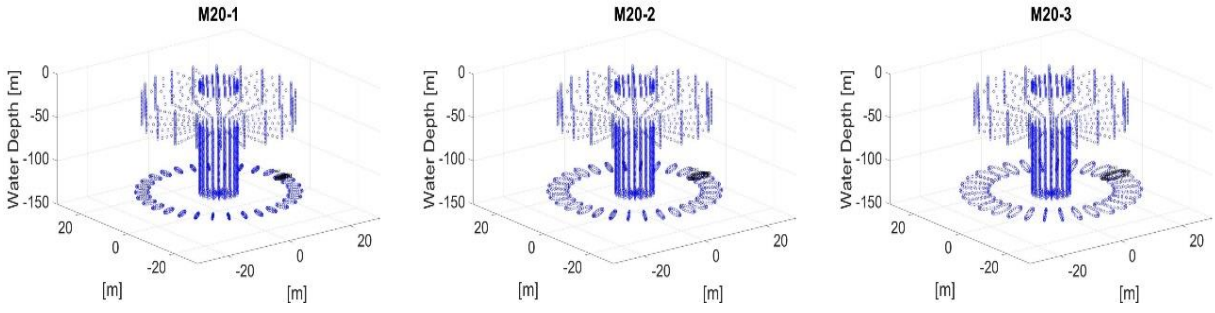

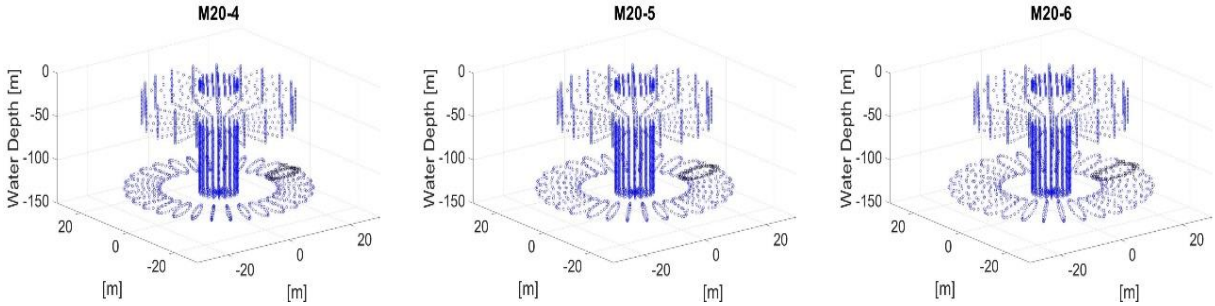

Fig. 4.53 SPAR-type FOWT wet surface mesh with the radius change of ring tube of internal torus

Tab. 4.20 SPAR-type FOWT parameters with distance from center of ring tube to center of torus change

Item	M10-3	M15-3	M20-3	M25-3	M30-3	M35-3
Distance from Center of Tube to Center of Torus [m]	**10**	**15**	**20**	**25**	**30**	**35**
Radius of Tube of External Torus [m]	3.726	3.736	3.741	3.744	3.746	3.747
Radius of Tube of Internal Torus [m]	3					
KB [m]	88.44	86.44	84.53	82.71	80.97	79.30
KG [m]	84.39	82.48	80.66	78.93	77.27	75.68
GM [m]	4.06	3.97	3.88	3.79	3.71	3.63
Draft [m]	129.25					
Displacement [m^3]	57662	59059	60455	61851	63248	64644
Total Mass [t]	59104	60535	61966	63398	64829	66260
Moment of Inertia Jz [$t \cdot m^2 \times 10^4$]	362	411	516	698	977	1375
Moment of Inertia Jx [$t \cdot m^2 \times 10^4$]	56605	58877	61166	63479	65823	68223
Moment of Inertia Jy [$t \cdot m^2 \times 10^4$]	56677	58949	61238	63551	65895	68295
Proportion of Moment of Inertia of water Jz [%]	2.70	9.66	20.16	30.94	39.77	46.18
Proportion of Moment of Inertia of water Jx [%]	4.91	7.10	9.15	11.09	12.94	14.70
Proportion of Moment of Inertia of water Jy [%]	4.90	7.09	9.14	11.08	12.92	14.69

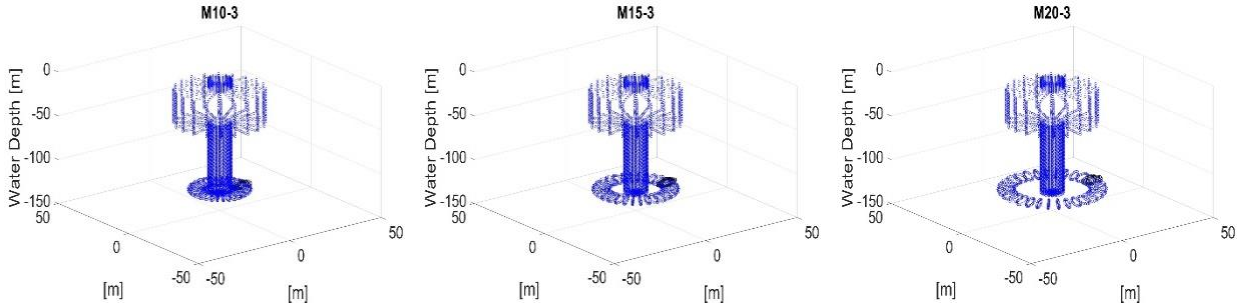

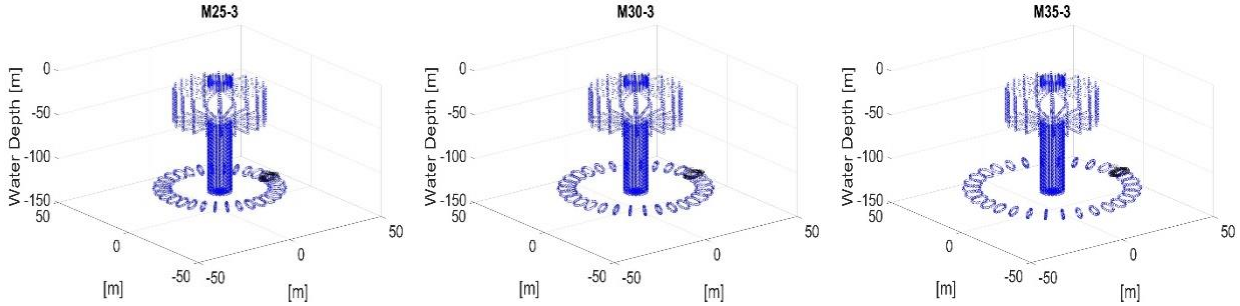

Fig. 4.54 SPAR-type FOWT wet surface mesh with distance from center of ring tube to center of torus change

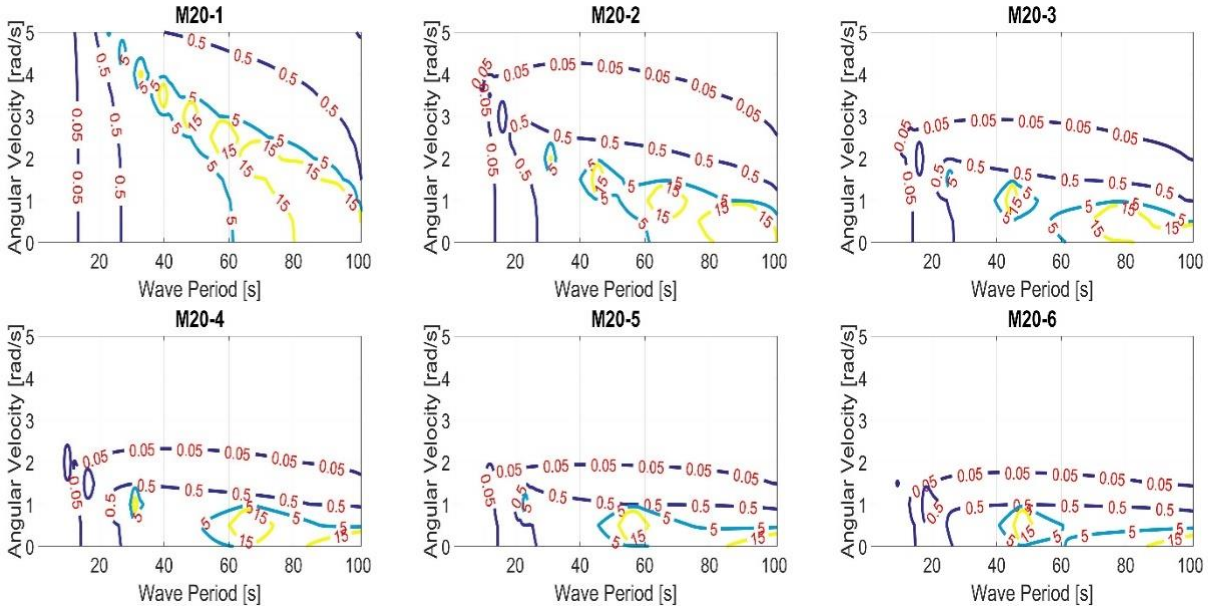

Fig. 4.55 Contour graph of SPAR-type FOWT pitch RAO with radius change of ring tube of internal torus

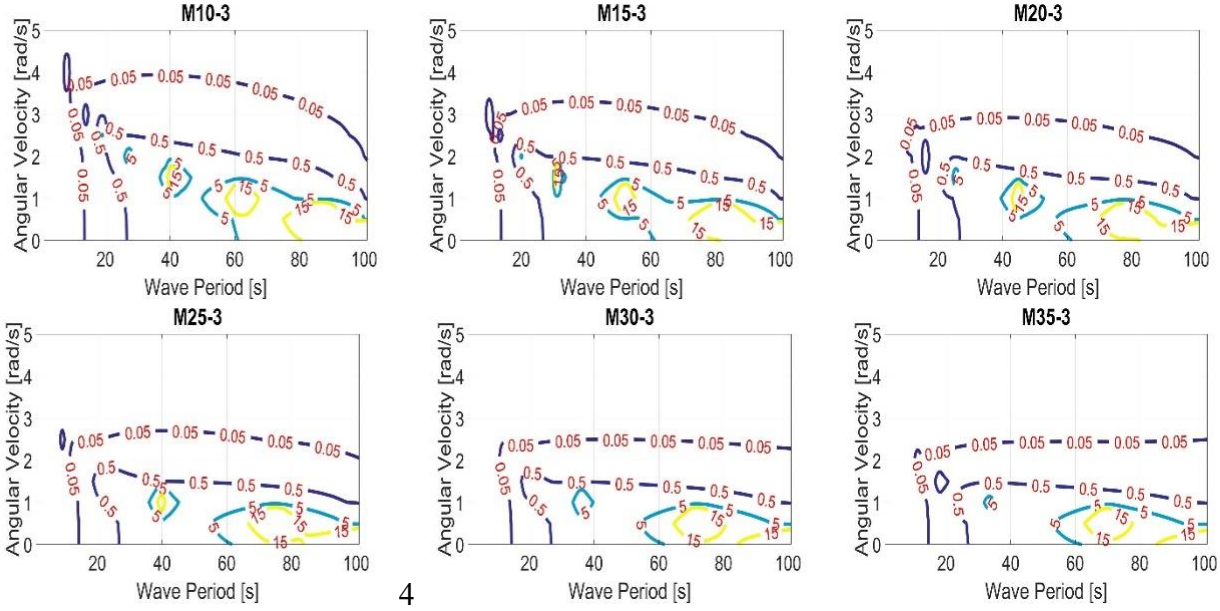

4

Fig. 4.56 Contour graph of SPAR-type FOWT pitch RAO with distance from center of ring tube to center of torus change

When the angular velocity is 0 rad/s, it is indicated that a large natural period over 100s can be obtained. Next, let us look at the effect of the angular velocity of annular flow. As already mentioned in the formulation in Chapter 3, the angular velocity of annular flow acts as a damping force in the motion within the range that can be linearized. It can be clearly confirmed that the dimensionless pitch response value of RAO is greatly attenuated near the natural period. In particular, focusing on the range where the dimensionless pitch response value is 5, the green line in the figure, when the angular velocity is less than 1 rad/s, the distance from center of ring tube to center of torus is over 20 m and the radius of ring tube of small torus is over 3 m, just as M20-3 in Fig. 4.55 and Fig. 4.56, the dimensionless pitch response value will be suppressed to 5 or less in a fairly wide periodic band. It can be considered that a large damping effect could be demonstrated even at a relatively small angular velocity. Consequently, the effects of annular flow portion appear relatively efficiently. In addition, the direction of contour lines tends to be basically parallel to the direction of wave period, and it can be revealed that the effect of attenuation will not have a particularly large increase when the angular velocity is greater than a certain value. When the angular velocity is 0 rad/s, the phase reversal phenomenon as with Fig. 4.57 will appear twice. However, when the angular velocity is not 0 rad/s, the phase reversal phenomenon will appear three times. Especially the phase is inverted across the natural period of the motion. Meanwhile, a small peak appears before the natural period in the RAO, and with the angular velocity increases, the earlier the small peak appear. However, it requires nearly twice the angular velocity compared with SPAR-type FOWT. From this aspect, the SPAR-type FOWT has better hydrodynamic response than the cylinder-type FOWT.

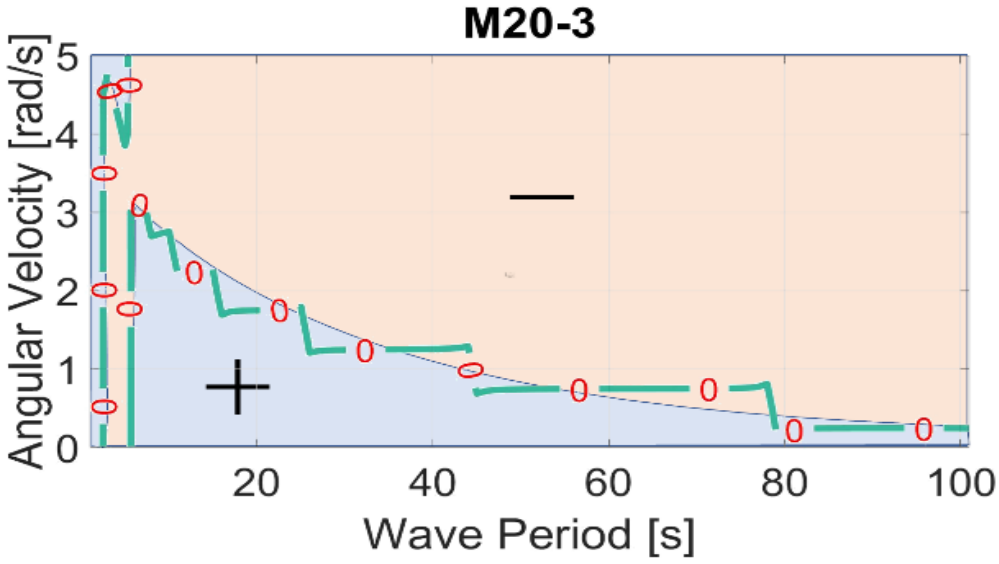

Fig. 4.57 Contour graph of M20-3 SPAR-type FOWT pitch phase

2. The light SPAR-type FOWT

Tab. 4.21 SPAR-type FOWT parameters with the radius change of ring tube of internal torus

Item	M10-1	M10-2	M10-3
Distance from Center of Tube to Center of Torus [m]	10		
Radius of Tube of External Torus [m]	1.76	2.736	3.726
Radius of Tube of Internal Torus [m]	**1**	**2**	**3**
KB [m]	81.04	78.25	74.60
KG [m]	71.65	69.20	66.00
GM [m]	9.41	9.10	8.62
Draft [m]	125.10		
Displacement [m^3]	23243	24109	25371
Total Mass [t]	23824	24711	26005
Moment of Inertia Jz [$t \cdot m^2 \times 10^4$]	91	96	101
Moment of Inertia Jx [$t \cdot m^2 \times 10^4$]	19862	21177	23051
Moment of Inertia Jy [$t \cdot m^2 \times 10^4$]	19897	21212	23086
Proportion of Moment of Inertia of water Jz [%]	1.65	5.38	9.68
Proportion of Moment of Inertia of water Jx [%]	1.40	5.45	11.28
Proportion of Moment of Inertia of water Jy [%]	1.40	5.44	11.26

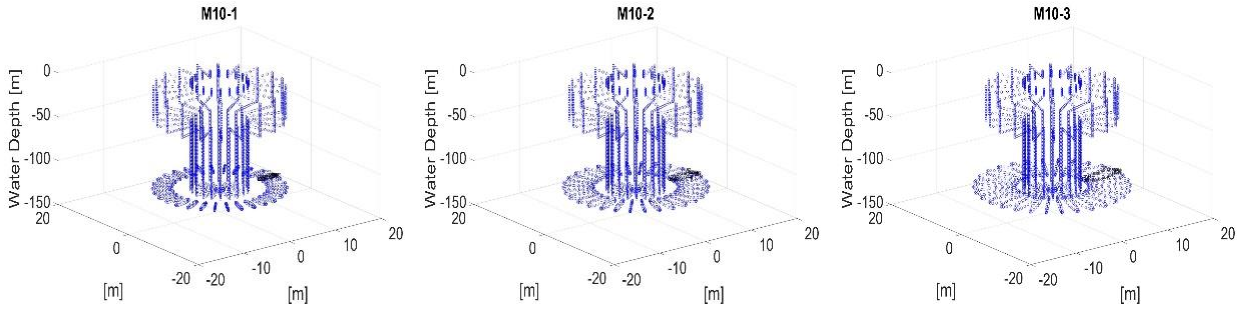

Fig. 4.58 SPAR-type FOWT wet surface mesh with the radius change of ring tube of internal torus

Tab. 4.22 SPAR-type FOWT parameters with distance from center of ring tube to center of torus change

Item	M8-2	M9-2	M11-2	M12-2
Distance from Center of Tube to Center of Torus [m]	**8**	**9**	**11**	**12**
Radius of Tube of External Torus [m]	2.72	2.732	2.739	2.742
Radius of Tube of Internal Torus [m]	2			
KB [m]	79.71	78.73	77.78	77.31

KG [m]	70.48	69.62	68.78	68.37
GM [m]	9.25	9.13	9.02	8.96
Draft [m]	125.10			
Displacement [m^3]	23651	23956	24261	24414
Total Mass [t]	24242	24554	24867	25024
Moment of Inertia Jz [$t \cdot m^2 \times 10^4$]	88	92	100	104
Moment of Inertia Jx [$t \cdot m^2 \times 10^4$]	20473	20942	21414	21648
Moment of Inertia Jy [$t \cdot m^2 \times 10^4$]	20508	20977	21448	21683
Proportion of Moment of Inertia of water Jz [%]	1.70	3.88	7.13	9.10
Proportion of Moment of Inertia of water Jx [%]	3.94	4.96	5.93	6.41
Proportion of Moment of Inertia of water Jy [%]	3.94	4.95	5.92	6.40

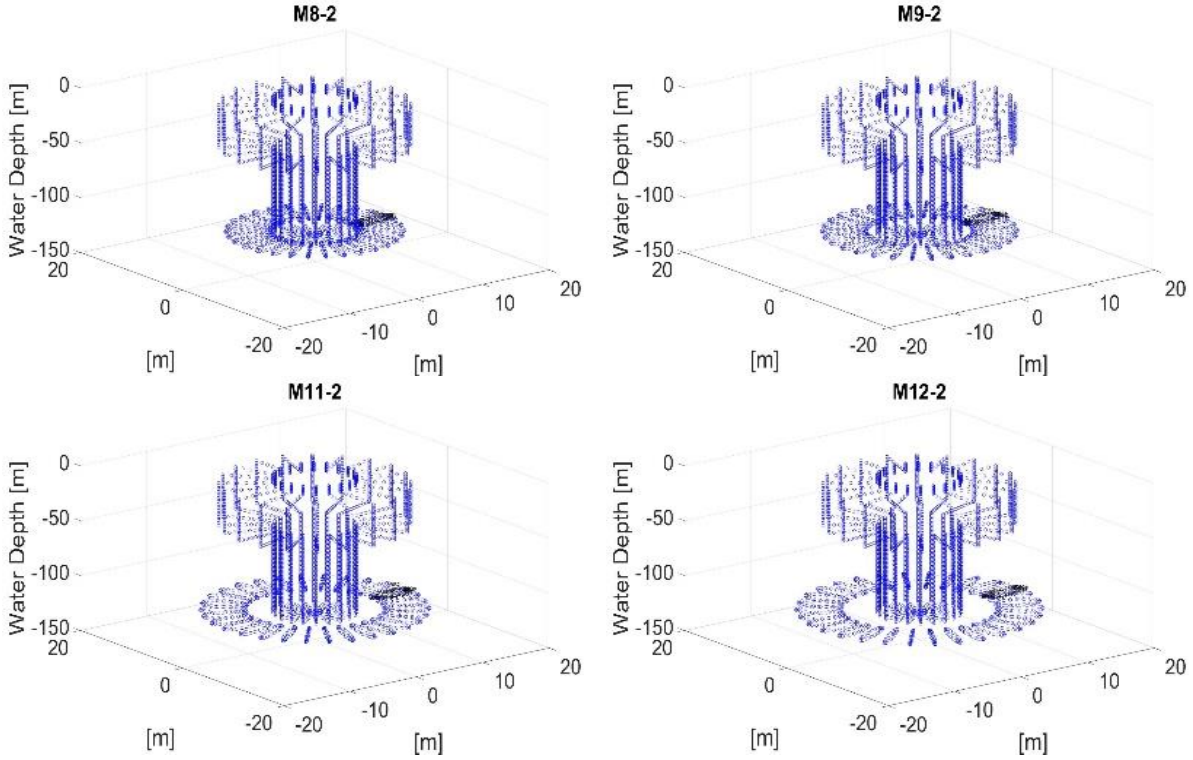

Fig. 4.59 SPAR-type FOWT wet surface mesh with distance from center of ring tube to center of torus change

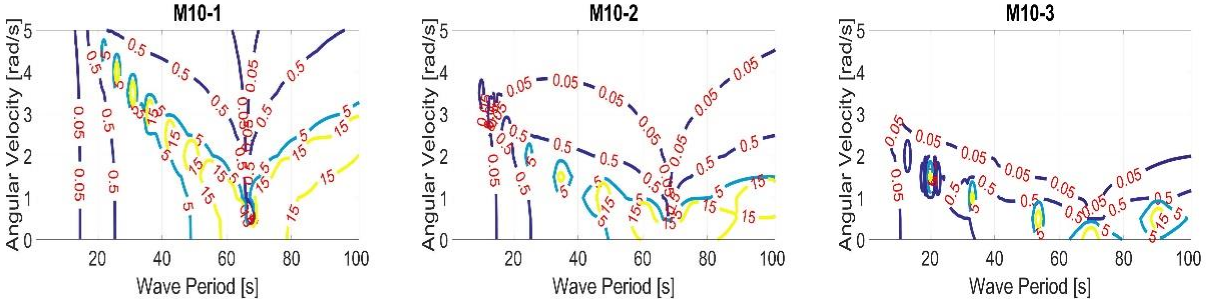

Fig. 4.60 Contour graph of SPAR-type FOWT pitch RAO with the radius change of ring tube of internal torus

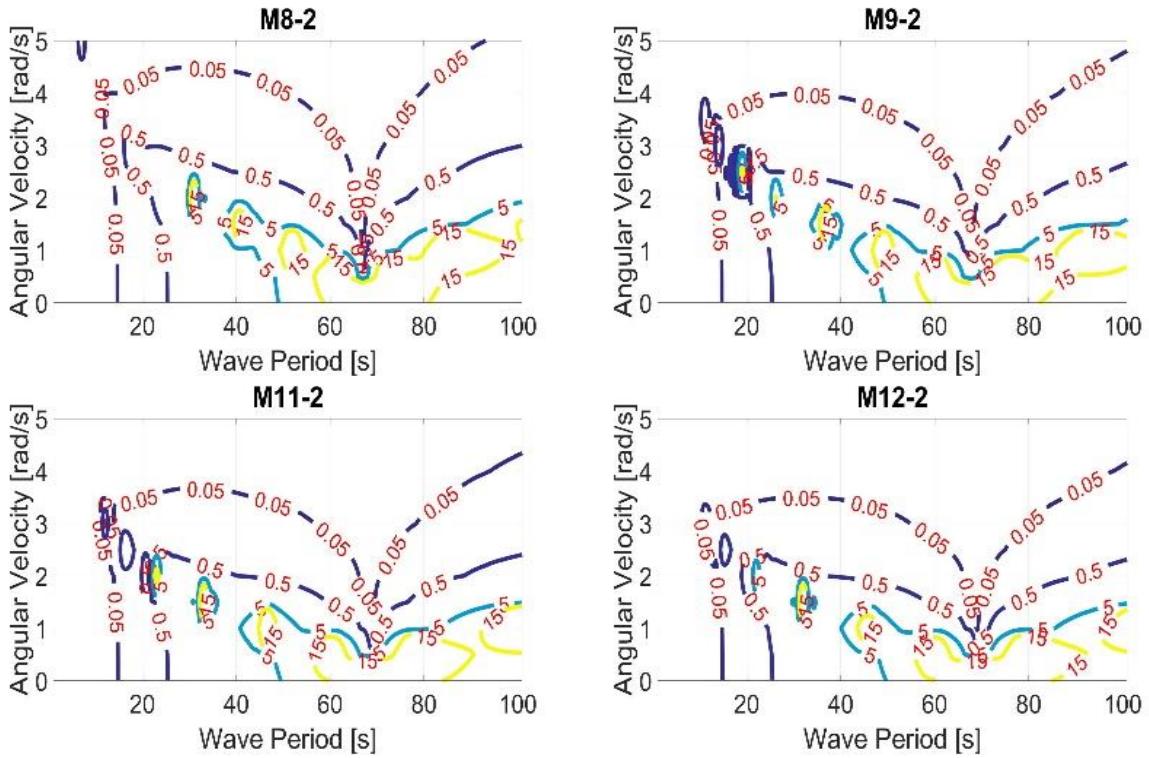

Fig. 4.61 Contour graph of SPAR-type FOWT pitch RAO with distance from center of ring tube to center of torus change

When the angular velocity is 0 rad/s, it is indicated that a large natural period over 60s can be obtained. Next, let us look at the effect of the angular velocity of annular flow. It can be clearly confirmed that the dimensionless pitch response value of RAO is greatly attenuated near the natural period. In particular, focusing on the range where the dimensionless pitch response value is 0.5, the blue line in the figure, when the angular velocity is less than 2 rad/s, the dimensionless pitch response value will be suppressed to 0.5 or less in a fairly wide periodic band. It can be considered that a large damping effect could be demonstrated even at a relatively small angular velocity. Consequently, the effects of annular flow portion appear relatively efficiently.

4.3.2.3 Change the Central Cylinder

Tab. 4.23 Characteristic parameters of SPAR-type FOWT with draft change

Item	M20-2
Distance from Center of Tube to Torus [m]	20
Radius of Tube of External Torus [m]	2.726
Radius of Tube of Internal Torus [m]	2
Cylinder Height [m]	50

Radius of cylinder [m]	15					
Ballast Height [m]	**13**	**14**	**15**	**16**	**17**	**18**
KB [m]	18.71	19.77	20.79	21.79	22.75	23.68
KG [m]	19.57	19.25	19.01	18.84	18.73	18.68
GM [m]	0.51	1.82	3.02	4.12	5.13	6.06
Draft [m]	36.97	39.30	41.62	43.94	46.27	48.59
Displacement [m^3]	29071	30713	32355	33997	35640	37282
Total Mass[t]	29798	31481	33164	34847	36531	38214
Moment of Inertia Jz [$t \cdot m^2 \times 10^4$]	434	453	472	491	510	529
Moment of Inertia Jx [$t \cdot m^2 \times 10^4$]	5868	6242	6680	7185	7760	8409
Moment of Inertia Jy [$t \cdot m^2 \times 10^4$]	5903	6277	6715	7220	7795	8444
Proportion of Moment of Inertia of water Jz [%]	11.59	11.10	10.66	10.25	9.87	9.51
Proportion of Moment of Inertia of water Jx [%]	3.51	3.70	3.86	3.99	4.08	4.15
Proportion of Moment of Inertia of water Jy [%]	3.49	3.68	3.84	3.97	4.07	4.13

Let the structure of torus have the same parameters, by changing the parameters of SPAR structure in the middle of total structure to see what varies will be produced to the output of RAO. Firstly, changing the parameter of draft and ensure that other parameters remain unchanged as much as possible. It is impossible to ensure that only one parameter changes without affecting the other one. Because the parameters of floating structure are related to each other. The height of ballast is changed linearly with an interval of 1 m, and the change in draught also increased almost linearly, meanwhile, the GM, displacement and moment of Inertia value are all increased by a large margin. An interesting phenomenon is the proportion of moment of inertia of water around z axis is always decreased, but the proportion of moment of inertia of water around x and y axis are all rise.

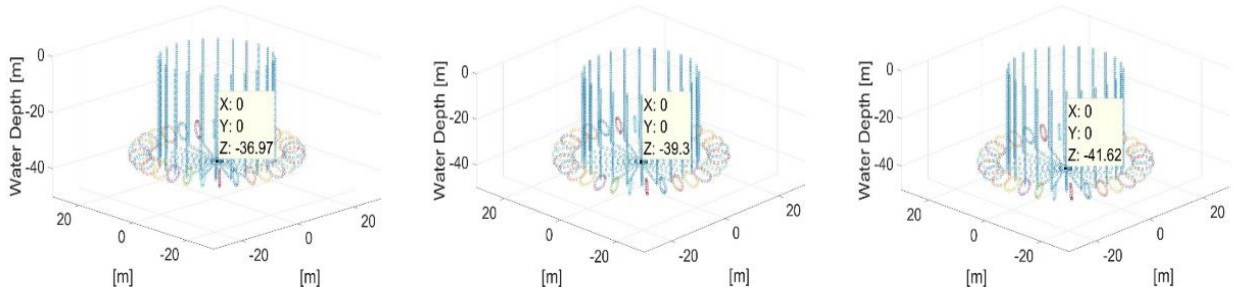

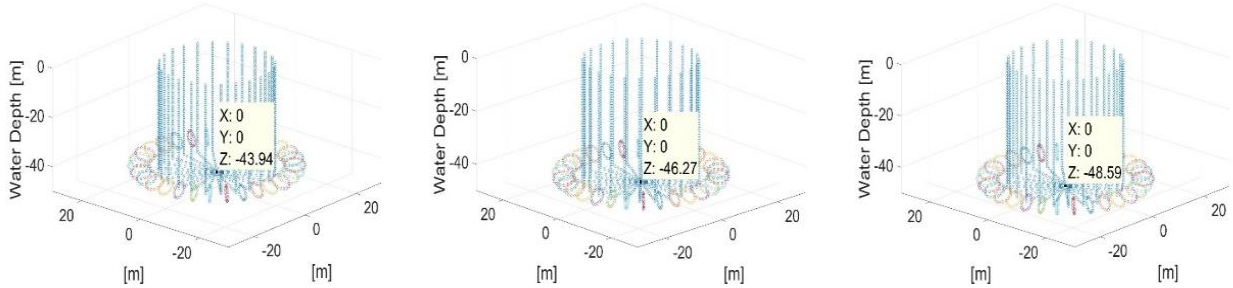

Fig. 4.62 SPAR-type FOWT wet surface mesh with draft change

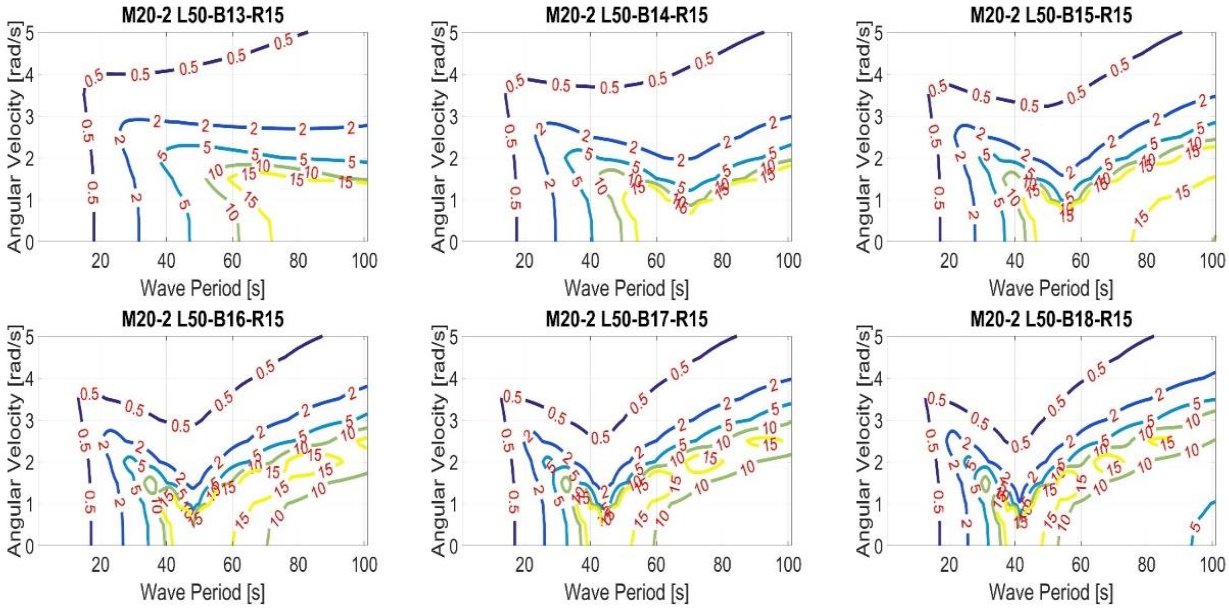

Fig. 4.63 Contour graph of SPAR-type FOWT pitch RAO with draught change and annular flow velocity change

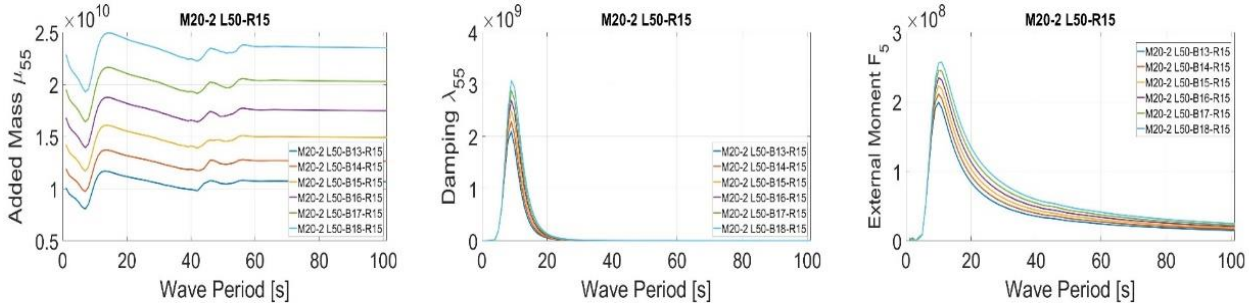

Fig. 4.64 Hydrodynamic parameters and dimensionless with draught change

These RAO curves located in the middle of Fig. 4.63 were obtained when the fluid in the inner torus structure is stationary. It can be seen that as the draught increases, the natural period of the floating body has been getting smaller, but the trend of getting smaller is slowing down. The natural period of free pitch is $T = \frac{2\pi}{\sqrt{\omega^2 - \alpha^2}}$, where, $2\alpha = \frac{B_{55}}{I_{22}+m_{55}}$, $\omega^2 = \frac{W \cdot GM}{I_{22}+m_{55}}$. It can be seen from Fig. 4.64 that although B_{55} and m_{55} will increase with the increase of draught, but damping coefficient B_{55} mainly increases slightly between the period of 10s and

20s, and the maximum increase is 1.5 times. The maximum increase of added coefficient mass m_{55} reached 2.5 times in the whole wave period. It can be seen from Tab. 4.23 that the maximum increase of W value is 1.3 times, while the maximum increase of GM value is 12 times. In summary, the GM value has the decisive impact, which directly leads to the reduction of the natural period. In addition, the law of change of the wave first-order external force had the similar to the damping coefficient.

In addition to change in natural period, it can be seen that the hydrodynamic response had obviously different at angular velocity = 0 rad/s with draught change from Fig. 4.63, and this is because at low wave period, the smaller draft FOWT has better hydrodynamic response and low wave period regular waves occupy the main position in the composition of irregular wave. It can also be seen that the hydrodynamics response had obviously different mainly at the high wave period with draught change. As the draught increases, the hydrodynamics response got better at the high wave period and narrower curve band can be seen clearly near the natural period. A higher natural period and a narrower curve band near the natural period are the RAO curve we want. However, the two kinds of phenomena seem to be contradictory and it is difficult to appear at the same time from the calculation results. However, when the angular velocity of annular flow is 2 rad/s and bigger, the very obvious attenuation effect can be got around the natural period.

Tab. 4.24 Characteristic parameters of SPAR-type FOWT with radius of central cylinder change

Item	M20-2					
Distance from Center of Tube to Torus [m]	20					
Radius of Tube of External Torus [m]	2.726					
Radius of Tube of Internal Torus [m]	2					
Cylinder Height [m]	50					
Ballast Height [m]	18					
Radius of Cylinder [m]	12	13	14	15	16	17
KB [m]	23.08	23.33	23.52	23.68	23.80	23.90
KG [m]	23.21	21.39	19.91	18.68	17.66	16.80
GM [m]	0.52	2.72	4.54	6.06	7.36	8.49
Draft [m]	48.14	48.34	48.48	48.59	48.67	48.73
Waterline Area [m^2]	452.39	530.93	615.75	706.86	804.25	907.92
Displacement [m^3]	24715	28601	32790	37282	42077	47174
Total Mass[t]	25333	29316	33610	38214	43128	48354

Moment of Inertia Jz [t·m²×10⁴]	293	355	432	529	647	789
Moment of Inertia Jx [t·m²×10⁴]	6259	6917	7634	8409	9244	10140
Moment of Inertia Jy [t·m²×10⁴]	6294	6952	7669	8444	9279	10175
Proportion of Moment of Inertia of water Jz [%]	17.14	14.18	11.63	9.51	7.78	6.37
Proportion of Moment of Inertia of water Jx [%]	5.47	4.99	4.55	4.15	3.79	3.46
Proportion of Moment of Inertia of water Jy [%]	5.44	4.97	4.53	4.13	3.77	3.45

The SPAR FOWT with such a large radius and small draft for the supporting part of the floating body has not been manufactured in actual production. The purpose of using this model in this calculation is mainly to take into account that its large radius will give the interior a very large space. As we all know, the main reason why FOWT cannot use TMD systems to increase damping and shock absorption like skyscrapers is that the interior of FOWT does not have sufficient space in the horizontal direction. In addition, another feature of this model is that it has a very thick outer wall. It is said that this model is an idealized model. Many production components installed for power generation inside the model are not considered. Thicker walls are used to compensate for these components. But it is still relatively thick. Another point, the ballast material used in this model is stone.

Secondly, changing the parameter of radius of cylinder and ensure that other parameters remain unchanged as much as possible. The radius of cylinder is changed linearly as the red font in the Tab. 4.24, and as the radius of cylinder increases with an interval of 1 m, the change in draught gradually decreases, the GM, displacement and moment of Inertia value are all increased by a large margin. The proportion of moment of inertia of water are all decreased, in particular, the moment of inertia around vertical z axis is significantly decreased.

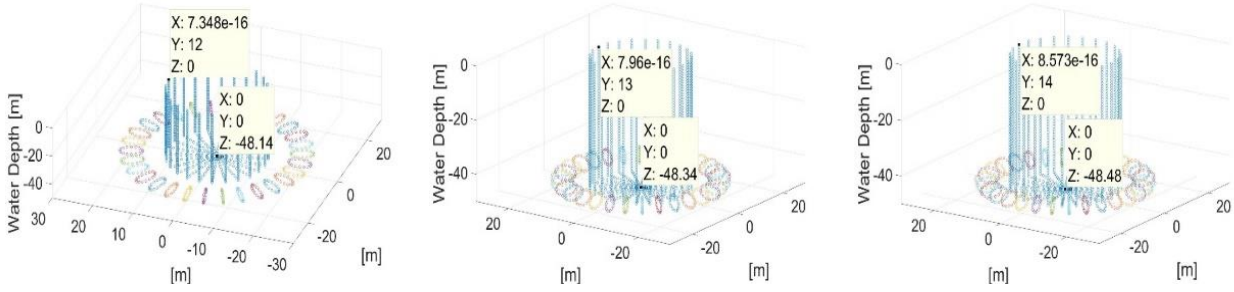

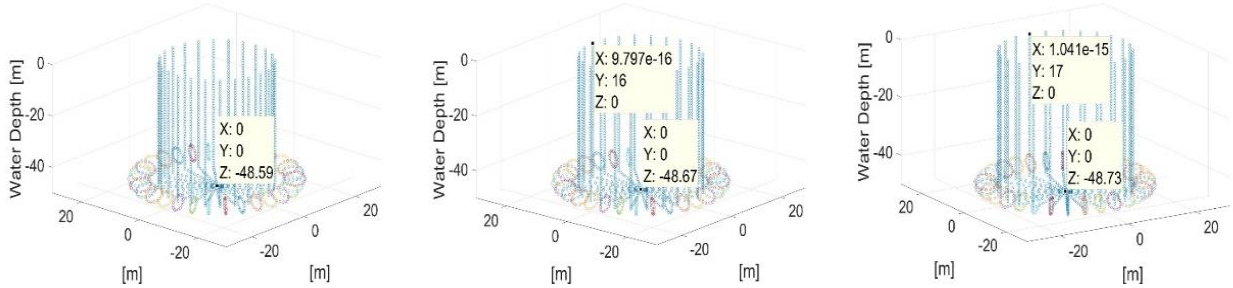

Fig. 4.65 SPAR-type FOWT wet surface mesh with radius of central cylinder change

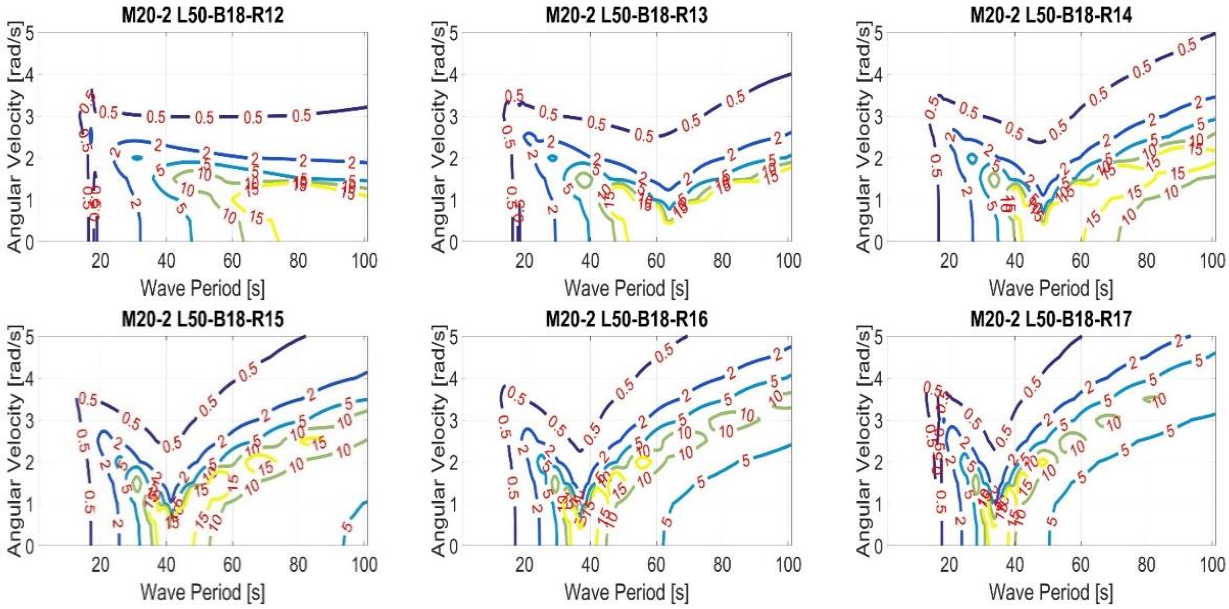

Fig. 4.66 Contour graph of SPAR-type FOWT pitch RAO with radius change and annular flow velocity change

It can be seen that the hydrodynamics had accordingly undergone a very big change from Fig. 4.66 very clear. Although the radius of cylinder increases with an interval of 1 m, the natural period of pitch degree motion changes greatly. The natural period of pitch degree reduced with the increase in the radius of cylinder. At the low wave period, we cannot sure to get a better hydrodynamic when the radius of cylinder is small, and the natural period of pitch degree motion decreases with the increase of the radius. Although the decreasing trend become slower, but the magnitude of the decrease is very large. A natural period around 30s is very bad and needs to be avoided as much as possible. It can be seen that the hydrodynamics had obviously different mainly when the dimensionless RAO value is big, and the smaller the radius of the cylinder, the larger the dimensionless RAO value will start to change from Fig. 4.66. When the angular velocity of annular flow is 2 rad/s and bigger, the very obvious attenuation effect can be got.

4.3.3 The rotational kinetic energy

Next, its engineering possibility from the viewpoint of energy consumption is discussed. The M40-3 case is selected, for this case, the maximum electric power generated from wind energy is about 2×10^7W. The rotational kinetic energy will be

$$E = \frac{1}{2} I\omega^2 \tag{4.20}$$

where, I is the rotational inertia, ω is the angular velocity of annular flow water.

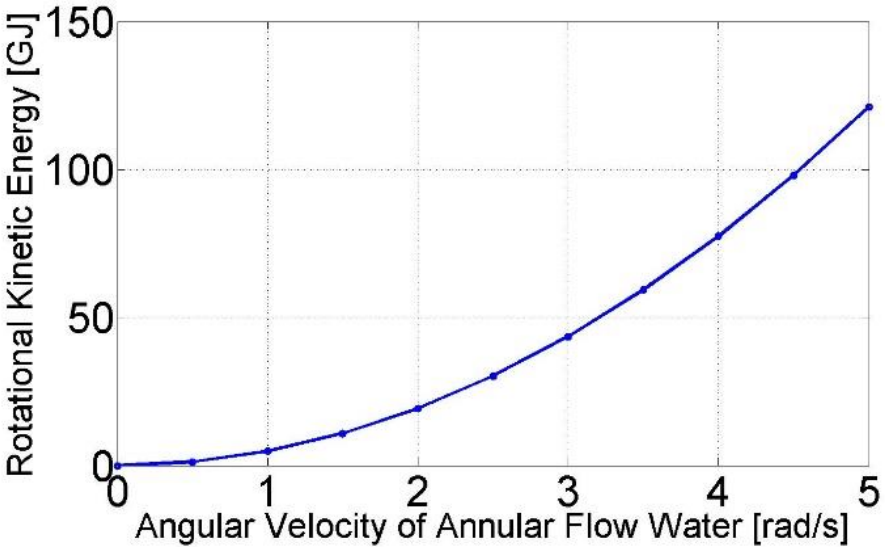

Fig. 4.67 Rotational kinetic energy

When the angular velocity of annular flow water increases from 0 to 3 rad/s that can get a significant shaking reduction effect, the energy that makes the flow water in the torus structure requires 43.6 GJ, and the time taken to accelerate the flow water in the torus structure with the electricity generated by FOWT is only 36 minutes. Of course, the calculation of the energy consumption also includes the energy needed to overcome the friction force to maintain the rotating motion. However, only from the calculation results of the rotational kinetic energy, it does not take a long time to increase the rotational angular velocity to the required rotational angular velocity, and in future actual operations, the flow water in the torus structure does not necessarily have to accelerate from 0. Therefore, we can preliminarily conclude that the engineering possibility of this idea is very high.

From the viewpoint of technical possibility, although there are frictionless phenomena like the rotation motion of the suspended moon around the earth is frictionless in the universe; superfluidity that helium can exhibit zero viscosity at ultra-low temperatures [57]; biological superfluidity [58], it cannot be practically applied in engineering through technical means. The

Maglev train is a more pragmatic solution, which an experimental Japanese maglev reached over 600 km/h in 2015. Converted to the M40-3 case in this paper, it is 4.2 rad/s and greater than the required angular velocity 3 rad/s.

4.3.4 The Motion on Yaw DOF

Obviously, only a single torus structure with annular flow will cause the motion of FOWT in yaw DOF to become larger, considering the current method of helicopter counteracting the motion of yaw DOF, two torus structures with annular flow of opposite rotation direction will be reduce the motion of the yaw DOF, but the rotational axis retention effect of its single torus structure with annular flow will cancel each other out and disappear. The second method of mounting a vertical rotation mechanism on the tail is currently considered feasible. Its feasibility is still under study.

Fig. 4.68 Two kinds of helicopter wing mounting methods

Chapter 5:Conclusion

In this paper, the same gyroscopic effect and the same rotational axis retention effect was not obtained by the rotational motion of a rigid body, rather than by means of an annular flow in a ring tube of torus. For the novel idea of SPAR-type FOWT using torus structure with the annular flow water, this paper mainly focuses on and performs hydrodynamic calculations, which lead to the determination of the geometry of the torus structure and the required rotational angular velocity of the rotating part inside the torus structure, and the feasibility from the viewpoint of energy consumption is briefly analyzed in terms of realizability, which is very high.

1. The novel design of using the annular flow water in the torus structure as the spinning top is confirmed through experiments, and its influence on the hydrodynamic response is mainly acting on the damp term as a damping force.
2. From the calculation results in the regular wave, it is revealed that when the volume of annular flow water is rational, a large damping effect can be confirmed overwhelmingly even at a relatively small angular velocity of annular flow water.
3. From the calculation results in the irregular wave, it is found that when the proportion of the moment of inertia Jy of annular flow water is about 5%, and the angular velocity of annular flow water is about 3rad/s, a significant vacillating suppression effect can be obtained.
4. When a better shaking suppression effect is obtained, the energy consumed by the annular flow water is not a large amount for the power generation of FOWT.

In the future, a complete dynamics analysis considering the aerodynamics of the part above the water-plane and finding a way to minimize the friction in the torus structure is a direction worthy of research efforts. It is also necessary to examine the engineering feasibility of this area in the future.

References

[1] BP, statistical review of world energy 2021. 2021.07

[2] 石田 茂資. 再生可能エネルギー学術ワークショップ×SDGs,佐賀大学海洋エネルギーセンター, 2021/10/04.

[3] https://gwec.net/global-wind-report-2021/

[4] https://www.ren21.net/

[5] https://gwec.net/global-offshore-wind-report-2020/

[6] Floating Offshore Wind Turbine Technology Guidebook, NEDO, 2019.03

[7] 鈴木 英之. 横浜国立大学浮体式洋上風力発電に関する勉強会,2021.6.17.

[8] KANRIN 第 88 号(2020.01),第 96 号(2021.05),日本船舶海洋工学会誌.

[9] https://en.wikipedia.org/wiki/Wind_power

[10] 村井 基彦. 横浜国立大学コンクリート製浮体式洋上風力発電システム（CFW）に関する勉強会,2020.9.3.

[11] https://www.hexicon.eu/mfn_news/hexicon-to-develop-twinway-project-for-floating-wind-in-norway/

[12] https://www.rystadenergy.com/

[13] https://ec.europa.eu/info/index_en

[14] http://jwpa.jp/index_e.html

[15] https://en.wikipedia.org/wiki/INS_Vikrant_(2013)

[16] 任俊生. 船舶運動與控制. 大連海事大學航海技術研究所. 2012

[17] Shengwen Xu, Motohiko Murai, Xuefeng Wang, KensakuTakahashi. A novel conceptual design of a dynamically positioned floating wind turbine. Ocean Engineering, Volume 221, 1 February 2021

[18] 井上 義行. 係留浮体の運動と係留力の推定法に関する研究. 昭和 53 年 12 月

[19] M. Murai, K. Ishikawa, R. Nishimura. A Study on an Experiment of Behavior of a SPAR Type Offshore Wind Turbine Con-sidering Rotation of Wind Turbine Blades, Oceans2010, 2010.05.

[20] Faisal Mahmuddin. Rotor Blade Performance Analysis with Blade Element Momentum Theory. Energy Procedia, Volume 105, May 2017.

[21] 劉應中, 繆國平. 船舶在波浪上的运动理论. 上海交通大學出版社. 1986.

[22] 朱仁傳, 繆国平. 船舶在波浪上的運動理論. 上海交通大學出版社. 2019.

[23] 王洪偉. 我所理解的流體力學. 國防工業出版社, 2014.

[24] Haskind, M. The hydrodynamic theory of ship oscillations in rolling and pitching. Prikl. Mat. Mekh. 1946, 10, 33–66.

[25] Haskind, M. The oscillation of a ship in still water. Izv. Akad. Nauk SSSR Otd. Tekh. Nauk 1946, 1, 23–34.

[26] F. Ursell. On The Heaving Motion of a Circular Cylinder on the Surface of a Fluid. The

University, Manchester, 1949.

[27] M. D. Haskind, On wave motions of a heavy fluid, Prikl. Mat. Mekh. 18 (1954) 15–26.

[28] T. H. Havelock. The Damping of the Heaving and Pitching Motion of a Ship. 1942.

[29] Fritz John. On the motion of floating bodies. I. 1949.

[30] Fritz John. On the motion of floating bodies. II. Simple harmonic motions. 1950.

[31] John L. Hess; A. M. O. Smith. Calculation of nonlifting potential flow about arbitrary three-dimensional bodies. Journal of Ship Research, 8 (04): 22–44.1964-09-01.

[32] A. B. Finkelstein. The initial value problem for transient water waves. Communications of Pure and Applied Mathematics, 10:511-522. 1957.

[33] Cummins, W.E. The impulse response function and ship motions. Schiffstechnik, 47, 101-109. 1962.

[34] Gerard van Oortmerssen. Thesis of the motions of a moored ship in waves, 1976

[35] Korvin-Kroukovsky, B.V. Investigation of ship motions in regular waves. 1955.

[36] Korvin-Kroukovsky, B.V; Winnifred R Jacobs. Pitching and heaving motions of a ship in regular waves. 1957.

[37] 田才 福造, 高木 又男, 規則波中の応答理論及び計算法 [J]. 耐波性に関するシンポジウム（第一回), 日本造船学会, 1969.

[38] Ogilvie, T. Francis; Tuck, Ernest O. A rational strip theory of ship motions: Part I. University of Michigan, 1969-03-01.

[39] Ogilvie, T. Francis; Tuck, Ernest O. A rational strip theory of ship motions: Part II. University of Michigan, 1971-01-01.

[40] Salvesen, Nils; Tuck, E O; Faltinsen, O. Ship Motions and Sea Loads [J]. 1970.

[41] Frank, Werner. Oscillation of cylinders in or below the free surface of deep fluids. 1967.10.

[42] Newman John Nicholas. The theory of ship motions. Advances in Applied Mechanics, Volume 18, 1978, pp. 221-283.

[43] St Dinis, W. Pierson. On the motions of ships in confused seas. 1953.

[44] Yakov Isidorovich Perelman. Physics for Entertainment: Volume 2.

[45] https://en.wikipedia.org/wiki/Viscosity

[46] George • Green. An Essay on the Application of Mathematical Analysis to the Theories of Electricity and Magnetism, 1828.

[47] C. Neumann. Ueber die Integration der partiellen Differentialgleichung: $\frac{\partial^2\Phi}{\partial^2 x}+\frac{\partial^2\Phi}{\partial^2 y}=0$. Article in Journal für die reine und angewandte Mathematik (Crelles Journal), published July 1861, pp. 335-366.

[48] 高木 又男, 新井 信一. 船舶•海洋構造物の耐波理論. 成山堂書店. 1996.

[49] 神部 勉, 偏微分方程式, Application Mathematics 3. 講談社, 1987.

[50] N. M. Newmark, “A Method of Computation for Structural Dynamics,” ASCE Journal of

the Engineering Mechanics Division, Vol. 85, 1959, pp. 67-94.

[51] http://ocedu.zju.edu.cn/bkspy//attachments/2018-12/01-1545977908-484635.pdf

[52] 元良誠三.浮体と海洋構造物の運動学.成山堂書店.1997

[53] Claudio Rodríguez. Lecture. Federal University of Rio de Janeiro(UFRJ), brazil

[54] Ying-Xin Zhou, Jia-Sheng Zu, and Jing Liu. Fluidic Endogenous Magnetism and Magnetic Monopole Clues from Liquid Metal Droplet Machine.

[55] M. Murai and A. Nagamine. Comparisons of Hydrodynamic Behavior of Vertical Axis and Horizontal Axis FOWT, Proc. of More, 2013.

[56] https://www.jodc.go.jp/jodcweb/

[57] https://en.wikipedia.org/wiki/Superfluidity

[58] Aurore Loisy, Jens Eggers, and Tanniemola B. Liverpool1. Active Suspensions have Nonmonotonic Flow Curves and Mul-tiple Mechanical Equilibria. Physical Review Letters 121, 018001 (2018). DOI: 10.1103/PhysRevLett.121.018001.